MAGIC-TDAS 05-11
051027/MGarcz

Analysis of the GRB050713a data using the huge Markarian 501 flare

Authors: Markus Garczarczyk MPI Munich
Markus Gaug IFAE Barcelona

November, 2005

Abstract

We analyzed the 2223 seconds of GRB050713a data taken on the 13$^{\text{th}}$ of July, 2005 and the Markarian 501 flare data from July, 1$^{\text{st}}$ using two absolute image cleaning levels and some of the newly developed image cleaning methods employing the times information. We obtain a 4σ signal from one hour of Mrk501 flare data in an energy bin of 65 GeV average energy and 5σ at a mean energy of 78 GeV. Applying a similar analysis to the GRB050713a data, we do not see any signal and derive two differential flux limits on the first 90 s of data taken during the prompt emission phase of $d\Phi/dE < 1.3 \cdot 10^{-17}\,\mathrm{ph\,cm^{-2}\,keV^{-1}\,s^{-1}}$ or 3.6 Crab units at $E = 150\,\mathrm{GeV}$ and $d\Phi/dE < 2.3 \cdot 10^{-18}\,\mathrm{ph\,cm^{-2}\,keV^{-1}\,s^{-1}}$ or 3.2 Crab units at $E = 280\,\mathrm{GeV}$ (99% CL). These limits include systematic effects due to the unknown spectral index of the incident photons, uncertainties about the point-spread function of the telescope during the observation of the GRB, inefficiencies of some trigger cells and an overall absolute calibration error of 10%. A second, semi-independent $DISP$-analysis yields very comparable limits, although at energies generally higher energies by about 5 GeV. The first limit is obtained at an energy about 20% lower than the lowest energy bin given by N. Galante and A. Stamerra, while the other limit results a factor four or $2.5\,\sigma$ of the given error of their analysis lower than their results. Other differential and integral flux limits are derived for longer time periods as well as possible transient emission during any 100 s time interval.

Contents

1 Preface **3**

2 Executive Summary **4**
2.1 Introduction . . . 4
2.2 Calibration and Image Cleaning . . . 5
2.3 Data Reduction . . . 5
2.4 Results . . . 6

3 Introduction **11**

4 The Data Samples **12**

5 Calibration **17**
5.1 Modifications and Bugs . . . 17
5.2 Extracting the conversion factors from the interlaced calibration events of the previous source . . . 18
5.3 Excluded Pixels . . . 18

6 Image Cleaning **20**

7 Cuts **22**
7.1 SIZE . . . 22
7.2 DIST . . . 25
7.3 CONC . . . 28
7.4 Further Cuts . . . 32
7.5 Cut Efficiencies . . . 32
7.6 SIZE after pre-cuts . . . 35
7.7 Center of Gravity after pre-cuts . . . 38

8 Random Forest Analysis **40**
8.1 Mrk501 data . . . 40
8.2 GRB050713 data . . . 45
8.3 Tests of the Parameters used for the RF training . . . 52

9 Alpha Analysis **59**
9.1 Optimizing Cut on HADRONESS . . . 62
9.2 Results Mrk501 Data . . . 64
9.3 Results GRB050713a Data . . . 69
9.3.1 Prompt emission phase . . . 69
9.3.2 First 1000 Seconds . . . 74
9.3.3 Entire Data Sample . . . 77
9.4 Calculation of Effective Areas . . . 80
9.5 Calculation of the Upper Limits . . . 82
9.6 Search in time slices of 100 seconds . . . 90
9.7 Effect of systematic uncertainties on the limits . . . 96

10 Disp Analysis **98**
10.1 Results Mrk501 Data . . . 101
10.2 Results GRB050713a Data . . . 106
10.2.1 Prompt emission phase . . . 106
10.3 Search in time slices of 100 seconds . . . 112

11 Conclusions **116**

1 Preface

We present an analysis of the GRB050713a data, taken on the 13^{th} of July, 2005, independent from a previous one presented by Nicola Galante and Antonio Stamerra [1]. This analysis is entirely focussed on low-energy events and introduces and compares a series of non-standard analysis elements:

- A signal larger extraction window to get rid of the camera inhomogeneity.
- Calibration of the GRB data, using the interleaved calibration events from the last run taken with the previous source.
- A couple of bug fixes found in and introduced to the Mars_V0-10 branch.
- New image cleaning algorithms employing the time information extracted from the FADCs.
- A new image reconstruction method weighting the second moments by the individual $SIZE$ values elevated by an exponent different from one.
- Training of the $RANDOM\ FOREST$ exclusively on sizes smaller than 400 p.e.
- An analysis using signals as low as 90 p.e.
- A new method to choose the best cut on $HADRONNESS$ by maximizing the Li&Ma signal significance without the use of the (biasing) ON-data.
- A different way to derive an differential upper limit in a relatively fine energy bin.

These methods are not yet standard, for this reason we will prove their principal functioning on the Mrk501 flare data, taken in the observation period, on the 1^{st} of July, 2005.

We will show that our analysis is able to reduce the threshold and increase the sensitivity of the MAGIC telescope well below 100 GeV for low zenith angle observations like Mrk501, and well below 200 GeV for the GRB050713a, observed at a zenith angle of 49°.

The resulting flux limit on GRB050713a can thus be placed at an energy about 20% lower than the lowest limit obtained by [1], essential for a source at very high redshift where the absorption by the Meta-galactic Radiation Field is dominant.

Because of the avant-garde character of this analysis, we decided to present two important additions:

1. We tested the whole analysis on the Mrk501 flare data, taken just one and a half weeks before with the same telescope conditions and show that if there is a sizable signal at low energies, our analysis is able to extract it with high significance.
2. We present in the following a rather detailed documentation of the methods needed to convince ourselves and others about the reliability and robustness of the results. We include many plots which we would have liked very much to see from other analyses in MAGIC and which we think are essential to judge the outcome of a spectrum or an upper limit.

For these two reasons, the scope of this document is much larger than e.g. the first analysis presented on the GRB050713a data [1]. For the busy reader, we have also included an executive summary of four pages which summarizes the most important steps and results.

This analysis is meant to be our future "standard" analysis for future GRB data and can be run soon on a stand-alone mode. This includes all plots shown in this document.

2 Executive Summary

2.1 Introduction

GRB050713a was detected on July, 13^{th}, 2005, at 04:29:02.39 UTC by the BAT instrument on the SWIFT satellite. The alert was distributed over the GCN within 13 seconds (SWIFT trigger 145675). It was announced to the GCN 122 seconds after the detection with uncertainty of 3 arcmin radius [2]. The XRT and the UVOT detectors, also located on SWIFT, found a fading source at RA: 21h 22m 09.6s, Dec: +77d 04m 30.3s. The MAGIC telescope started to observe the position 40 sec. after the onset of the burst ($T0$). While the brightest part of the keV emission occurred within $T0 + 20s$, three smaller peaks followed at $T0 + 50$s, $T0 + 65$s and $T0 + 105$s, thus after the start of the observation of MAGIC (see figure 1). The burst position was observed by MAGIC for 2223 seconds in a zenith angle range between 49° to 50°, additionally 2000 seconds of OFF data taken two days later are available.

No optical telescope could detect the afterglow and thus no direct measurement of the redshift is available, however a temptative measurement by the XMM-Newton collaboration exists yielding $z = (0.4 - 2.6)$ with a best fit value at $z = 0.55$ [3].

For our analysis, we were using the GRB050713a ON and OFF data and additionally Mrk501 flare data from July 1^{st} to test our analysis on a strong signal taken under the same telescope conditions, however with a much lower zenith angle (14-°-24°). For completeness, also a dedicated run triggering on sparks from the closed MAGIC camera was analyzed. Table 1 lists the used data sets. Unfortunately, the GRB050713a ON data was taken with a lower discriminator threshold ($DT = 32$) than the OFF data ($DT = 40$).

Moreover, 122850 calibrated MC simulated gamma shower events were used for the Mrk501 reference analysis, 61042 events simulated with a point spread function of $PSF(\sigma) = 0.05°$ were used for the GRB050713a analysis and another 53571 events, simulated with $PSF(\sigma) = 0.07°$, for the study of systematic effects due to possible degradations of the point spread function when the not yet so extensively tested lookup-tables mode was used by the AMC.

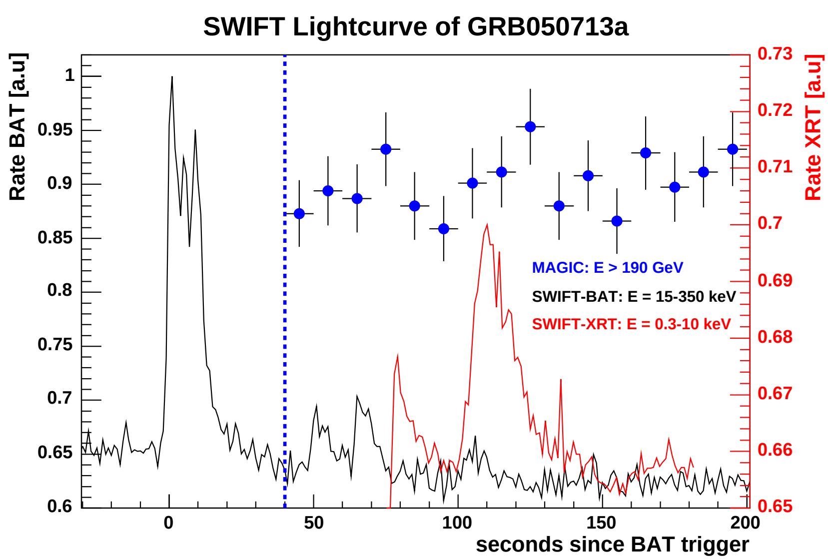

Figure 1: Light curve of GRB050713a. In black, the BAT light curve in gamma-rays; in red, the XRT light curve in X-rays [4]. The blue line shows the start of the observation with MAGIC. The blue points show the event rate (in 10 sec bins) of MAGIC after all cuts.

2.2 Calibration and Image Cleaning

All data was calibrated with the standard procedure using Mars version V0-10-8, except for some relatively small modifications:

- The global extraction window was enlarged according to Patricia's findings about the trigger cell timing offsets [5].
- An exclusion limit for arrival time fluctuations was enforced.
- Quite some pixels were excluded explicitly, listed in table 2.
- All excluded pixels were also excluded explicitly in the MC simulation data.
- The calibration constants were taken from the interleaved calibration events taken from the last run of the source observed just before the GRB alert occurred.

After this procedure, the gross camera inhomogeneity documented in [5] has gone and only two to three much smaller voids are seen in the center-of-gravity distributions (figures 12 and 13).

We cleaned all data using four different image cleaning algorithms:

1. Absolute cleaning with thresholds of 10 and 5 photo-electrons
2. Absolute cleaning with thresholds of 7 and 4 photo-electrons
3. An algorithm using a combination of absolute charge levels and the FADC time information, provided by Nepomuk Otte
4. An algorithm using a combination of relative charge levels w.r.t. pedestal fluctuations and the FADC time information developed by Markus Gaug

The last algorithm also modifies the calculation of second moments of the cleaning images: It weights every pixels with the charge elevated by 1.5 instead of 1.0, as the three others.

2.3 Data Reduction

The data was reduced in three steps: First, a couple of pre-cuts were applied to the data, namely:

- A strong cut in $SIZE$ (eq. 1) removing all events with $SIZE > 400$ photo-electrons (see figures 15 and 16). This cut ensures that the subsequent analysis was entirely focussed on low-energy events.
- A strong cut in $DIST$ (eq. 2), also focusing the analysis on low energies (see figures 17 and 18).
- Further cuts using the parameter $CONC$ (eq. 3) to eliminate the events triggered by sparks in parts of the camera (see figures 19, 20 and 21).
- Further weak cuts on the number of islands, the leakage and the number of core pixels (eq. 6).

Tables 4 and 5 list the efficiencies of the applied cuts where already a higher efficiency at low energies can be observed for the image cleaning algorithms using the time information.

The distributions in $SIZE$ do not agree between GRB050713a ON and OFF data, as shown in figure 22. We decided therefore to use only parts of the ON data for the subsequent step where the $HADRONNESS$ parameter was calculated by training matrices with the use of about one third of the simulated gamma sample. A different training was performed with the help of another third if the simulated gamma events to obtain an energy estimation parameter ($ENERGY$). The parameters used for the calculation of $HADRONNESS$ were: $SIZE$, $LENGTH$, $WIDTH$, $CONC$, $CONC4$, $DIST$ and sign(cos($DELTA \cdot ALPHA$))*$M3LONG$. Distributions of each of these parameters are found in chapter 8. It seems that the relative importance of the $CONC$ and especially $CONC4$ parameter increases of the time image cleanings are used (figures 31, 38 and 39).

The matrices were then applied to all data and distributions of $HADRONNESS$ and $ENERGY$ are obtained (see figures 40 and 49). A global energy resolution of about 34% was obtained below 200 GeV and of 28% above for the GRB050713a analysis. After investigation of the reduced data sets, slightly more stringent cuts were applied on $DIST$, $SIZE$ and the number of $ISLANDS$, explained in chapter 9 and found in eq. 9 and 12.

In a final step, cuts on the $ALPHA$ and $HADRONNESS$ parameter were evaluated simultaneously by optimizing the significance obtained from simulated gammas and the corresponding data set used as background. The resulting parameters are listed in table 6 for the Mrk501 analysis and in tables 7, 8 and 9.

An important point is that we explicitly tested all parameters entering in the calculation of $HADRONNESS$ with a gamma-rich sample of Mrk501 flare data and checked that the distributions agree between MC simulated gamma showers and real gamma showers from that source. We found that all parameters agree well, except for $CONC$ and $CONC4$ if an absolute image cleaning with levels of 7 and 4 photo-electrons is used or, in less importance, using Markus' algorithm (figures 41 to 46).

2.4 Results

We splitted the Mrk501 data in four bins of reconstructed energy: $45\,\mathrm{GeV} < ENERGY < 75\,\mathrm{GeV}$ to test the smallest possible energy threshold, $60\,\mathrm{GeV} < ENERGY < 100\,\mathrm{GeV}$, $100\,\mathrm{GeV} < ENERGY < 150\,\mathrm{GeV}$ and $150\,\mathrm{GeV} < ENERGY < 300\,\mathrm{GeV}$. In the smallest energy bin, a $4\,\sigma$ signal was found at a mean energy of 65 GeV using Markus' image cleaning and a $3.8\,\sigma$ signal at a mean energy of 61 GeV using Nepomuk's algorithm. Between 60 and 100 GeV reconstructed energy, we find already a $4.9\,\sigma$ and $5.5\,\sigma$ excesses at mean simulated shower energies of 78 GeV for the two image cleaning algorithms (see figure 2). Table 6 lists all the relevant parameters resulting from the Mrk501 test analysis, leading to the conclusion that our analysis is very sensitive at low energies.

The GRB050713a data was analyzed in four ways:

1. Taking the first 90 s of observation which correspond to the prompt emission phases in either the BAT and/or the XRT instrument on SWIFT. The remaining six runs (starting at about 7.7 min after start) as OFF data.
2. Taking the first three runs (about 16 min) as ON data and the rest as OFF data.
3. Taking the entire ON data, compared with the dedicated OFF data taken two days later.
4. Searching in time bins of 100 s ON data, using the data outside the corresponding time bin as OFF data.

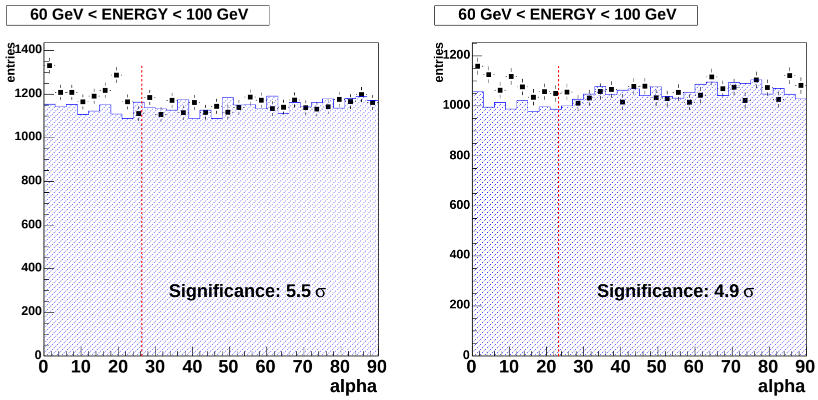

Figure 2: Distributions of the parameter $ALPHA$ for the Mrk501 data, obtained with the Nepomuk's time image cleaning (left) and Markus' image cleaning (right). The distributions are obtained in the bin $60\,\mathrm{GeV} < ENERGY < 100\,\mathrm{GeV}$ yielding a mean simulated gamma shower energy of 78 GeV.

None of these four searches yielded a significant excess over background (see tables 7, 8, 9 and 16 for a full listing of all parameters), data analyzed with Nepomuk's image cleaning algorithm yielded the lowest energy threshold (150 GeV), followed by Markus' algorithm (161 GeV). Upper limits were placed starting from the observed number of excess events and the number of background events in the same "signal" region of the alpha distribution. In order to determine the 99% CL upper limit on the number of events in each energy bin, we followed the approach outlined in [10]. The upper limit was calculated using different power law test spectra and folding them with the distribution of effective areas in the corresponding bin of reconstructed energy. All relevant formulae are outlined in chapter 9.4 and 9.5.

The resulting differential limits (tables 10, 11 and 12) differ by maximally 20% if the spectral index changes from -1 to -3. Integral limits (tables 13, 14 and 15) differ even less. Also the change of the point spread function from $0.05°\sigma$ to $0.07°\sigma$ changes the limits by maximally 40%, although both analyses calculate the $HADRONNESS$ and $ALPHA$ cuts independently.

At last, a search for peak emission in steps of 100 seconds was performed. To do so, the entire GRB050713a data sample was divided in 22 slices of equal time duration (of 101 seconds). Only Nepomuk's image cleaning was used for the analysis, every of the time slices was taken as ON data while the surrounding data set was used as OFF data. A second search was performed shifting the phase of the time slice by 50 seconds. Figure 4 shows the distributions of obtained significances, with and without phase shift.

The number of excess events are distributed in general randomly over time, as can be seen in figure 5.

Further systematic uncertainties were investigated concerning less efficient parts of the camera due to trigger inefficiencies and absolute calibration errors. Including these effects raise all upper limits by about 20%. Finally, the following differential upper limits were obtained, including statistical and systematic uncertainties:

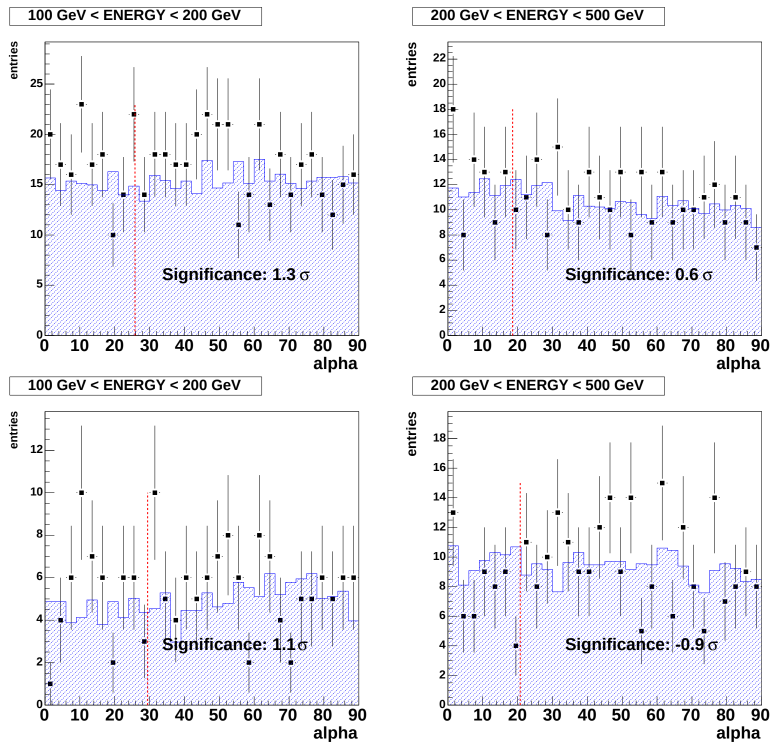

Figure 3: Distributions of the parameter $ALPHA$ for the 90 s of the prompt GRB emission, obtained with the Nepomuk's time image cleaning. The four plots correspond to two slices of the $ENERGY$ parameters: Left: 100 to 200 GeV and right: >200 GeV reconstructed energy; Top: with cuts optimized using $PSF = 0.05°\sigma$, bottom: using $PSF = 0.07°\sigma$. The red line indicates the region where a possible signal is expected.

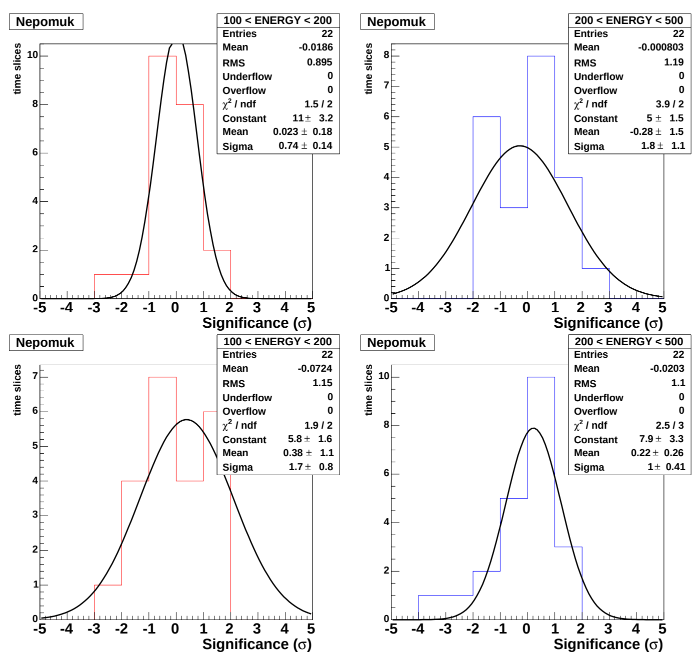

Figure 4: Distributions of the obtained significances during the peak search. Left: 100 to 200 GeV reconstructed energy, right: 200 to 500 GeV reconstructed energy. Top: Starting from $T = 0$ s, bottom: times shifted by half a period, starting from $T = 50$ s.

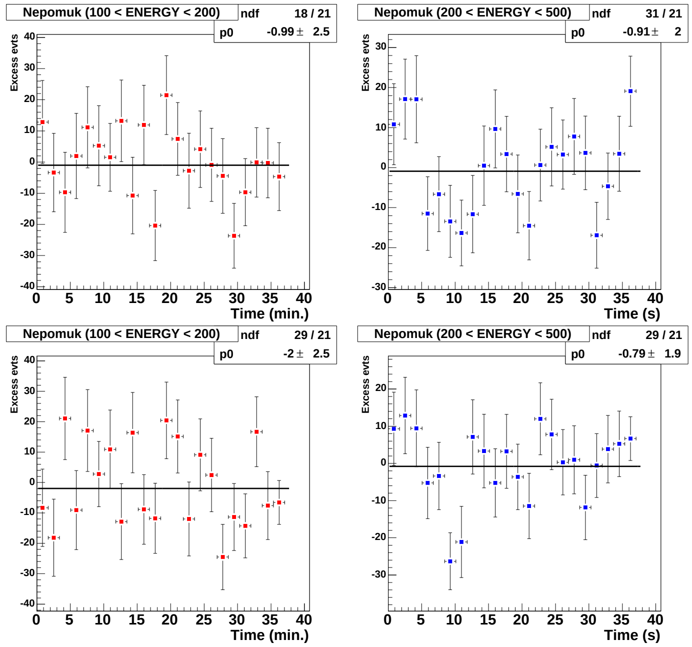

Figure 5: Number of excess events vs. time for the peak search. Left: 100 to 200 GeV reconstructed energy, right: 200 to 500 GeV reconstructed energy. Top: Starting from $T = 0\,\mathrm{s}$, bottom: times shifted by half a period, starting from $T = 50\,\mathrm{s}$.

$$
\begin{array}{llll}
< \dfrac{d\Phi}{dE} > |_{150\,\mathrm{GeV}} & < \; 1.3 \cdot 10^{-17}\ \mathrm{ph/cm^2/keV/s} & \equiv \; 3.6\,\mathrm{C.U.} & \text{first } 90\,\mathrm{s} \\
< \dfrac{d\Phi}{dE} > |_{150\,\mathrm{GeV}} & < \; 4.1 \cdot 10^{-18}\ \mathrm{ph/cm^2/keV/s} & \equiv \; 1.1\,\mathrm{C.U.} & \text{first } 1000\,\mathrm{s} \\
< \dfrac{d\Phi}{dE} > |_{150\,\mathrm{GeV}} & < \; 2.4 \cdot 10^{-18}\ \mathrm{ph/cm^2/keV/s} & \equiv \; 0.7\,\mathrm{C.U.} & \text{entire } 2223\,\mathrm{s} \\
< \dfrac{d\Phi}{dE} > |_{150\,\mathrm{GeV}} & < \; 1.8 \cdot 10^{-17}\ \mathrm{ph/cm^2/keV/s} & \equiv \; 4.9\,\mathrm{C.U.} & \text{any } 100\,\mathrm{s} \text{ interval} \\
 & & & \\
< \dfrac{d\Phi}{dE} > |_{280\,\mathrm{GeV}} & < \; 2.3 \cdot 10^{-18}\ \mathrm{ph/cm^2/keV/s} & \equiv \; 3.2\,\mathrm{C.U.} & \text{first } 90\,\mathrm{s} \\
< \dfrac{d\Phi}{dE} > |_{280\,\mathrm{GeV}} & < \; 7.7 \cdot 10^{-19}\ \mathrm{ph/cm^2/keV/s} & \equiv \; 1.1\,\mathrm{C.U.} & \text{first } 1000\,\mathrm{s} \\
< \dfrac{d\Phi}{dE} > |_{280\,\mathrm{GeV}} & < \; 5.3 \cdot 10^{-19}\ \mathrm{ph/cm^2/keV/s} & \equiv \; 0.7\,\mathrm{C.U.} & \text{entire } 2223\,\mathrm{s} \\
< \dfrac{d\Phi}{dE} > |_{280\,\mathrm{GeV}} & < \; 4.8 \cdot 10^{-18}\ \mathrm{ph/cm^2/keV/s} & \equiv \; 6.6\,\mathrm{C.U.} & \text{any } 100\,\mathrm{s} \text{ inverval}
\end{array}
$$

The crab unit (C.U.) was thereby assumed to be: $1\,\mathrm{C.U.} := 1.5 \cdot 10^{-3} \left(\frac{E}{\mathrm{GeV}}\right)^{-2.58} \mathrm{ph/cm^2/TeV/s}$, measured by MAGIC and fitted from 300 GeV to 5 TeV. These limits include systematic uncertainties due to possible degradations of the point spread function, trigger inefficiencies in parts of the camera, changes in the limits due to the unknown spectral index and a global 10% uncertainty in the absolute calibration. Even including these systematics, the limit in the upper energy bin results to be about a factor four better than the one presented by N. Galante and A. Stamerra in [1]. However, their paper quotes an “error on the limit”, so our limit lies within $2.5\,\sigma$ of their presented uncertainty. This is somehow expected since we developped a dedicated low-energy analysis with the aim to improve sensitivity. The limit in the lower energy bin cannot be compared directly with their results since their analysis does not reach down so far in energy.

Finally, a semi-independent $DISP$-analysis was performed, using the similar, but not the same, parameters to calculate the $HADRONNESS$. Slightly different cuts were used there and a final cut on the parameter θ^2. Comparing these two analysis yield generally higher energy thresholds for the $DISP$-analysis (about 5 GeV for the GRB050713a prompt emission search), but comparable sensitivity and upper limits at higher energies. We noted that the so-called "ghost-busting" efficiency goes down to 0.5 at very low energies and may be responsible for the higher threshold in energy.

3 Introduction

GRB050713a was detected on July, 13^{th}m, 2005, at 04:29:02.39 UTC by the BAT instrument on the SWIFT satellite. It was first announced to the GCN at 04:31:34 UTC with the coordinates RA: 21h 22m, Dec: +77d 04m with an uncertainty of 3 arcmin radius [2]. The XRT and the UVOT telescopes, also located on SWIFT, found a fading source at RA: 21h 22m 09.6s, Dec: +77d 04m 30.3s. The MAGIC telescope received the alert while it was observing a Galactic source (OFF-Sadr) and started observing the position 40 sec. after the onset of the burst ($T0$). While the brightest part of the keV emission ocurred at $T0 + 20s$, three smaller peaks followed at $T0 + 50$s, $T0 + 65$s and $T0 + 105$s, thus after the start of the observation of MAGIC (see figure 6).

The burst position was observed during 2223 seconds, two days later, another 2000 seconds of dedicated OFF data was taken at the same position. Its location lies outside the Galactic plane and no bright stars are found in the field-of-view of the MAGIC camera.

Unfortunately, no optical telescope could detect the afterglow and measure the redshift directly. However, the XMM-Newton collaboration performed a fit to the observed afterglow spectrum in X-rays, containing a redshifted absorber component. With this method, the best fit value for the redshift comes out to be $z = 0.55$ with the 90% CL ranges of $z = (0.4 - 2.6)$ [3].

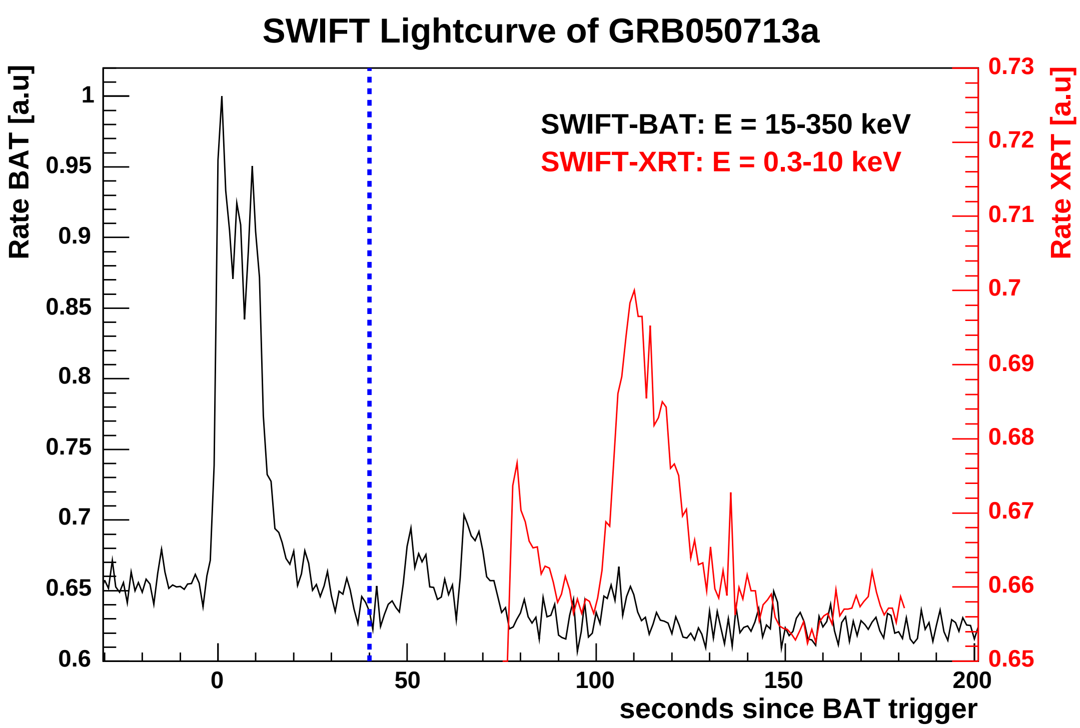

Figure 6: Light curve of GRB050713a. In black, the BAT light curve in gamma-rays; in red, the XRT light curve in X-rays [4]. The blue line shows the start of the observation with MAGIC.

We expect thus the gamma-ray horizon to lie somewhere between 100 and 200 GeV, at energies above which possible gamma rays are mainly aborbed by collisions with the meta-galactic radiation field. An analysis dedicated on the lowest possible energy threshold is therefore desired to extract some physical meaning to a given signal or an upper limit.

4 The Data Samples

This chapter contains information about the data files which were used for the analysis of the Gamma-Ray Burst GRB050713a. These are the following samples:

- GRB050713a: ON and OFF
- Two samples of Monte-Carlo simulated gamma showers from GRB050713a:
    1. Period 21 with $0.05°\sigma$
    2. Period 25 with $0.07°\sigma$
- Markarian 501: ON and OFF
- Monte-Carlo simulated gamma showers from Markarian 501
- Two dedicated spark runs

Table 1 lists all the run numbers used for this analysis.

Unfortunately, the OFF-data for GRB050713a was taken with a different discriminator threshold (DT) compared with the ON-data. We believe that this discrepancy occurred because the source observed previous to GRB050713a was a galactic source, taken with $DT = 40$. When the GRB alert occurred, the discriminator thresholds were not set back to the value, usually used for extra-galactic sources ($DT = 32$), in order not to lose any time. Two days later, the shifters took the Off-GRB050713a data applying the discriminator thresholds of $DT = 32$ because they saw that it was an extra-galactic source. From the different DT's follow also different raw trigger rates (see figure 7). Figure 10 shows the distributions of ("fundamental") pedestal RMS for the GRB050713a data sets. One can see here also that the mean pedestal RMSs are different between ON and OFF data. Moreover the spread in pedestal RMS is much bigger for the data samples than the one used in the simulation, a discrepancy already known since a long time.

In the course of this analysis, more fundamental discrepancies will be found between the two data sets, and we predict already at this point that we could not make much use of the OFF data, therefore.

A similar problem occurred when observing Mrk501: During the observation, the shifters realized that the rates had passed 400 Hz and thought it would be safer to raise the discriminator thresholds. Therefore, the Mr501 ON data set is also split into two parts: About 20 minutes taken with $DT = 32$ and another half an hour taken with $DT = 40$. Apart from that problem, the Mrk501 data resulted to be of very good quality, except for the Off-data taken on July, 6^{th}.

Information	Start		End	Runtype	Day	zd. angle			DT	Remarks
GRB050713a										
calibration	61317			P	2005-07-13	25			40	Off-Sadr ped. run
	61318			C						Off-Sadr cal. run
	61344			D						Off-Sadr interl. cal.
target	61345	-	61351	D		49	-	50		
GRB050713A OFF data										
calibration	61529			P	2005-07-15				32	
	61530			C						
off target	61531	-	61544	D		49	-	50		
Markarian501										
calibration	59833			P	2005-07-01				32	
	59832			C						
target	59834	-	59839	D		21	-	24	32	extra-galactic DT
	59840	-	59851	D		14	-	21	40	galactic DT
Markarian501 OFF data										
calibration	59711			P	2005-06-29				32	
	59712			C						
target	59713	-	59718	D		15	-	24		
	59720	-	59723	D		12	-	15		
calibration	59938			P	2005-07-02				32	
	59939			C						
target	59940	-	59948	D		16	-	20		
calibration	60397			P	2005-07-06				32	
	60398			C						
target	60399	-	60412	D		16	-	23		
calibration	60630			P	2005-07-08				32	
	60631			C						
target	60632	-	60637	D		15	-	18		excluded 60636
Spark Events										
calibration	52634			P	2005-04-11				32	TeV-L3+C ped. run
	52635			C						TeV-L3+C cal. run
	52630			P						pedestal run
	52632			P						pedestal run
	52631	-	52633	D						spark runs

Table 1: Collection of the data samples used for this analysis. P stands for "Pedestal Run", C for "Calibration Run", D for "Data Run" and DT for "Discriminator Threshold".

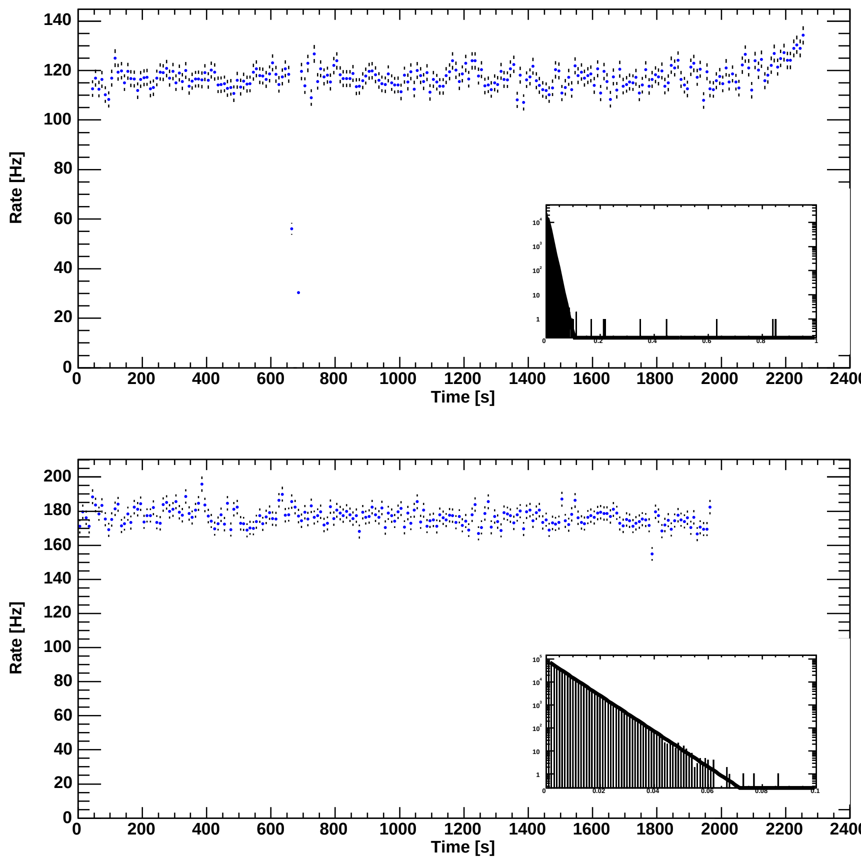

Figure 7: Raw Event Rates of GRB050713a (top) and OffGRB050713a (bottom) after suppression of the interleaved calibration events. The inset shows the distribution of time differences between consecutive events.

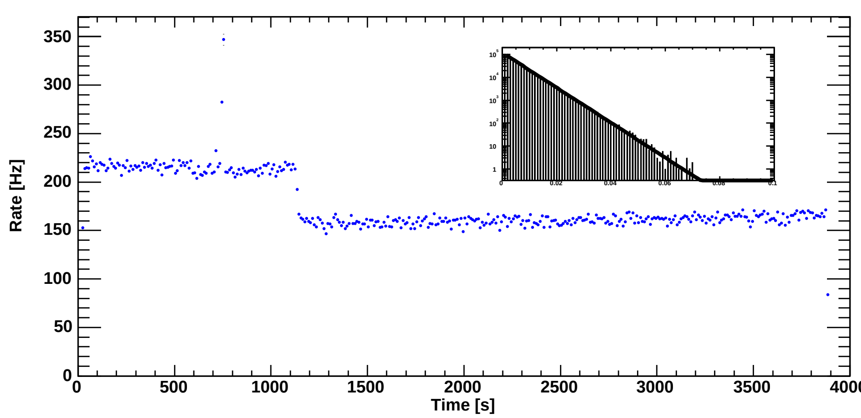

Figure 8: Raw Event Rates of Mrk501 ON data, taken on July, 1^{st}, 2005. The decrease in rate happens when the shifters decided to increase the discriminator thresholds.

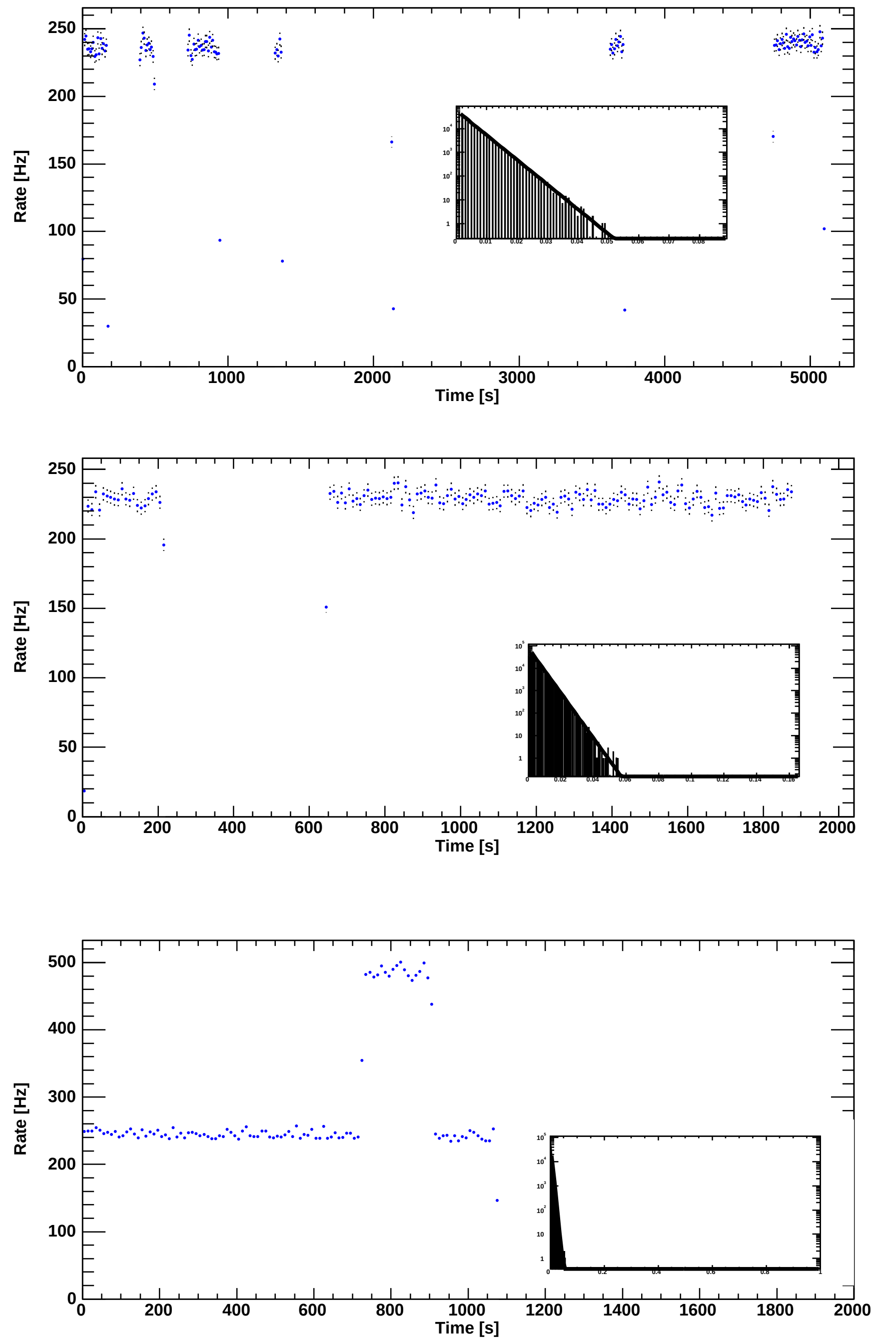

Figure 9: Raw Event Rates of Mrk501 OFF data: Top: data, taken on June, 29^{th}, 2005; center: data, taken on July, 2^{nd}, 2005; bottom: data, taken on July, 8^{nd}, 2005. The period with the high rates corresponds to run 60636 which was excluded. The insets show the distribution of time differences between consecutive events.

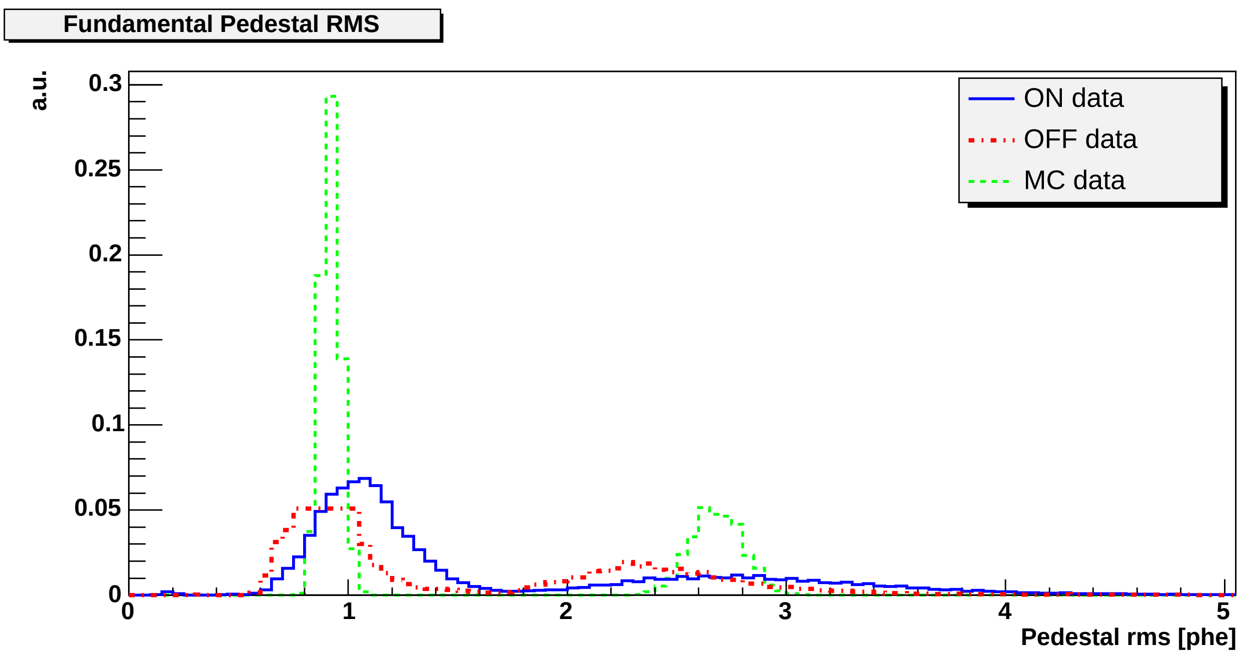

Figure 10: Distributions of the pedestal RMS for the GRB050713a data sets.

5 Calibration

The calibration of a GRB data set is slightly different from the standard calibration due to the fact that there is no time to pedestal and calibration runs before the source is observed. Instead, we have the interlaced calibration events from the previous source observation which we can use to calibrate the first minute of the GRB data set. It would not be a big issue wasn't it for the fact that the first minute is the most important part of the data set, the time where the signal expectation is highest.

We describe in the following a rather detailed procedure of how we calibrated the data, mainly because other GRB data sets should be treated in the same way.

5.1 Modifications and Bugs

We used the ***MARS release V0-10-8*** with digital filter to extract and calibrate all data. This release was especially made after we had found and eliminated a couple of bugs:

1. All MARS releases of the V0-10 family do not yet have an entirely automized Monte Carlo file recognition. This concerns the weights for the digital filter (which are different for the MC) and the high-gain vs. low-gain inter-calibration (which are also different for the MC). We fixed therefore the callisto_mc.rc file used by Pratik Majumdar and committed it to the CVS.

2. We had found that the reader of the calibrated Cherenkov photon container ("MReadMarsFile" reading "MCerPhotEvt") set the flag "core pixel" to true if ROOT version 3.05.07 is used, compiled with gcc-3.3. The subsequent image cleaning classes set this flag if a pixel charge exceeds the first threshold ("cleaning level 1"), but do not reset it ***before*** applying the cleaning level 1. In the case that the flags are not set to zero before the image cleaning starts, individual island pop up in the cleaned image and distort the Hillas parameters. We could not see such an effect with ROOT-3.10, but did not have the time to test the bug in more detail. Instead, we chose to reset the "core-pixel" flag before starting any image cleaning operation.

3. After Patricia's investigations about the inhomogenities of the trigger cell timing windows [5], we decided to make the global extraction window larger. This means, modifying the following parameters in ***callisto.rc***:

   - MJPedestalY2.ExtractWinLeft: 4.5
   - MJPedestalY2.ExtractWinRight: 5.0

4. As there were about five pixels with rather large arrival time fluctuations during the calibration runs, we made one exclusion limit more stringent:

   - MJCalibration.MCalibrationChargeCalc.ArrTimeRmsLimit: 1.7

   All pixels fluctuating with more than 1.7 FADC slices RMS with respect to the calibration trigger were thus excluded.

5. We calibrated the Monte Carlo simulation files excluding the same pixels as those excluded by the data files calibration.

5.2 Extracting the conversion factors from the interlaced calibration events of the previous source

First, we calibrated the data file nr. 61344 taken off-source Sadr using its own pedestal and calibration file. The interlaced calibration constants are then getting stored in a ***signal00061344.root***-file. From that file, the calibration constants can be retrieved. The procedure has been made automatic in the current Mars-Development branch using the option:

- callisto –signalfile=signal00061344.root

In Mars_V0-10-8, the extraction was made by hand and the retrieved storage containers written into a separate root-file, called ***calib00061345.root***. From that moment on, the calibration of the GRB data file can be started using the flags:

- callisto -y

5.3 Excluded Pixels

Apart from the central and the blind pixel, the following pixels were excluded by the calibration:

ID	reason	ID	reason
0	central pixel	53	dead
97	fluctuation arr. times	105	very low signal, hot spot
115	very low signal, hot spot	150	very low signal, hot spot
157	dead	160	probably dead
162	very low signal, hot spot	209	dead
211	dead	230	fluctuating arr. times
239	dead	279	very low signal, hot spot
307	fluctuating gain	312	fluctuating gain
334	fluctuating arr. times	345	dead
352	very low signal, hot spot	377	fluctuation arr. times
395	no signal	419	very low signal, hot spot
420	very low signal, hot spot	472	pedestal very high
524	fluctuating arr. times	544	no signal
551	fluctuating gain	556	very low signal, hot spot
559	blind pixel supply	574	fluctuating gain

Table 2: Excluded pixels from calibration: The categories are: ***Dead***: Previously known dead pixels; ***Probably dead***: Pedestal RMS is 4.5 σ smaller than the average pedestal RMS; ***Fluctuating gains***: Previously known pixels with highly fluctuating gains; RMS of absolute arrival times is bigger than 1.7 FADC slices; ***Fluctuating arrival times***: RMS of absolute arrival times is bigger than 1.7 FADC slices; ***Very low signal, hot spot***: The mean reconstructed charge is smaller than half the mean charge average of the camera, at the same time a “hot spot” is seen at the position of the pixel after calibration of the data; ***No signal***: Mean reconstructed signal of the calibration light pulses is smaller than 3.5 pedestal RMS.

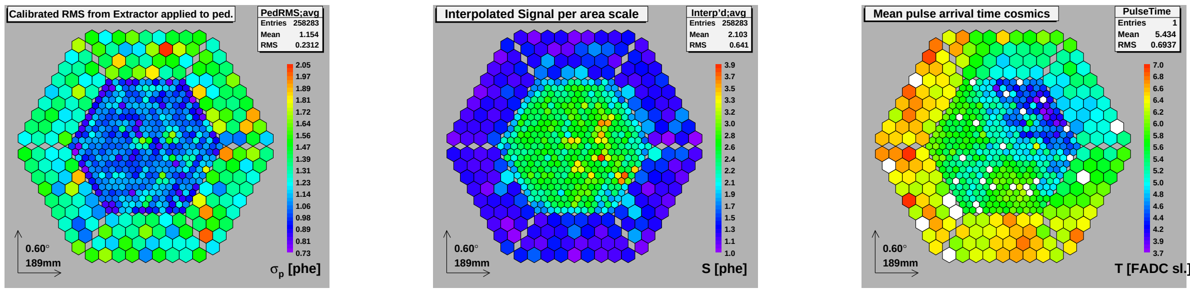

Figure 11: Results of the calibration: left: Average pedestal RMS, center: Mean interpolated signal in photo-electrons (outer pixels multiplied with 0.25), bottom: Mean signal pulse arrival time.

In total, 27 pixels were excluded plus the not equipped central pixel and the supply of the blind pixels. Table 2 gives an overview of the excluded pixels. All given exclusion reasons types were applied automatically except for the type of pixels called “Very low signal, hot spot”. These pixels were found to yield a very low signal for the calibration pulses, but then an on average much too high signal for the cosmics pulses. These pixels belong to the class of channels where the distribution of high-gain signals from the calibration pulses go into saturation too often, hence that distribution is not used, however the distribution of low-gain signals is also flaw since the low-gain switch has not been applied often enough. The reconstructed mean signal is therefore too low and the derived conversion factor too high. Actually, the development branch of MARS incorporates an automatic check for these channels. We had to exclude them “by hand” in all further analyses. Moreover, there were 37 pixels declared as “unreliable”, mostly because the χ-square of the Gauss-fit to the signal distribution was not satisfactory. We treated these channels like ordinary channels.

All excluded pixels were cross-checked with the camera hardware experts [6] and found to be identical to their list of mal-functioning pixels, except for some outer pixels.

Figure 11 shows the most important summary plots obtained from callisto. On the left side, the pedestal RMS shows that there is no obvious bright star in the field-of-view of the GRB, however about 5-6 outer pixels appear to be quite a bit noisier than the rest. This does not affect our analysis much since our cuts will remove most of the signal contained in the outer camera. The central camera of figure 11 shows the mean calibrated signal, interpolated in case of the “bad pixels”. The signals of the outer pixels were multiplied with 0.25 in order to get the camera response per pixel area unit. One can see that the camera response is flat except for the already known “spark” events and some small deficit of 5–10% at the lower right part of the inner camera, covering a group of five pixels. This deficit will remain until the end of the analysis and constitute a true inefficiency which will have to be corrected for. The right side of figure 11 shows the mean pulse arrival times for pulses exceeding a threshold of about 15 photo-electrons. The differences in the average Cherenkov signal arrival times are probably due to the time offset of the trigger cell at the upper right part of the camera (see also [5]), but do not have any effect on the signal reconstruction efficiency, as can be seen comparing figure 11 center and right. We conclude therefore that by making the extraction big enough, the inhomogenity of the camera response seems to be gone.

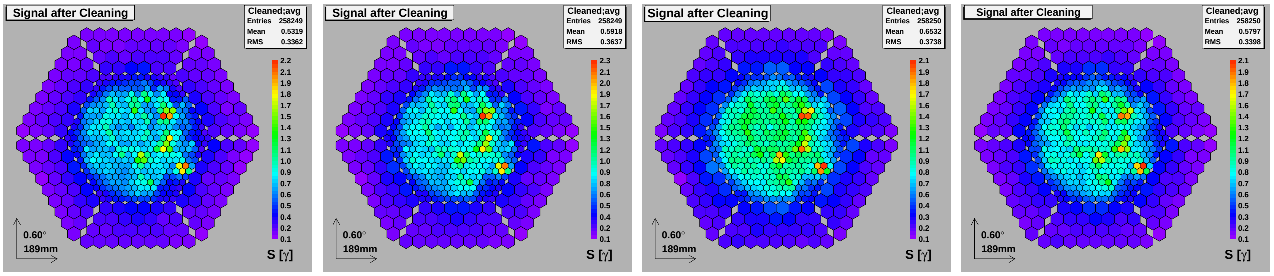

Figure 12: Averaged signal per pixel in photo-electrons after image cleaning: From left: (a) absolute cleaning with levels 10 and 5 photo-electrons, (b) absolute cleaning with levels 7 and 4 photo-electrons, (c) Nepomuk's image cleaning using times, (d) Markus image cleaning using times.

6 Image Cleaning

We cleaned all calibrated data using two standard cleaning algorithms and two new algorithms which take advantage of the pulse arrival time information – one written by Nepomuk Otte and another written by Markus Gaug. As we wanted to achieve the lowest possible threshold in energy, but have reliable and tested analysis for cross-checks, all further analysis was therefore split into four parts according to the four cleaned data samples. Table 3 lists the chosen parameters used for the four cleaning algorithms. The algorithms differ by the thresholds applied to the reconstructed charge, the time windows and later the weights used in the calculation of the moments of the statistical Hillas ellipse reconstruction: The first three algorithms weighted the first and second moments with the calibrated charge, while the last one used the charged elevated to 1.5 as weight. To do so, the Hillas algorithm was modified as shown in [7].

Algorithm	charge reference mode	charge level 1	charge level 2	time win. neighbors	global time win.	max. nr. rings	weight image par.
Abs 10 5	absolute	10 phe	5 phe	–	–	1	1
Abs 7 4	absolute	7 phe	4 phe	–	–	1	1
Nepomuk	absolute w.r.t. bias	4 phe	1 phe	1.0 ns	6.6 ns from mean isl.	4	1
Markus	scaled w.r.t. bias	3 σ	0.75 σ	2.3 ns	3.3 ns single pairs	1	1.5

Table 3: Tested image cleaning algorithms.

Figure 12 shows the averaged signal after image cleaning for the four cleaning algorithms. One can see "hot spots" which we checked to coincide all with the sparking pixels. It seems that the relative importance of the sparks to the signal is less pronounced if the time image cleaning algorithms are used. At the lower right edge of the camera and the rightmost part, clear deficits are seen within all cleaning algorithms. We checked thoroughly our calibration results for these parts of the camera, but could not find deviating behavior there. We suspect therefore that two trigger cells were not working as efficiently as the rest, but cannot prove this assumption.

Figure 13 shows the averaged center of the reconstructed ellipse ("center of gravity") after image

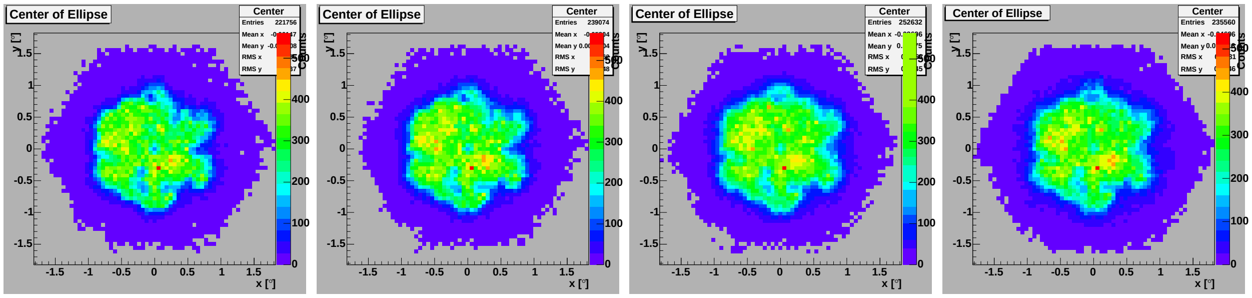

Figure 13: Average center of the reconstructed signal ellipses after image cleaning for the GRB050713a data: From left: (a) absolute cleaning with levels 10 and 5 photo-electrons, (b) absolute cleaning with levels 7 and 4 photo-electrons, (c) Nepomuk's image cleaning using times, (d) Markus image cleaning using times.

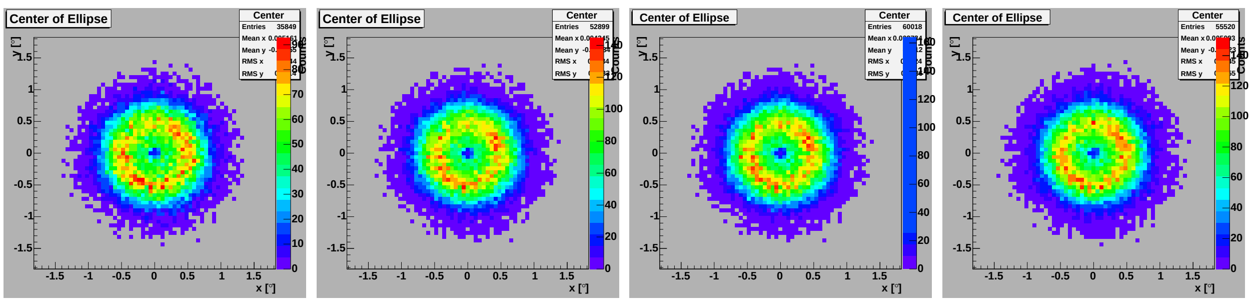

Figure 14: Average center of the reconstructed signal ellipses after image cleaning for Monte Carlo simulated gamma showers: From left: (a) absolute cleaning with levels 10 and 5 photo-electrons, (b) absolute cleaning with levels 7 and 4 photo-electrons, (c) Nepomuk's image cleaning using times, (d) Markus image cleaning using times.

cleaning for the four cleaning algorithms. One can see that the camera gets illuminated more uniformly when decreasing the threshold.

From figures 12 and 13, one can conclude that the large inefficiency observed in the upper right part of the camera, obtained in previous analyses seems to be gone completely. This conclusion was already foreseeable given the results obtained in the previous chapter which indicated that the larger extraction window effectively removes the gross inefficiency. However, two to three smaller voids remain at the upper right part, the rightmost part and the lower right part of the inner camera. The importance of these voids decreases however with usage of the time image cleanings. The reason for these inefficiencies is still unclear to us, and we did have time to investigate this issue in further detail. In later chapter, we will see that the inefficiency is very energy-dependent. It will be taken into account in the derivation of an upper limits.

7 Cuts

In this section, we describe the cuts applied to the data, before random forest and energy estimation is performed. These cuts are thought to be either necessary in any case (e.g. to exclude the "spark events" or to make the alpha-distribution flat) or they are so loose that practically no signal loss can be expected. We obtain then a cleaned data sample which we can use for cross-checks and as input to the following analysis steps.

7.1 SIZE

As we are only interested in low-energy events, we apply a strong cut on the parameter $SIZE$:

$$60\,\text{p.e.} < SIZE < 400\,\text{p.e.} \tag{1}$$

The lower $SIZE$ limit is simply due to the fact that we could never observe any signals below 70 photo-electrons, so a cut on 60 p.e. was therefore considered to be safe. Concerning the upper limit, we wanted to perform a dedicated training of cuts on low energy events. This cut makes an important difference to previous analyses since we do not expect to achieve good gamma-hadron separation efficiencies above this $SIZE$ value.

Figures 15 and 16 show the distributions of $\log(SIZE)$ for the GRB050713a and the Mrk501 data samples, respectively, together with the region which is left after the $SIZE$ cut. Like in following plots, the results of all four image cleaning algorithms are shown for comparison.

In the case of the distributions obtained with the GRB050713a data, one can see that unfortunately, the ON data sample distribution is shifted with respect to the distribution obtained from the OFF data sample, certainly because of the different discriminator threshold settings. Shown in figure 15 is also the distributions obtained from simulated gamma showers with the naively assumed point-spread function (PSF) of 0.05° FWHM (histogram "MC") and another one with the slightly worse PSF of 0.07° FWHM (histogram "MC (PSF)"). A loss of events at low sizes can be observed if the PSF worsens.

Figure 15 shows also a lower gamma efficiency if the absolute image cleaning using thresholds of 10 and 5 photo-electrons is used. As expected, the efficiency is highest for the image cleaning algorithms requiring time coincidences, especially if Nepomuk's algorithm is used.

Figure 16 shows the distributions of $\log(SIZE)$ for the Mrk501 data sample. Here, the ON data sample distributions agree nicely with the ones obtained from the OFF data sample, if the data taken with the lower discriminator thresholds are taken, otherwise a shift is obtained, similar to one observed in figure 15.

The $\log(SIZE)$ distributions of both data samples, figures 15 and 16 show a strange bump between 300 and 1000 photo-electrons, less pronounced with the absolute image cleaning using 10 and 5 photo-electrons. The origin of this bump has not yet been investigated, but should raise some concern.

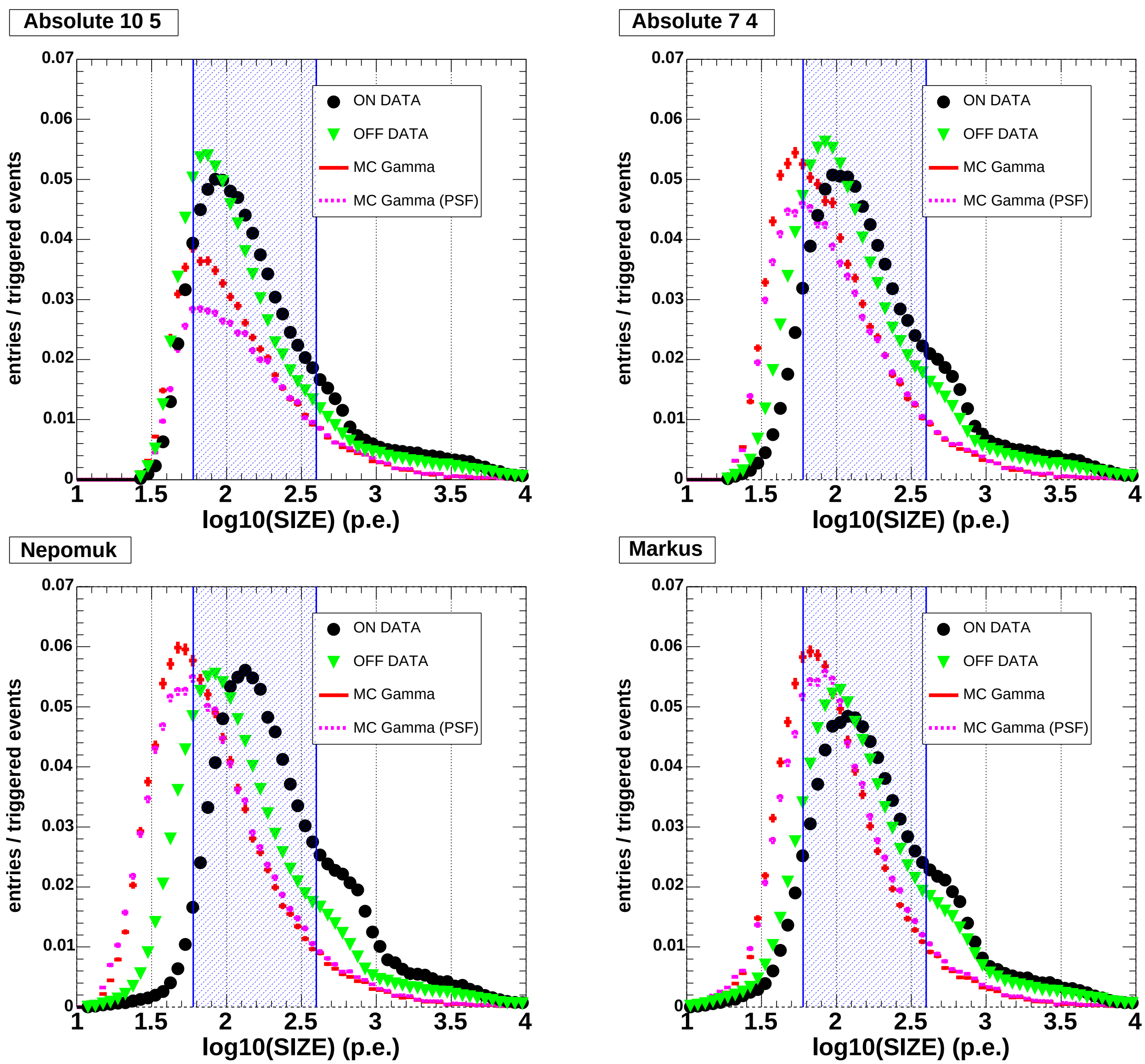

Figure 15: Normalized distributions of the parameter $\log(SIZE)$ for the various image cleaning algorithms and the GRB050713a data. The blue lines show the cuts applied previous to the further analysis: $60\,\text{p.e.} < SIZE < 400\,\text{p.e.}$. Top left: absolute cleaning with levels 10 and 5 photo-electrons, top right: absolute cleaning with levels 7 and 4 photo-electrons, bottom left: Nepomuk's image cleaning using time coincidence, bottom right: Markus image cleaning using time coincidence.

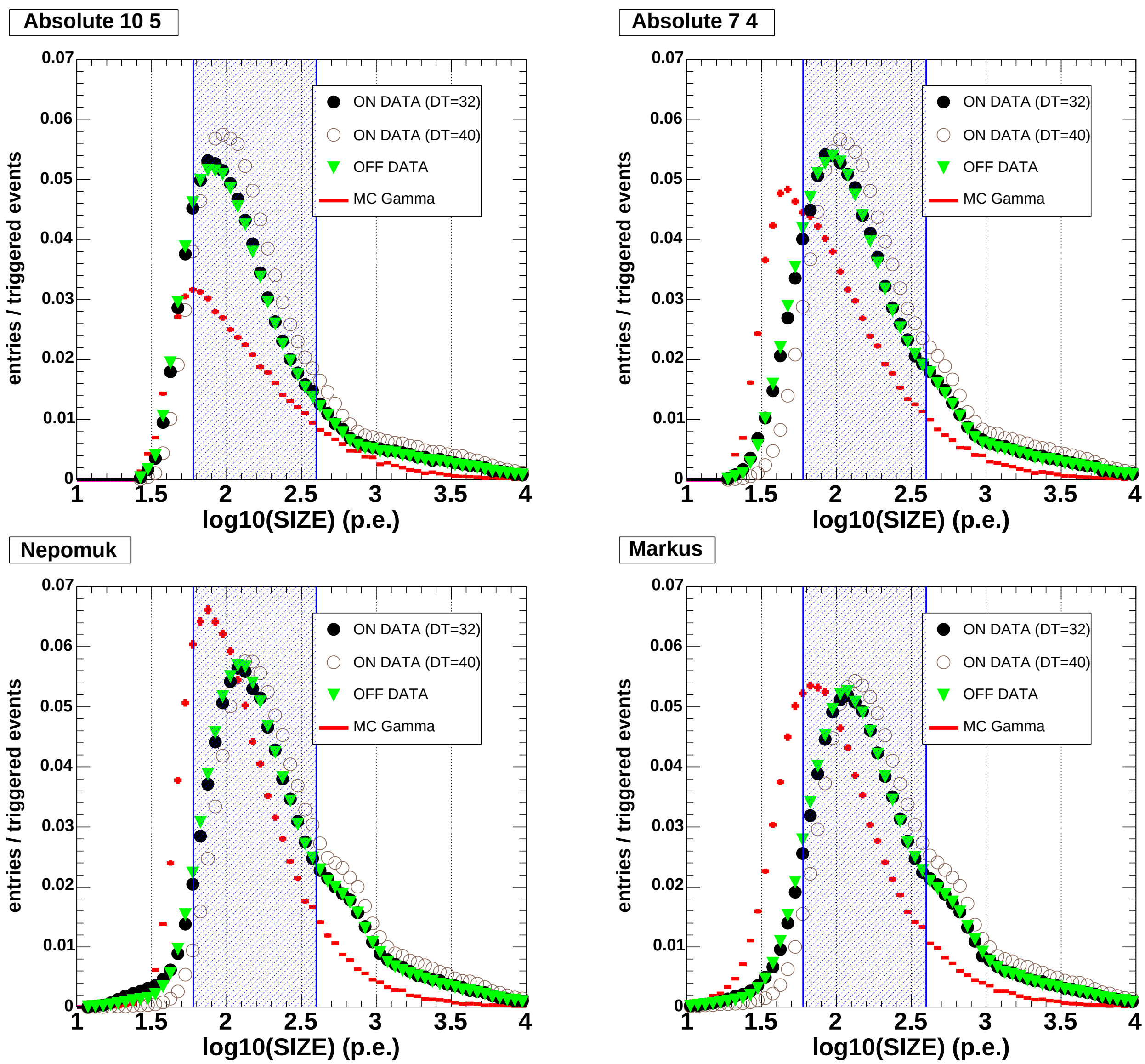

Figure 16: Normalized distribution of the parameter $\log(SIZE)$ for the various image cleaning algorithms and the Mrk501 data. The red lines show the cuts applied previous to the further analysis: $60\,\mathrm{p.e.} < SIZE < 400\,\mathrm{p.e.}$. Top left: absolute cleaning with levels 10 and 5 photo-electrons, top right: absolute cleaning with levels 7 and 4 photo-electrons, bottom left: Nepomuk's image cleaning using time coincidence, bottom right: Markus image cleaning using time coincidence.

7.2 DIST

It is necessary to make a cut on the $DIST$ parameter, mainly because of an observed higher trigger efficiency for events with a low $ALPHA$-parameter at the edges of the trigger area of our camera [8]. Including these events would result in an excess of ON- and OFF data at low $ALPHA$ values. Also, events at low $DIST$ cannot be reconstructed properly and show almost flat alpha-distributions. From inspection of the alpha-distributions after preliminary analysis, we concluded that a strong cut on $DIST$ was necessary since the beginning of the analysis:

$$0.33 < DIST < 0.86 \tag{2}$$

Note that the $DIST$ variable has the units "degree (°)". In order to transform what is obtained from the MARS parameter container "MHillasSrc.fDist" to $DIST$, we divided by a factor 297 °/cm. Figure 17 and 18 show the distribution of the $DIST$ parameter versus the logarithm of $SIZE$, together with the applied cuts for the GRB050713a and the Mrk501 data samples, respectively. One can see that the cuts on $DIST$ remove some of the MC-simulated gamma signal, however relatively much more of the ON and OFF data since the maximim of their $DIST$ distributions lies at a higher value. It is also clearly visible that the mean $DIST$ for the expected gamma signals is lower using for GRB050713a data than for the Mrk501 data, an effect of the different zenith angle. For this reason, the final (even tighter) cuts on $DIST$ will be slightly different for the data samples.

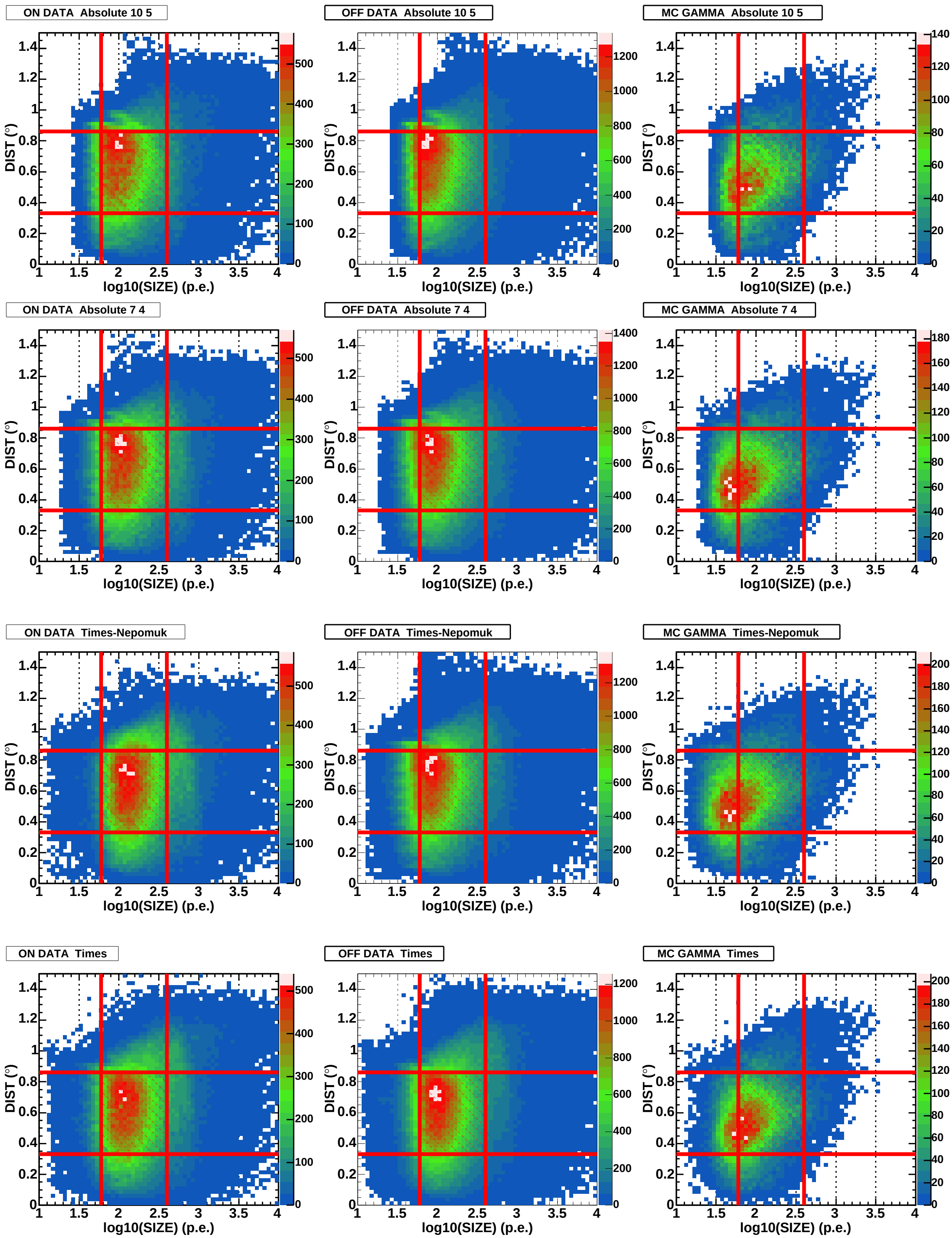

Figure 17: Distributions of the parameter *DIST* for the various image cleaning algorithms and the GRB050713a data. The red lines show the cuts applied previous to the further analysis: $0.33 < DIST < 0.86(^\circ)$. First: absolute cleaning with levels 10 and 5 photo-electrons, second: absolute cleaning with levels 7 and 4 photo-electrons, third: Nepomuks image cleaning using times, bottom: Markus image cleaning using times.

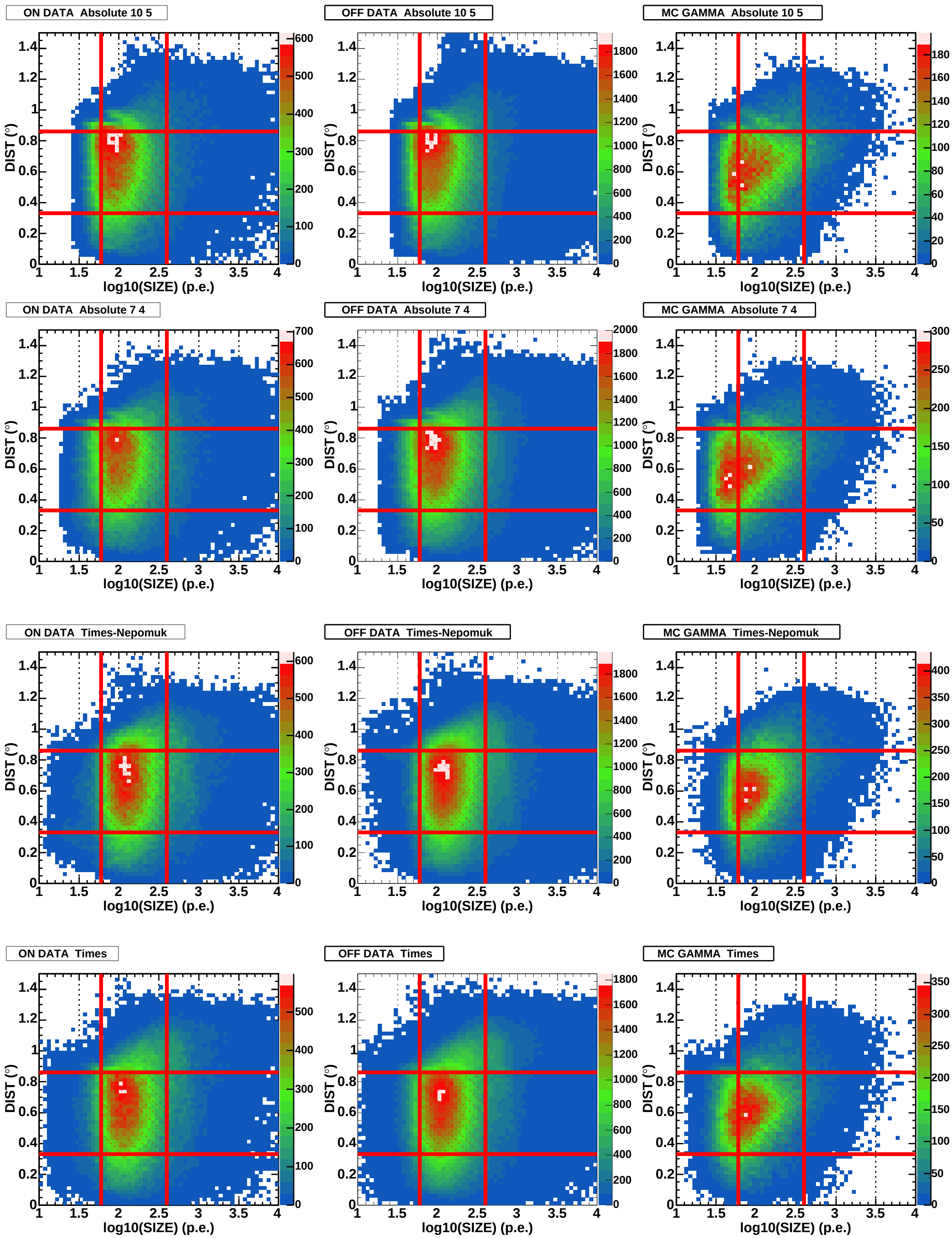

Figure 18: Distribution of the parameter dist for the various image cleaning algorithms and the Mrk501 data. The red lines show the cuts applied previous to the further analysis: $0.33 < DIST < 0.86(°)$. Top: absolute cleaning with levels 10 and 5 photo-electrons, second: absolute cleaning with levels 7 and 4 photo-electrons, third: Nepomuks image cleaning using times, bottom: Markus image cleaning using times.

7.3 CONC

With an energy-dependent cut on the parameter $CONC$, one can remove the spark events which otherwise seriously affect the analysis. Unfortunately, the Monte-Carlo simulated events and the real data do not always agree too well in the parameter $CONC$ [9]. We want to show however in the following figures that we found a way to remove almost all spark events without cutting away signal:

$$\log(CONC) < 0.65 - 0.45 \cdot \log(SIZE) \tag{3}$$

Figures 19 and 20 show the applied cut in the $\log(CONC)$ vs. $\log(SIZE)$ plane for the GRB050713a and the Mrk501 data, respectively. One can see that almost no (simulated) signal is cut away, but also hardly any real data events, except for the branch at the right upper part of the distributions which are due to the sparking events.

Figure 21 shows the cut applied to the spark events data. Almost all events are removed, either by the cut on $\log(CONC)$ or the one on $SIZE$.

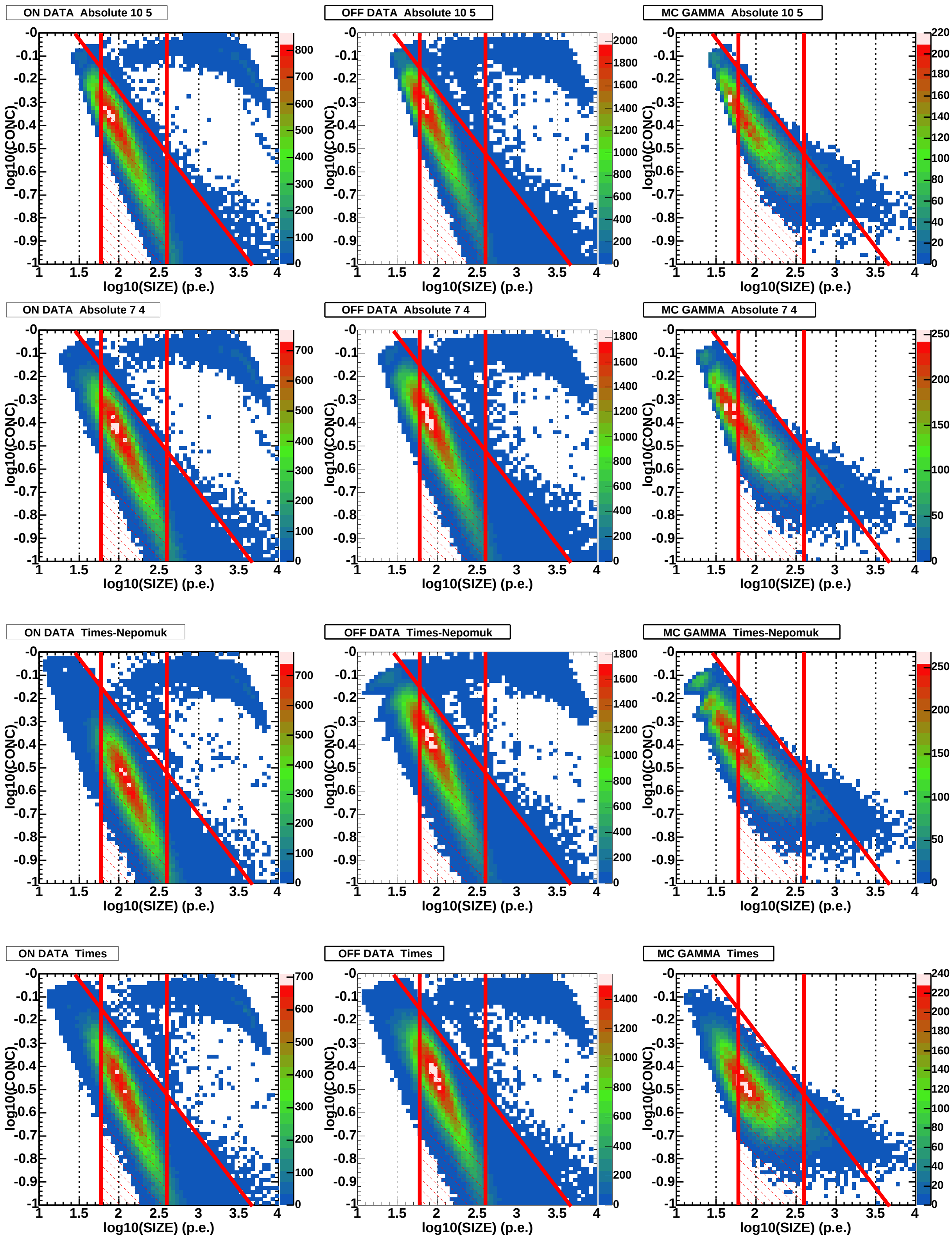

Figure 19: Distributions of the parameter $\log(CONC)$ for the various image cleaning algorithms and the GRB050713a data. The DIST cut from the previous chapter has already been applied. The red lines show the cuts applied previous to the further analysis: $\log(CONC) < (0.65 - (0.45 * \log(SIZE))$. First: absolute cleaning with levels 10 and 5 photo-electrons, second: absolute cleaning with levels 7 and 4 photo-electrons, third: Nepomuk's image cleaning using times, bottom: Markus image cleaning using times.

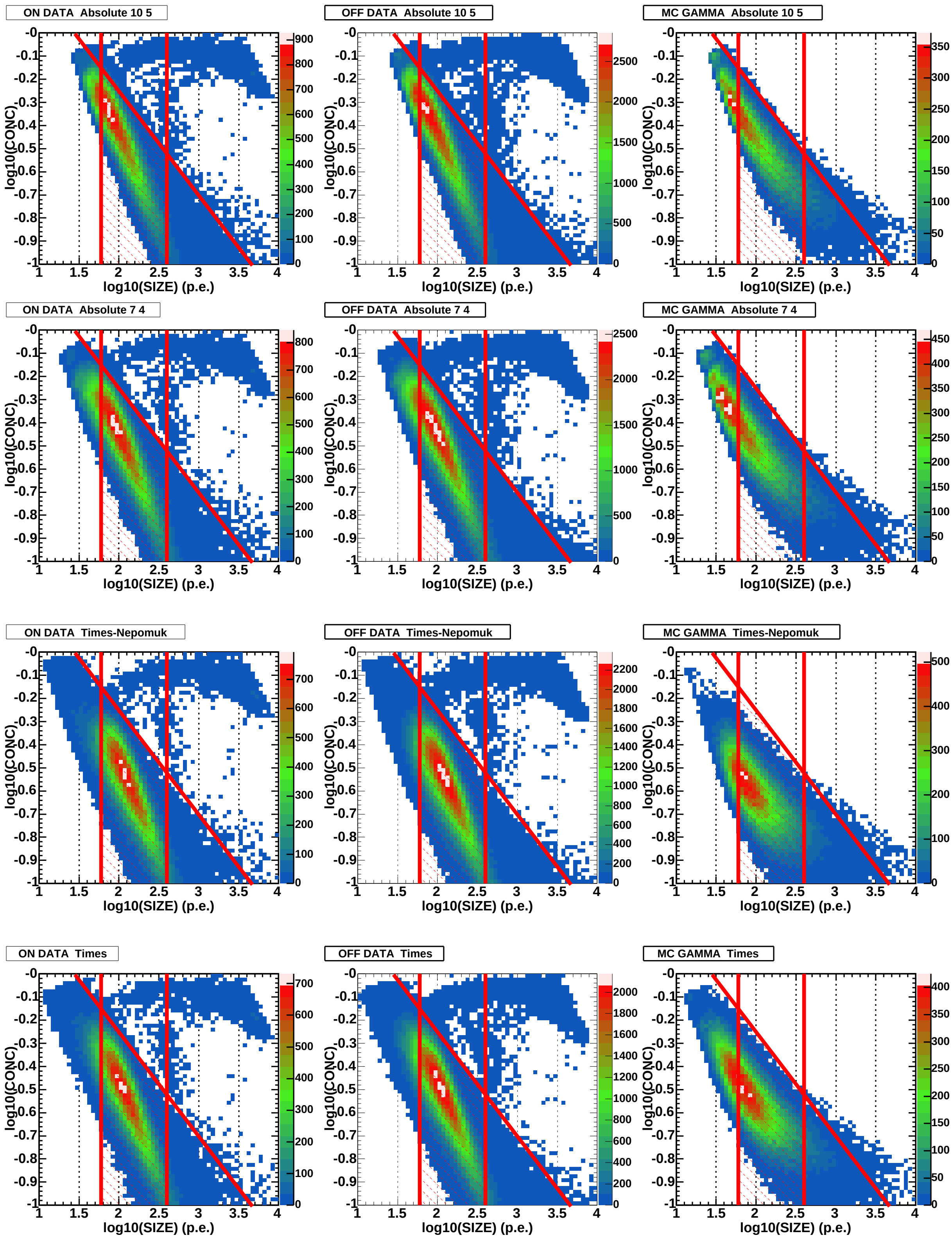

Figure 20: Distribution of the parameter $\log(CONC)$ for the various image cleaning algorithms and the Mrk501 data. The DIST cut from the previous chapter has already been applied. The red lines show the cuts applied previous to the further analysis: $\log(CONC) < (0.65 - (0.45 * \log(SIZE))$. Top: absolute cleaning with levels 10 and 5 photo-electrons, second: absolute cleaning with levels 7 and 4 photo-electrons, third: Nepomuk's image cleaning using times, bottom: Markus image cleaning using times.

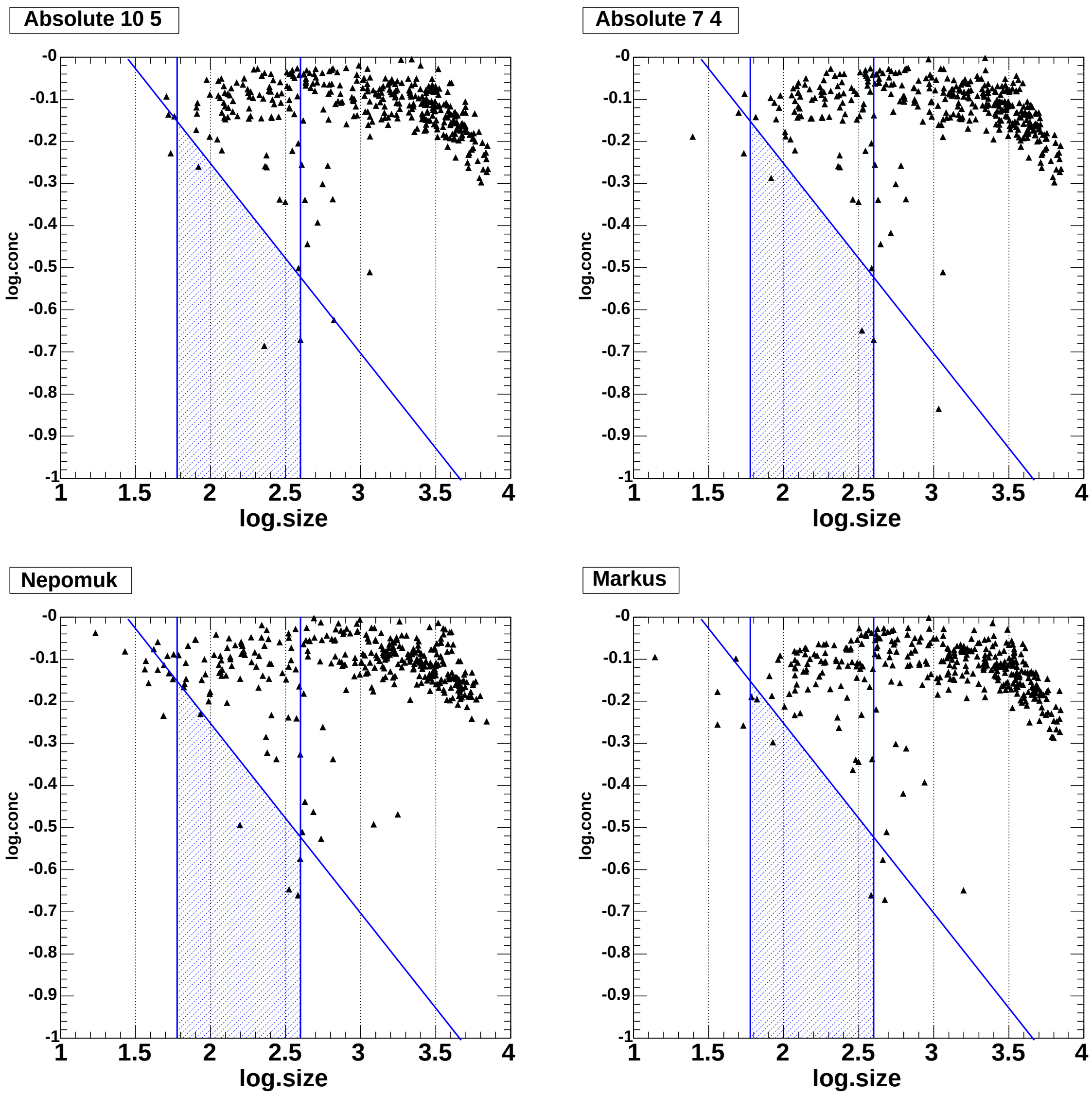

Figure 21: Distribution of the parameter $\log(CONC)$ for the dedicated spark event runs. The blue lines show the cuts applied for the GRB050713a and Mrk501 data samples: $\log(CONC) < (0.65 - (0.45 * \log(SIZE))$. Top left: absolute cleaning with levels 10 and 5 photo-electrons, top right: absolute cleaning with levels 7 and 4 photo-electrons, bottom left: Nepomuk's image cleaning using times, bottom right: Markus image cleaning using times. With this cuts almost all spark events are removed form the data.

7.4 Further Cuts

The following couple of cuts are either standard cuts or do not remove any (simulated) signal such that we simply state them in the following list. As we are interested only in low-energy events, we already set a cut on the $LEAKAGE$ parameter and further proven standard quality cuts:

$$LEAKAGE < 0.01 \quad (4)$$
$$CORE\_PIXELS > 1 \quad (5)$$
$$ISLANDS < 4 \quad (6)$$

7.5 Cut Efficiencies

Tables 4 and 5 list the selection efficiencies for all cleaning steps applied until now. In general, Nepomuk's image cleaning algorithm yields the best efficiency for the Monte-Carlo simulated gamma samples, followed by Markus' algorithm and the absolute cleaning with levels 7 and 4. More than about half the triggered gamma events do not enter the further analysis, mainly because of the cuts in $SIZE$.

The hadron samples ($OFF\ Data$ and $ON\ Data$) yield slightly higher efficiencies, also due to the cuts in $SIZE$. Important is the matching of efficiencies between OFF and ON data, which is the case for the absolute cleaning with levels 7 and 4 and Markus' algorithm, a bit less for Nepomuk's algorithm and worst for the absolute cleaning with levels 10 and 5. Curiously, the matching is better for the GRB05013a data samples than for the Mrk501 data sets.

In the last row of table 4, the cut efficiency for the spark runs is shown: The last cut on $\log(conc)$ effectively removes all sparking events. For the absolute cleaning algorithms, only one event remains, in Markus' algorithm two events and in Nepomuk's one five spark events. From these numbers, we consider the cut in $\log(conc)$ efficient enough to remove the sparking events.

	Selection Efficiencies GRB050713a				
Image Cleaning Algorithm	MC gammas PSF=0.05°	MC gammas PSF=0.07°	OFF Data	ON Data	Sparks Data
Total events	61042	53571	571414	258250	564
	Event surviving Image Cleaning				
Abs_10_5	0.59	0.50	0.81	0.86	0.97
Abs_7_4	0.87	0.79	0.93	0.93	0.98
Nepomuk	0.98	0.97	0.95	0.97	0.91
Markus	0.91	0.90	0.91	0.91	0.99
	Event surviving after SIZE cut				
Abs_10_5	0.39	0.34	0.56	0.61	0.15
Abs_7_4	0.49	0.46	0.63	0.64	0.13
Nepomuk	0.50	0.51	0.63	0.66	0.15
Markus	0.58	0.58	0.63	0.63	0.15
	Event surviving after all pre-cuts				
Abs_10_5	0.37	0.32	0.50	0.56	0.002
Abs_7_4	0.47	0.44	0.57	0.58	0.002
Nepomuk	0.47	0.48	0.55	0.59	0.009
Markus	0.54	0.55	0.52	0.53	0.004

Table 4: Selection efficiencies for the GRB050713a data samples

	Selection Efficiencies Mrk501					
Image Cleaning Algorithm	MC gammas	OFF Data 29/06	OFF Data 02/07	OFF Data 08/07	ON Data DT=32	ON Data DT=40
Total events	122850	272040	344819	218245	263812	451979
	Event surviving Image Cleaning					
Abs_10_5	0.52	0.78	0.85	0.83	0.84	0.93
Abs_7_4	0.81	0.90	0.97	0.96	0.95	0.98
Nepomuk	0.98	0.93	0.99	0.99	0.97	0.99
Markus	0.90	0.89	0.96	0.96	0.93	0.97
	Event surviving size-cut					
Abs_10_5	0.34	0.55	0.60	0.57	0.59	0.68
Abs_7_4	0.44	0.61	0.67	0.65	0.65	0.70
Nepomuk	0.48	0.66	0.71	0.71	0.69	0.68
Markus	0.56	0.62	0.67	0.67	0.65	0.67
	Event surviving pre-cuts					
Abs_10_5	0.26	0.38	0.41	0.40	0.41	0.48
Abs_7_4	0.34	0.42	0.45	0.44	0.44	0.49
Nepomuk	0.37	0.44	0.47	0.47	0.46	0.46
Markus	0.42	0.38	0.41	0.40	0.40	0.42
	Event surviving final cuts					
Abs_10_5	0.20	0.20	0.22	0.00	0.22	0.25
Abs_7_4	0.26	0.18	0.19	0.19	0.19	0.21
Nepomuk	0.36	0.16	0.17	0.18	0.18	0.18
Markus	0.27	0.13	0.14	0.14	0.13	0.14
	Event surviving final cuts and alpha<15					
Abs_10_5	0.15	0.03	0.04	0.00	0.04	0.05
Abs_7_4	0.19	0.03	0.03	0.03	0.03	0.04
Nepomuk	0.23	0.03	0.03	0.03	0.03	0.03
Markus	0.20	0.02	0.02	0.02	0.02	0.03

Table 5: Selection efficiencies for the Mrk501 data samples

7.6 SIZE after pre-cuts

Figure 22 shows the distributions of log($SIZE$) for the GRB050713a data sample after all pre-cuts. One can see that the ON data sample distribution remains shifted with respect to the distribution obtained from the OFF data sample. Looking at the distributions obtained from simulated gamma showers with the point-spread function (PSF) of 0.05° FWHM (histogram "MC") and the other one with the slightly worse PSF of 0.07° FWHM (histogram "MC (PSF)"), one observes a loss of events at low sizes for the simulation using the worse PSF, but no general shift towards higher sizes. These two distributions agree well above about 100 photo-electrons, in the case of Nepomuk's image cleaning, they agree even well below 100 photo-electrons. From these observations, it seems rather unlikely that the difference in PSF is a reason for the disagreement between the ON and the OFF data sample. We tend to attribute it entirely to the difference in discriminator thresholds. Note also the big difference in the shift between Nepomuk's and Markus's image cleaning algorithm. This discrepancy is still not understood and requires further investigation.

In figure 22, one can see even more the lower gamma efficiency for the absolute image cleaning using thresholds of 10 and 5 photo-electrons. Again, the efficiency is highest for the image cleaning algorithms requiring time coincidences, especially for Markus algorithm.

Figure 23 shows the distributions of log($SIZE$) for the Mrk501 data sample after all pre-cuts. Here again, the ON data sample distributions agree well with the ones obtained from the OFF data sample. Also, the relative efficiencies agree very well between ON and OFF sample. Again here however, this agreement applies only for the ON-data taken before the raise of the discriminator thresholds. If the entire ON sample is taken, a similar picture as in figure 22 is obtained.

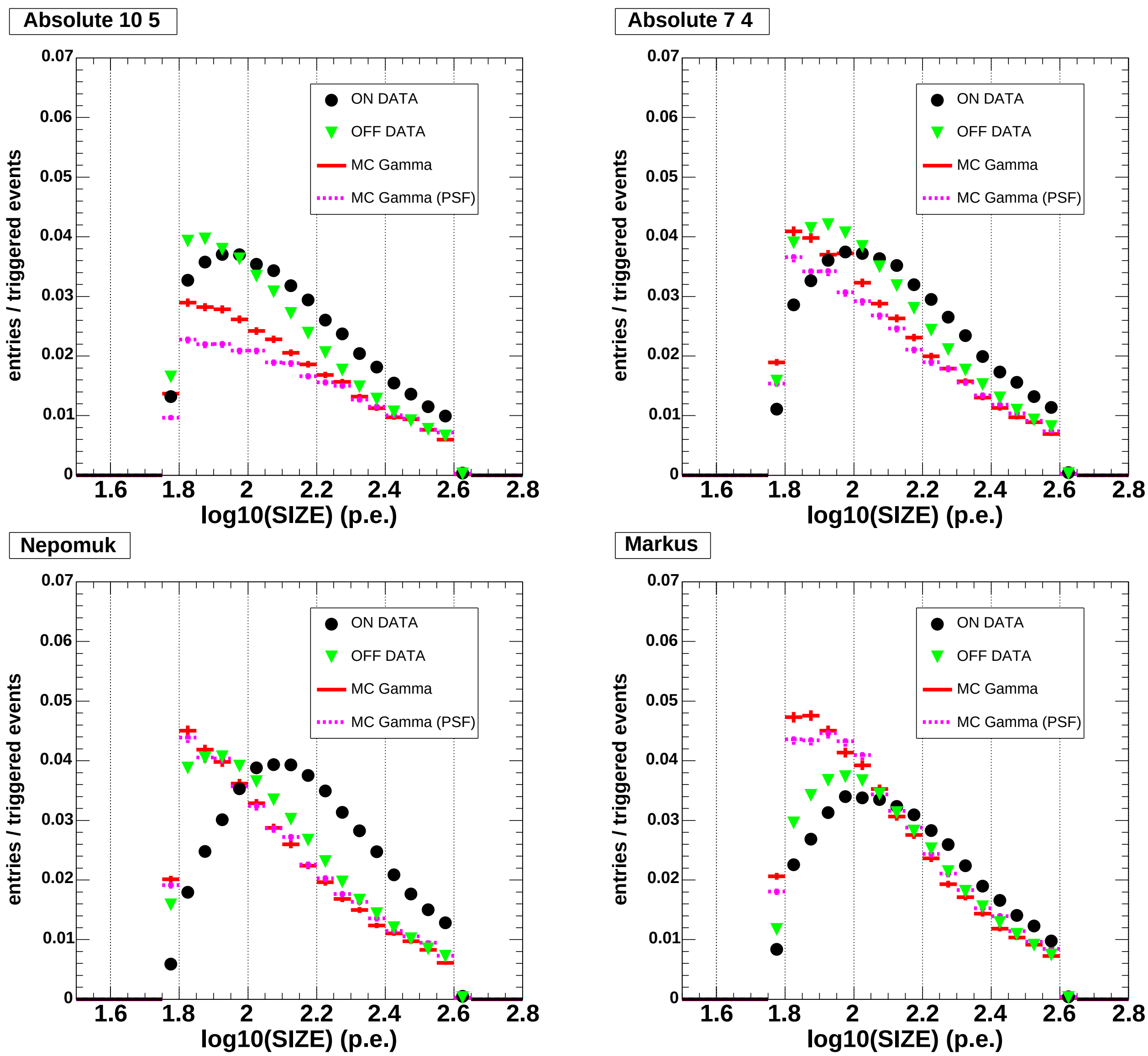

Figure 22: Normalized distributions of the parameter log(size) for the various image cleaning algorithms and the GRB050713a data after pre-cuts. Top left: absolute cleaning with levels 10 and 5 photo-electrons, top right: absolute cleaning with levels 7 and 4 photo-electrons, bottom left: Nepomuk's image cleaning using times, bottom right: Markus image cleaning using times.

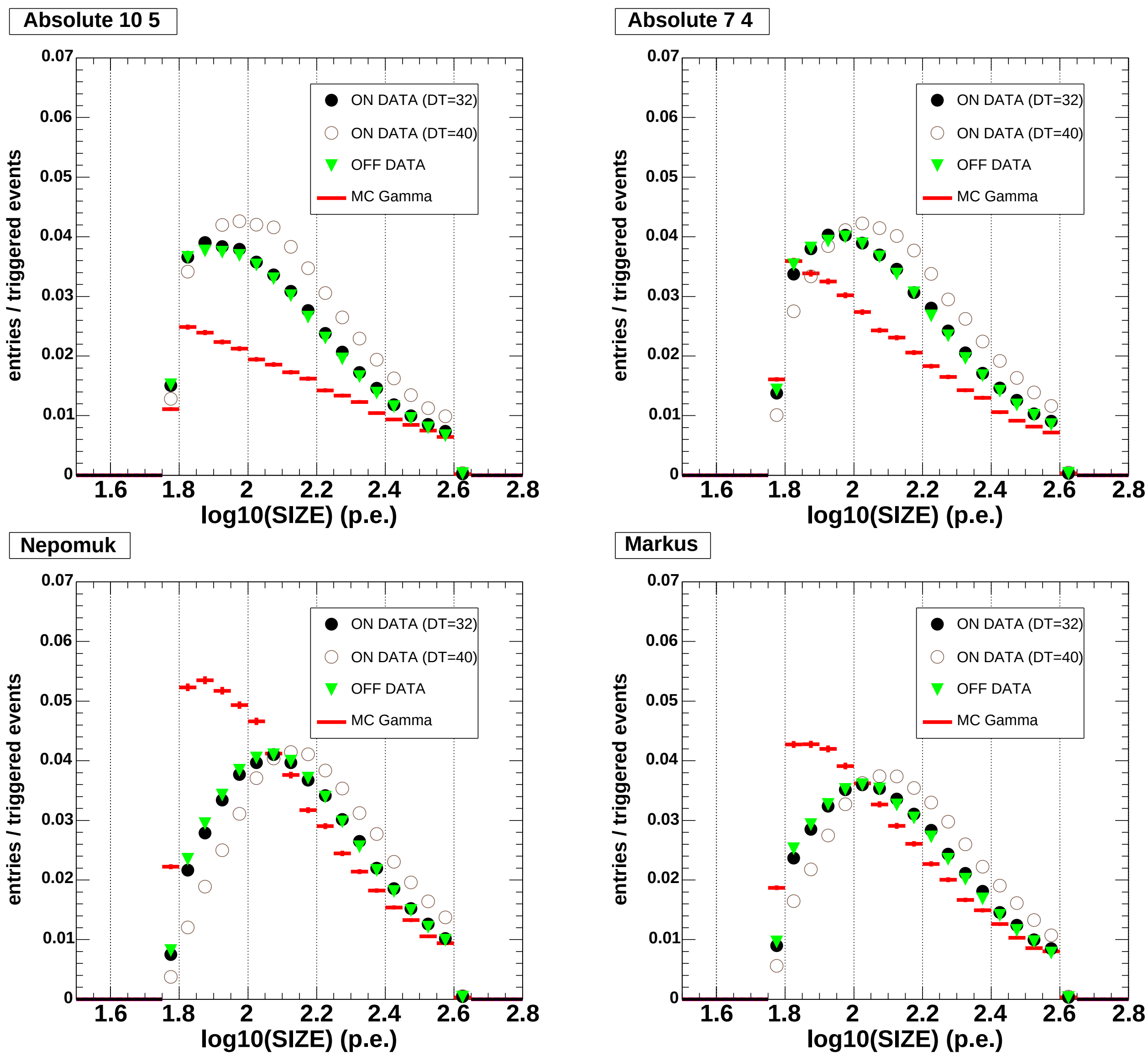

Figure 23: Normalized distribution of the parameter log(size) for the various image cleaning algorithms and the Mrk501 data after pre-cuts. Top left: absolute cleaning with levels 10 and 5 photo-electrons, top right: absolute cleaning with levels 7 and 4 photo-electrons, bottom left: Nepomuk's image cleaning using times, bottom right: Markus image cleaning using times.

7.7 Center of Gravity after pre-cuts

The Center-of-gravity (C.o.G.) is good measure for the homogeneity of the camera response. Figures 24 show the C.o.G. obtained from the GRB050713a data for various data samples: The MC simulated gamma events (left), the ON data (center) and the OFF data (right) for three different image cleaning algorithms (top to bottom).

Generally, a void can be seen at the lower right edge and the right edge of the camera, as already noted in the previous chapters. The absolute image cleaning shows additionally a void at the upper right edge of the camera. At the left side of the camera and at some smaller spots towards the center of the camera, clear excesses are observed with all image cleaning algorithms. The reason for this non-uniformity is still unclear. However, these excesses appear more pronounced if one of the time image cleaning algorithms is used and for the ON data. We found out that the inhomogeneities appear above all at low energies, which explains partly the increased sensitivity of the time image cleanings towards them. Moreover, we note that the inhomogenities do not coincide at all with the trigger cell timing offsets observed in [5].

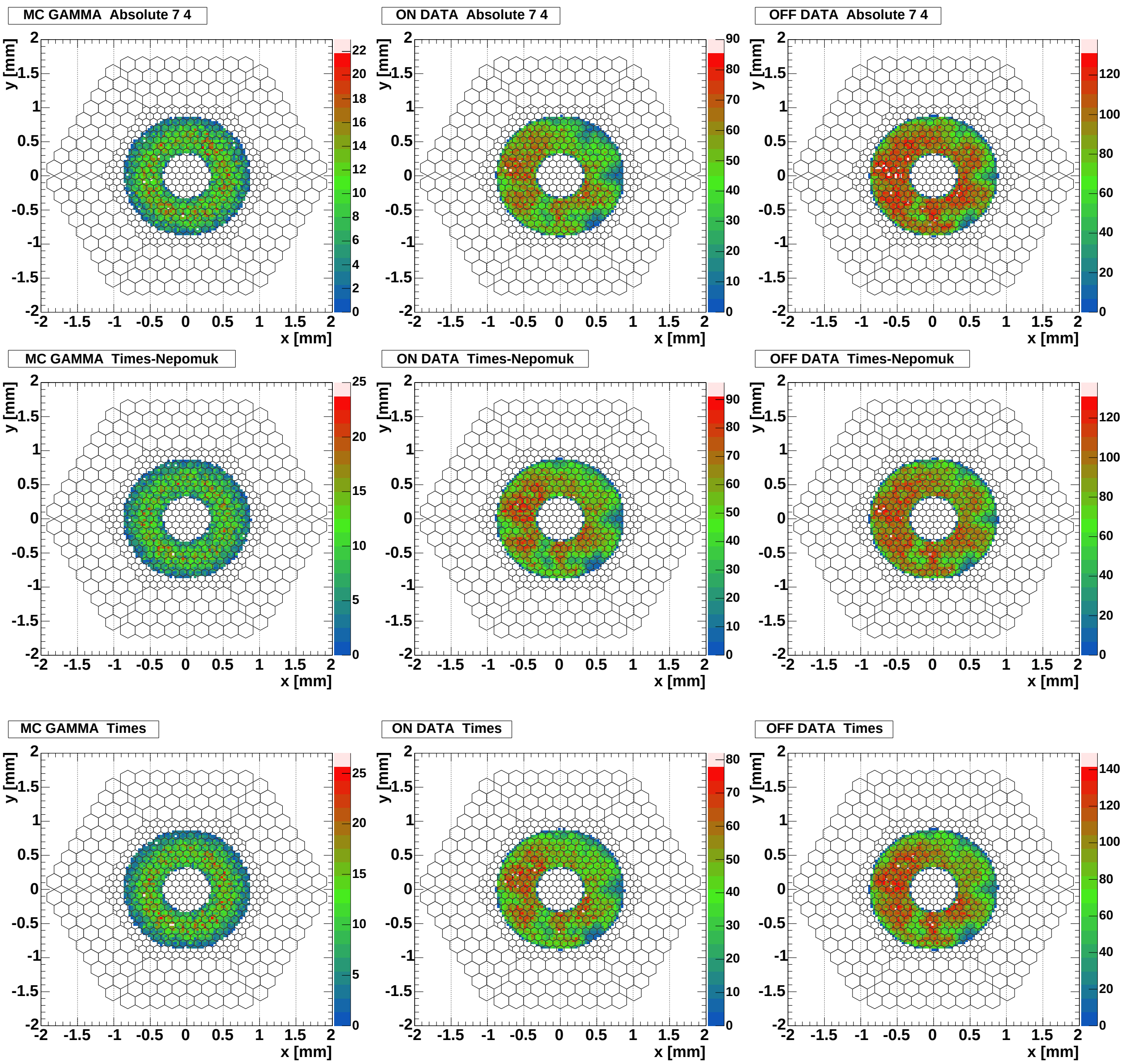

Figure 24: The C.o.G., obtained from the GRB050713a data after pre-cuts. Left: Simulated gamma showers, center: ON data, right: OFF data. Top: Absolute 7 4 image cleaning, center: Nepomuk's algorithm, bottom: Markus' algorithm.

8 Random Forest Analysis

The next step consists in the calculation of the $HADRONNESS$ parameter using the Random Forest algorithm [11]. The algorithm consists in a training procedure and a subsequent application of the trained algorithm onto the data. A similar approach can be used for the estimation of the shower energy. In order to avoid biases, the simulated gamma sample was therefore divided into three samples: One training sample for the $HADRONNESS$ parameter, one training sample for the $ENERGY$ parameter and one test sample for all later analysis.

As we wanted to perform an analysis based on the $ALPHA$ distribution (the "Alpha Analysis") and a second one using the $DISP$-algorithm (the "Disp Analysis"), we had to train and apply the Random Forest matrices twice: Once using source-dependent parameters (for the "Alpha Analysis") and another time excluding source-dependent parameters (for the "Disp Analysis").

The following variables were used for both analyses:

- $SIZE$
- $WIDTH$
- $LENGTH$
- $CONC$
- $CONC4$

For the "Alpha Analysis", additionally the two source-dependent parameters were used:

- $DIST$
- sign(cos($DELTA \cdot ALPHA$))*$M3LONG$

8.1 Mrk501 data

Figures 25 to 30 show the distributions of the used parameters for the four tested image cleaning algorithms. One can see that in general, there are quite remarkable differences between the different cleaning algorithms, however the distributions agree very well between the two ON data samples and the OFF sample, except for some absolute normalization in the case of the absolute image cleanings. An exception to the good agreement can be found in the parameters $CONC$ and $CONC4$ where slight disagreements between the two ON samples are found. However, ON and OFF data taken with the same discriminator threshold settings agree well. For this reason, we found that the OFF data (which was used for the Random Forest training) was sufficiently well described by these two parameters such that the resulting Random Forest matrices could be later applied to at least the first part of the ON data.

Figure 31 shows the mean decrease in Gini index, obtained from the different optimizations. That variable is a measure of the efficiency that the given cut parameter obtains in rejecting background if the other cut parameters are present. One can see that the parameter $LENGTH$ results to be the strongest cut parameter for the absolute image cleaning. If time image cleanings are used, the parameter $CONC4$ results to be the most efficient. From figure 31, one can also deduce that the differences in $HADRONNESS$ between the "Alpha Analysis" and the "Disp Analysis" will be rather small since the importance of the two parameters $DIST$ and $M3LONG$ is very small.

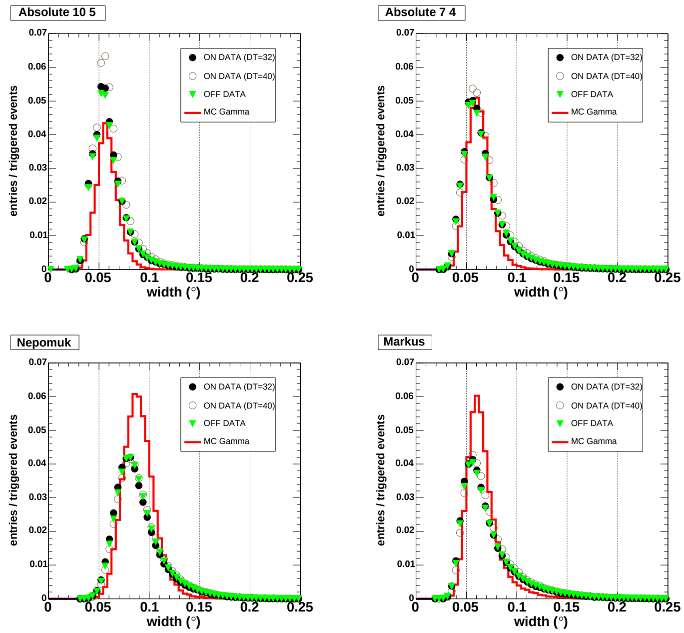

Figure 25: Normalized distributions of the parameter $WIDTH$ for the various image cleaning algorithms and the Mrk501 data. Top left: absolute cleaning with levels 10 and 5 photo-electrons, top right: absolute cleaning with levels 7 and 4 photo-electrons, bottom left: Nepomuk's image cleaning using time coincidence, bottom right: Markus's image cleaning using time coincidence.

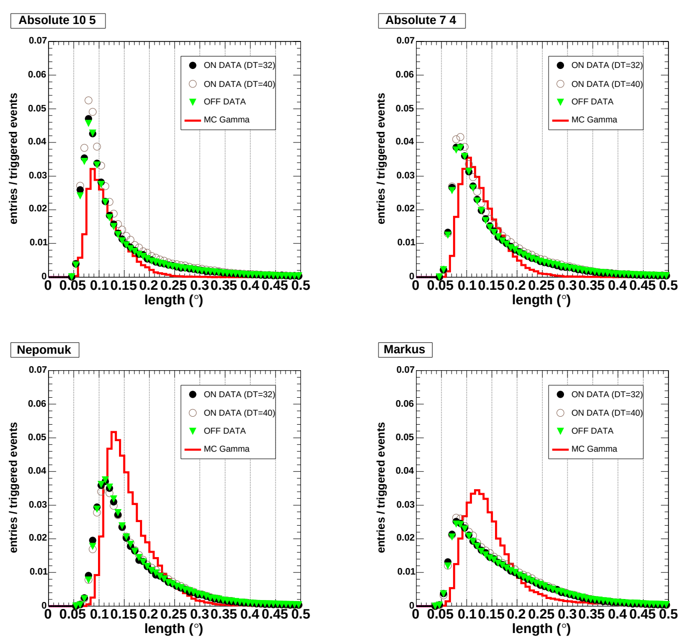

Figure 26: Normalized distributions of the parameter $LENGTH$ for the various image cleaning algorithms and the Mrk501 data. Top left: absolute cleaning with levels 10 and 5 photo-electrons, top right: absolute cleaning with levels 7 and 4 photo-electrons, bottom left: Nepomuk's image cleaning using time coincidence, bottom right: Markus's image cleaning using time coincidence.

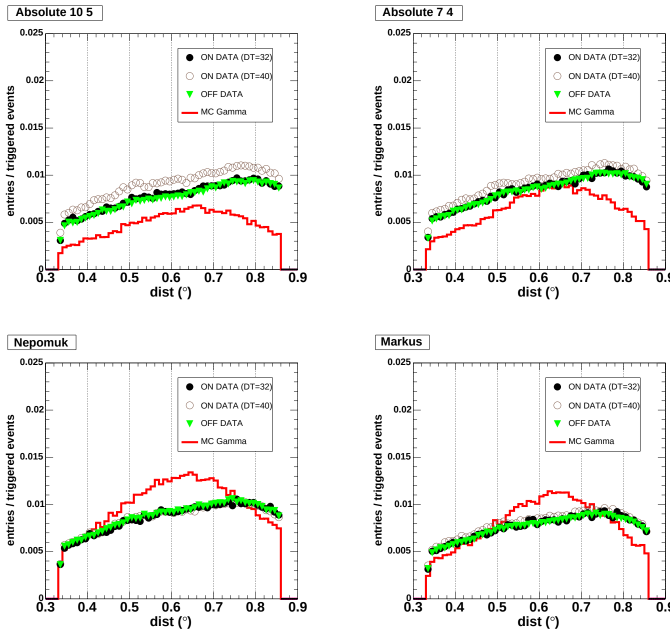

Figure 27: Normalized distributions of the parameter $DIST$ for the various image cleaning algorithms and the Mrk501 data. Top left: absolute cleaning with levels 10 and 5 photo-electrons, top right: absolute cleaning with levels 7 and 4 photo-electrons, bottom left: Nepomuk's image cleaning using time coincidence, bottom right: Markus's image cleaning using time coincidence.

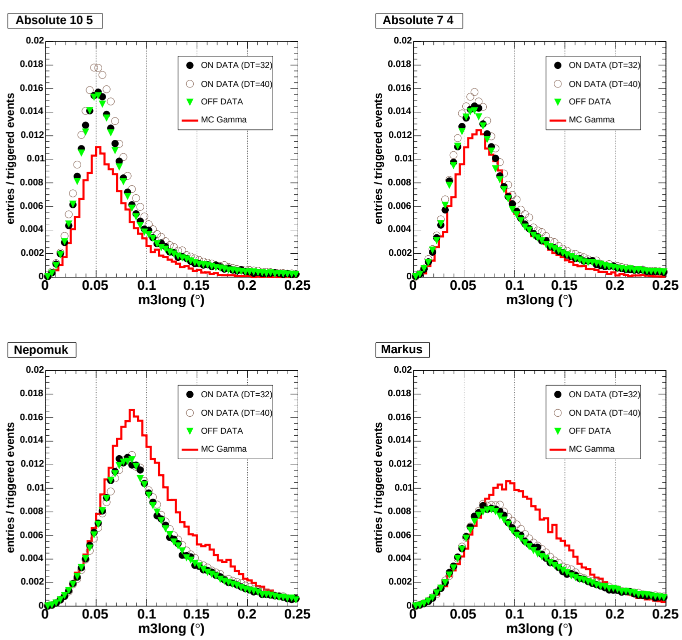

Figure 28: Normalized distributions of the parameter $M3LONG$ for the various image cleaning algorithms and the Mrk501 data. Top left: absolute cleaning with levels 10 and 5 photo-electrons, top right: absolute cleaning with levels 7 and 4 photo-electrons, bottom left: Nepomuk's image cleaning using time coincidence, bottom right: Markus's image cleaning using time coincidence.

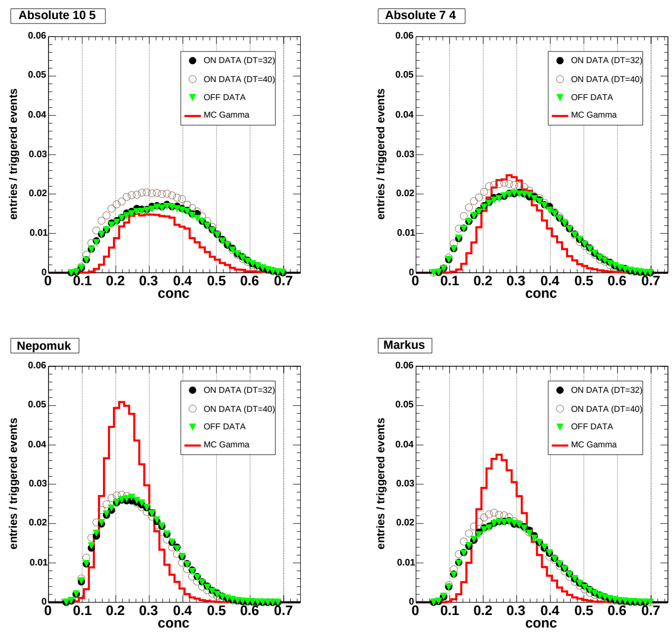

Figure 29: Normalized distributions of the parameter $CONC$ for the various image cleaning algorithms and the Mrk501 data. Top left: absolute cleaning with levels 10 and 5 photo-electrons, top right: absolute cleaning with levels 7 and 4 photo-electrons, bottom left: Nepomuk's image cleaning using time coincidence, bottom right: Markus's image cleaning using time coincidence.

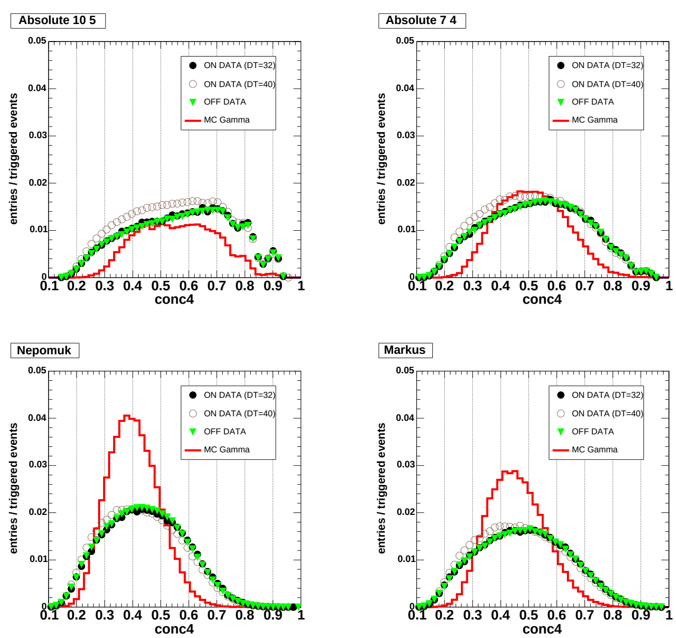

Figure 30: Normalized distributions of the parameter $CONC4$ for the various image cleaning algorithms and the Mrk501 data. Top left: absolute cleaning with levels 10 and 5 photo-electrons, top right: absolute cleaning with levels 7 and 4 photo-electrons, bottom left: Nepomuk's image cleaning using time coincidence, bottom right: Markus's image cleaning using time coincidence.

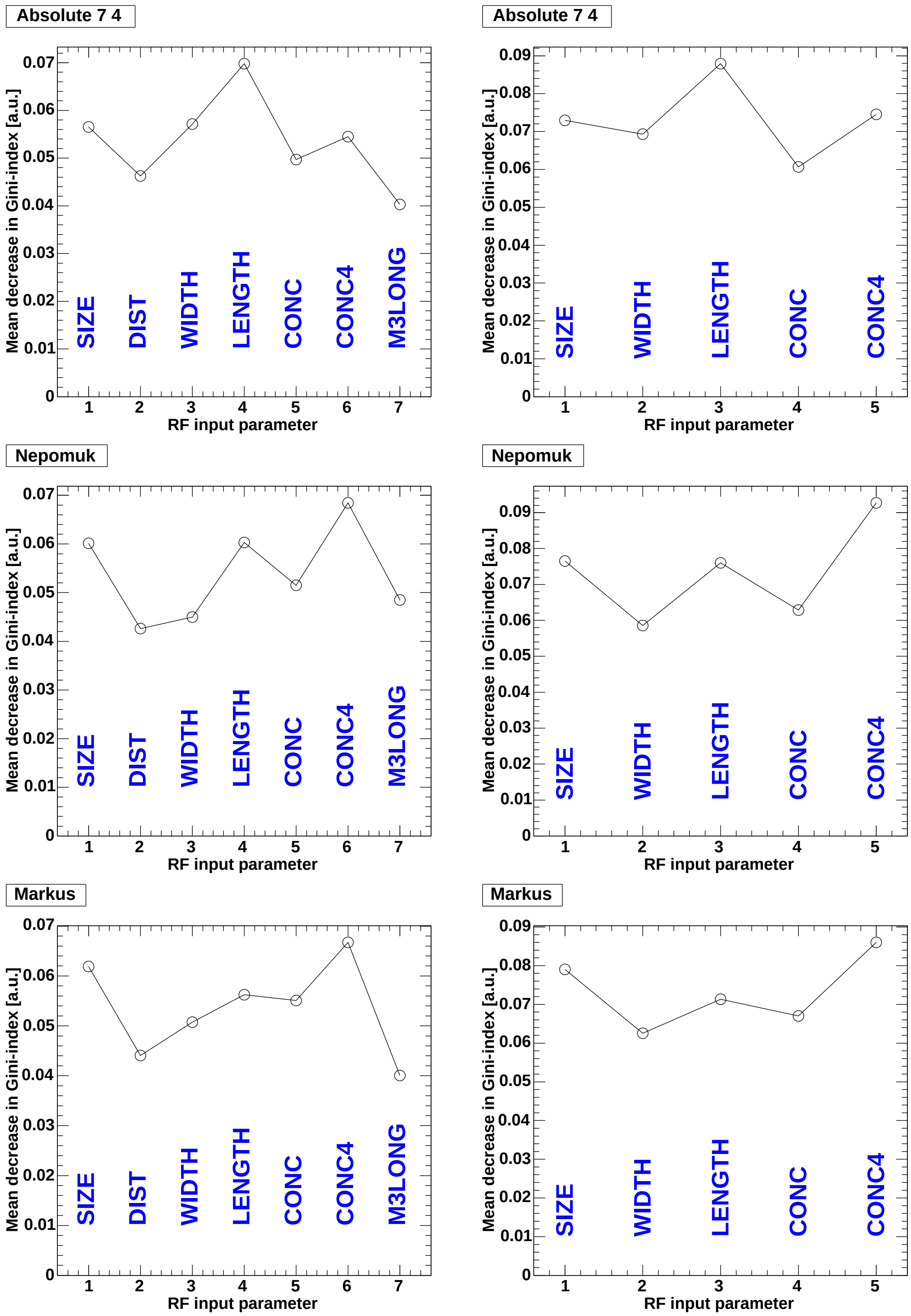

Figure 31: Mean decrease in Gini index for every parameter used by the Random Forest training of the Mrk501 data. On the left side, the parameters used for the "Alpha Analysis" are shown, on the right side, only those used for the "Disp Analysis". The values are proportional to the relative importance of the parameter in the rejection of the background. The different image cleaning algorithms correspond to: Top: absolute cleaning with levels 7 and 4 photo-electrons, center: Nepomuk's image cleaning using time coincidence, bottom: Markus's image cleaning using time coincidence.

8.2 GRB050713 data

Figures 32 to 37 show the distributions of the used parameters for the four tested image cleaning algorithms, displaying ON and OFF data and the simulated gammas with two point spread functions. Apart from the conclusions drawn from the Mrk501 data, one can see that three parameters show a sizeable dependency on the point spread function:

- $WIDTH$
- $CONC$
- $CONC4$

The $CONC$ and $CONC4$ parameter show moreover a dependency on the discriminator threshold.

For this reason, the Random Forest training was not performed taking the OFF data as background, but instead the last four runs of the ON data! We believe that this decision introduces less biases than taking a very deviating OFF data sample. Our approach was justified later when it became clear that no signal was detected in the last four runs. Because the efficiency of background rejection lies far away from 100%, a possible small signal there, possibly overlooked due to the bias introduced by this procedure would not have been able to bias the Random Forest training considerably. Due to the lack of such a bias, in contrary, an overlooked signal cannot be large. We did not have time to quantify this reasoning, maybe the Random Forest experts can help to do so...

Figure 38 shows the mean decrease in Gini index, obtained from the different optimizations using the better point spread function ($PSF = 0.05°\sigma$), while the same variables shown in figure 39 were obtained using the worse point spread function ($PSF = 0.07°\sigma$). That variable is a measure of the efficiency that the given cut parameter obtains in rejecting background if the other cut parameters are present. One can see that the parameter $LENGTH$ results to be the strongest cut parameter for the absolute image cleaning. If time image cleanings are used, the parameter $CONC4$ results to be the most efficient. Comparing the efficiency of the $WIDTH$ parameter against the one of the $LENGTH$ parameter between the two simulations using different point spread functions, one can see that the order gets inversed: If the worse PSF is used, the importance of the $WIDTH$ parameter increases.

As already concluded from the Mrk501 analysis, the importance of the parameters $DIST$ and $M3LONG$ is very low. We therefore conclude that the differences in $HADRONNESS$ between the "Alpha Analysis" and the "Disp Analysis" will be rather small.

The precision of the reconstructed energy can be estimated from figure 40 for both values of the point spread function and two bins of reconstructed energy. One can see that the degradation of the energy resolution due to the use of the worse PSF is negligible. We obtain a global energy resolution of about 34% for the bin ranging from 100 GeV to 200 GeV and about 28% from 200 GeV to 500 GeV, respectively using Nepomuk's image cleaning.

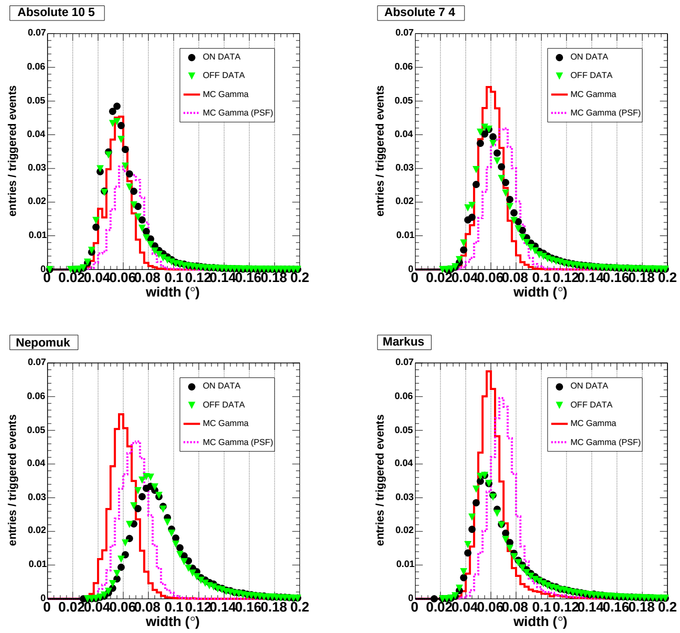

Figure 32: Normalized distributions of the parameter $WIDTH$ for the various image cleaning algorithms and the GRB050713a data. Top left: absolute cleaning with levels 10 and 5 photo-electrons, top right: absolute cleaning with levels 7 and 4 photo-electrons, bottom left: Nepomuk's image cleaning using time coincidence, bottom right: Markus's image cleaning using time coincidence.

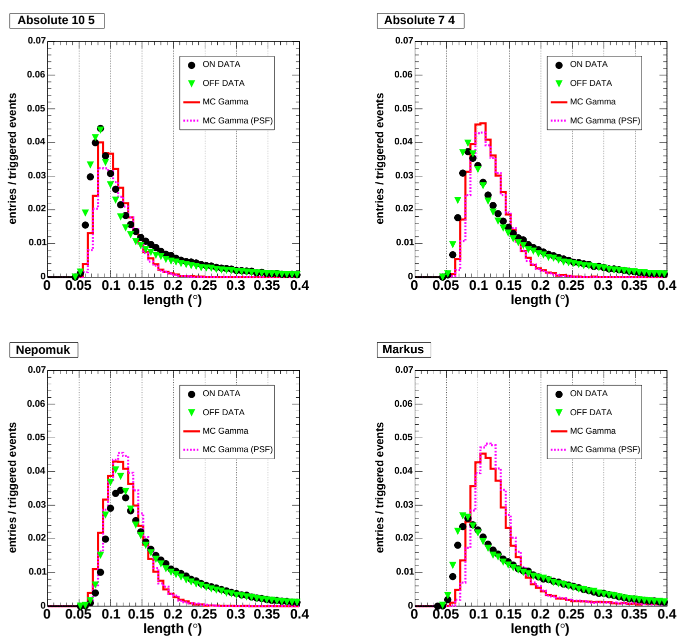

Figure 33: Normalized distributions of the parameter $LENGTH$ for the various image cleaning algorithms and the GRB050713a data. Top left: absolute cleaning with levels 10 and 5 photo-electrons, top right: absolute cleaning with levels 7 and 4 photo-electrons, bottom left: Nepomuk's image cleaning using time coincidence, bottom right: Markus's image cleaning using time coincidence.

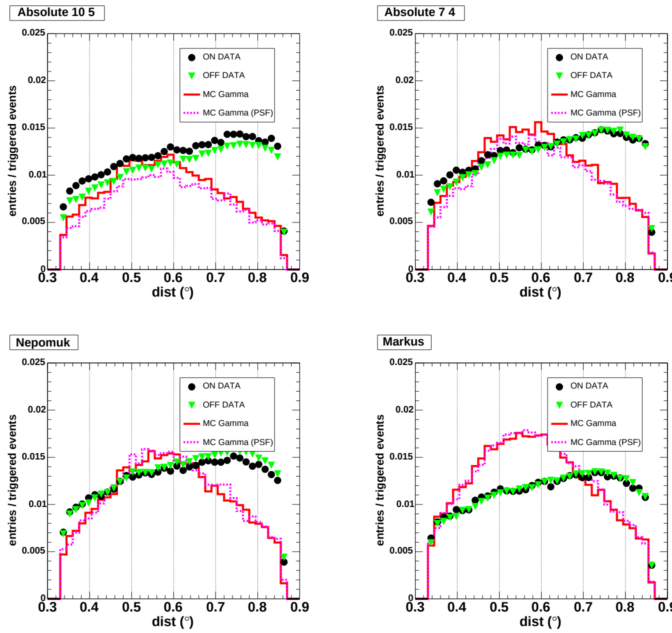

Figure 34: Normalized distributions of the parameter $DIST$ for the various image cleaning algorithms and the GRB050713a data. Top left: absolute cleaning with levels 10 and 5 photo-electrons, top right: absolute cleaning with levels 7 and 4 photo-electrons, bottom left: Nepomuk's image cleaning using time coincidence, bottom right: Markus's image cleaning using time coincidence.

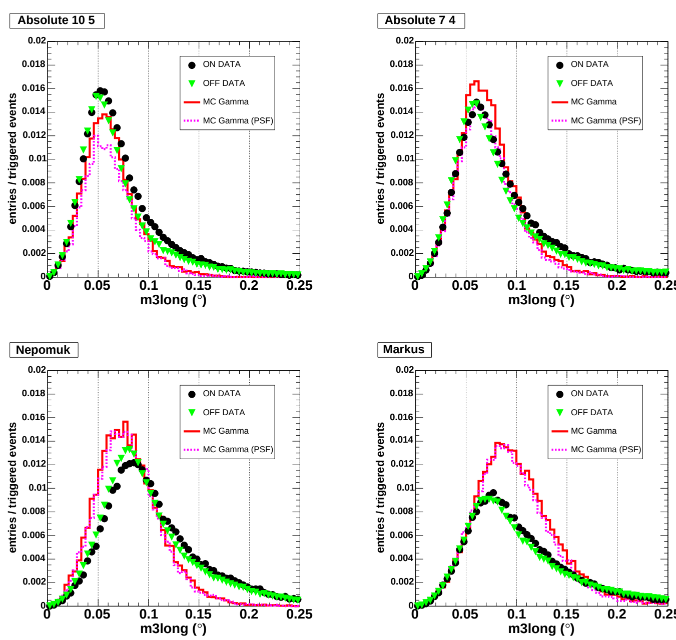

Figure 35: Normalized distributions of the parameter $M3LONG$ for the various image cleaning algorithms and the GRB050713a data. Top left: absolute cleaning with levels 10 and 5 photo-electrons, top right: absolute cleaning with levels 7 and 4 photo-electrons, bottom left: Nepomuk's image cleaning using time coincidence, bottom right: Markus's image cleaning using time coincidence.

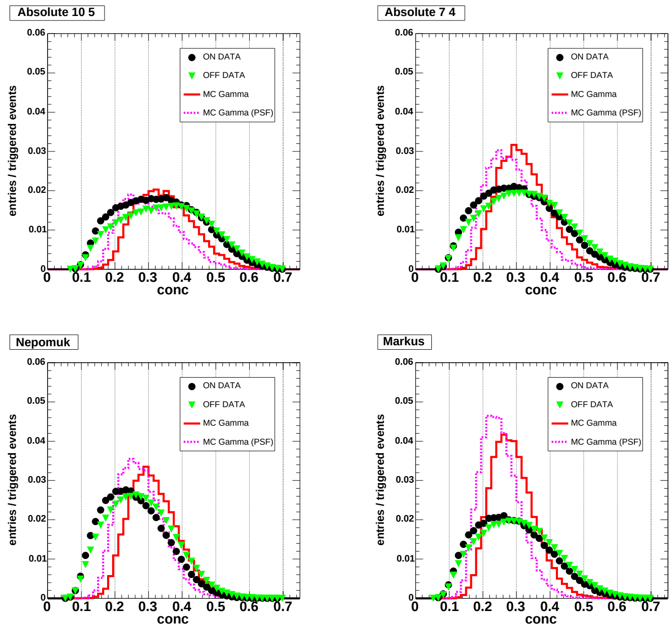

Figure 36: Normalized distributions of the parameter $CONC$ for the various image cleaning algorithms and the GRB050713a data. Top left: absolute cleaning with levels 10 and 5 photo-electrons, top right: absolute cleaning with levels 7 and 4 photo-electrons, bottom left: Nepomuk's image cleaning using time coincidence, bottom right: Markus's image cleaning using time coincidence.

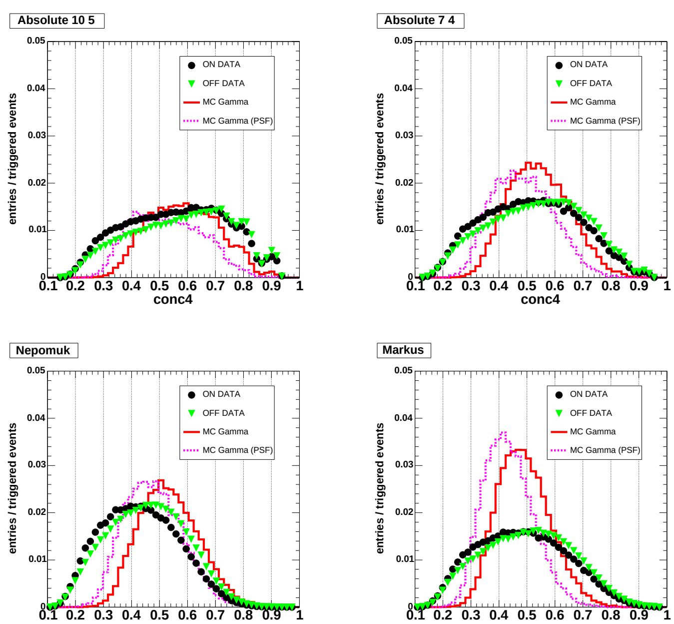

Figure 37: Normalized distributions of the parameter $CONC4$ for the various image cleaning algorithms and the GRB050713a data. Top left: absolute cleaning with levels 10 and 5 photo-electrons, top right: absolute cleaning with levels 7 and 4 photo-electrons, bottom left: Nepomuk's image cleaning using time coincidence, bottom right: Markus's image cleaning using time coincidence.

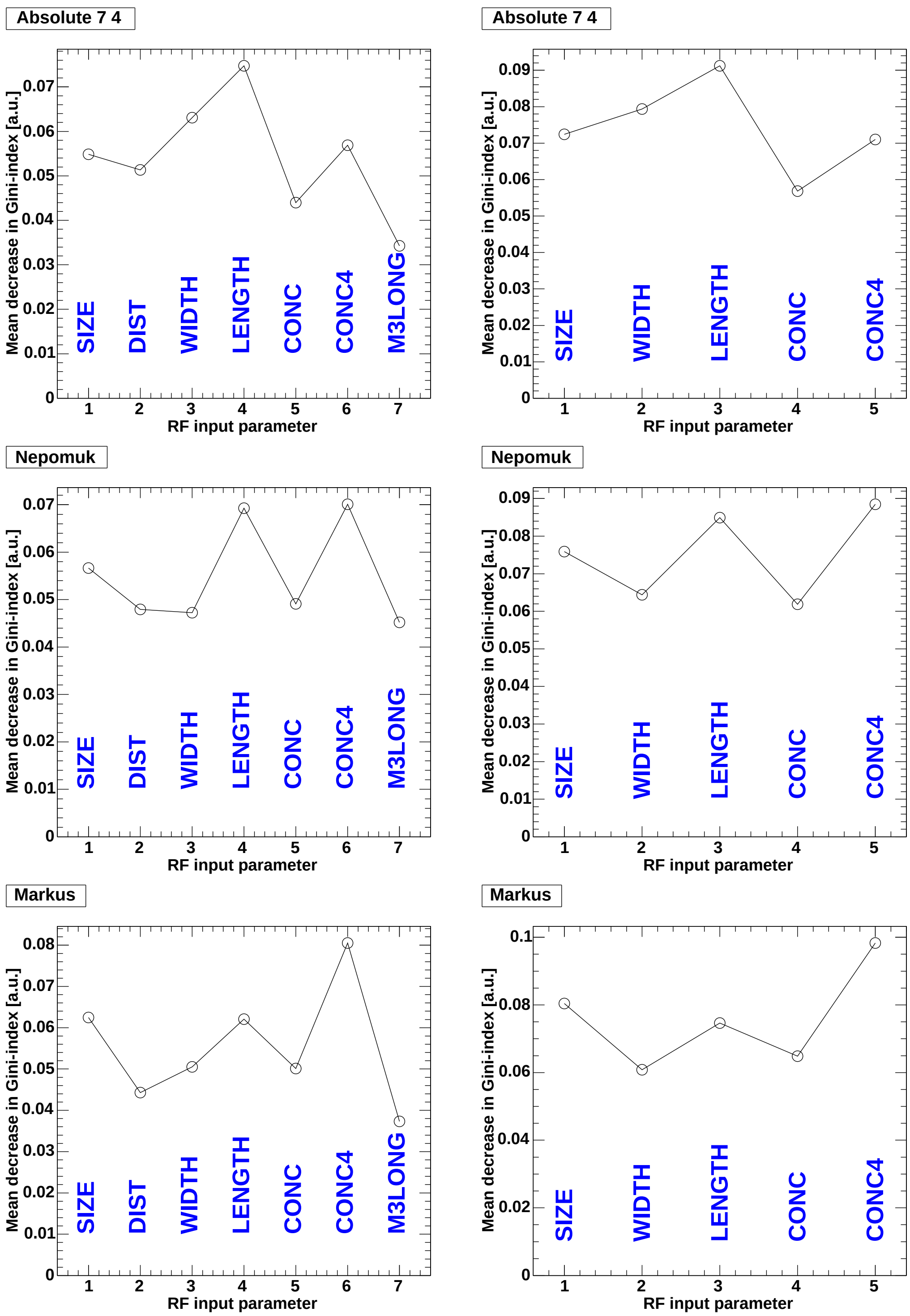

Figure 38: Mean decrease in Gini index for every parameter used by the Random Forest training of the GRB050713a data, using a PSF of $0.05°\sigma$. On the left side, the parameters used for the "Alpha Analysis" are shown, on the right side, only those used for the "Disp Analysis". The values are proportional to the relative importance of the parameter in the rejection of the background. The different image cleaning algorithms correspond to: Top: absolute cleaning with levels 7 and 4 photo-electrons, center: Nepomuk's image cleaning using time coincidence, bottom: Markus's image cleaning using time coincidence.

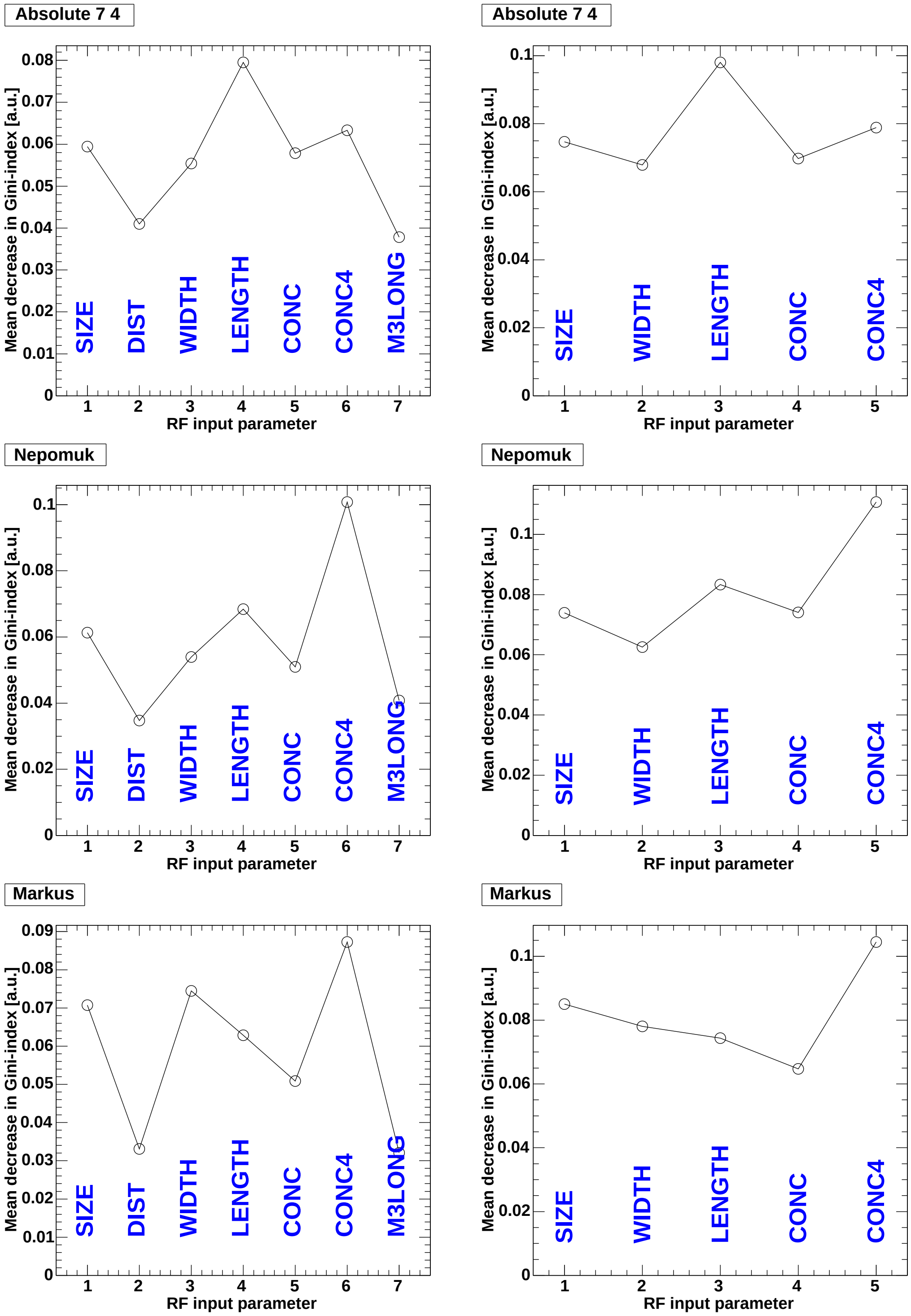

Figure 39: Mean decrease in Gini index for every parameter used by the Random Forest training of the GRB050713a data, using a PSF of $0.07°\sigma$. On the left side, the parameters used for the "Alpha Analysis" are shown, on the right side, only those used for the "Disp Analysis". The values are proportional to the relative importance of the parameter in the rejection of the background. The different image cleaning algorithms correspond to: Top: absolute cleaning with levels 7 and 4 photo-electrons, center: Nepomuk's image cleaning using time coincidence, bottom: Markus's image cleaning using time coincidence.

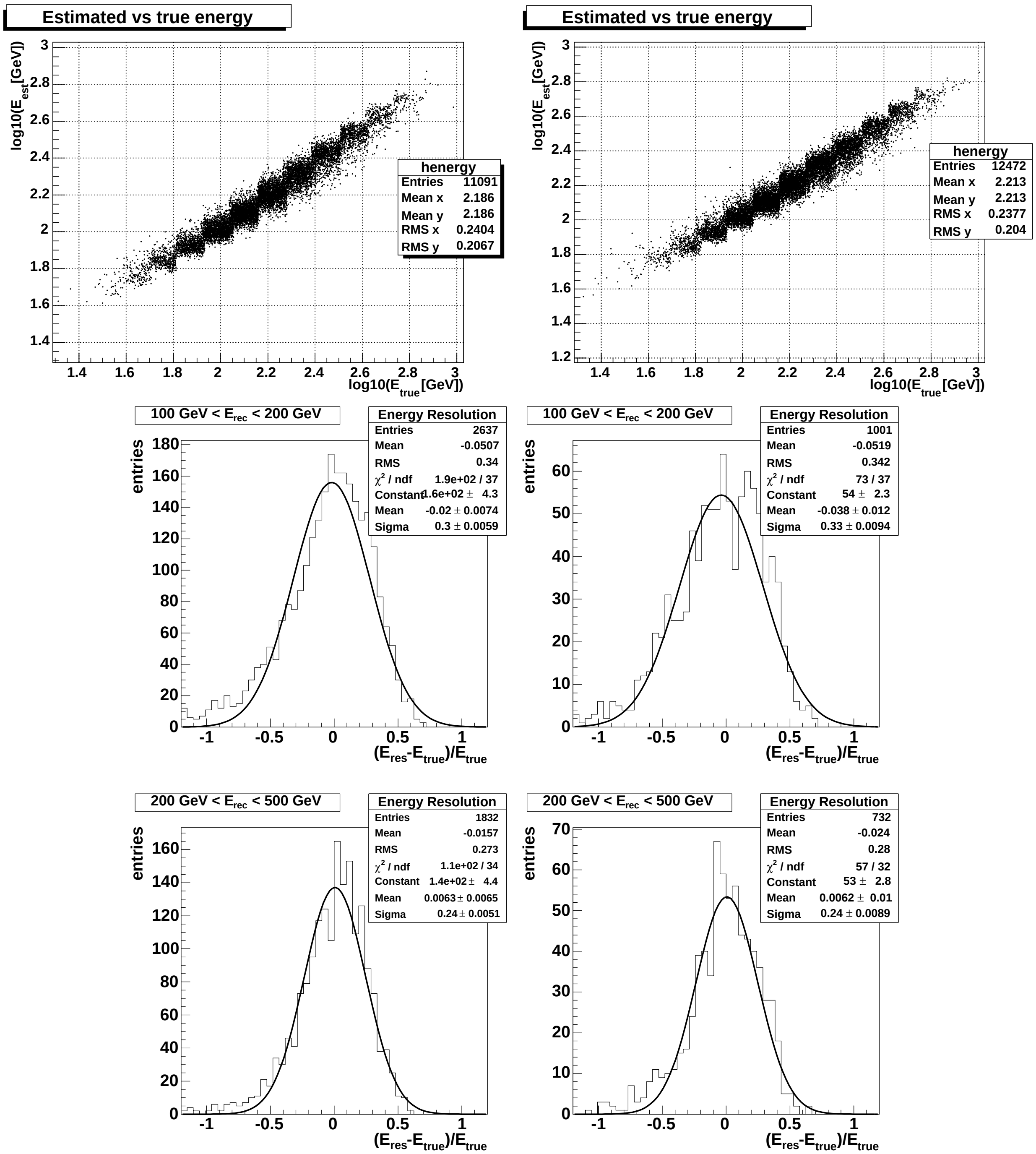

Figure 40: Distributions of the reconstructed energy vs. the true energy of gamma showers, simulated for the GRB050713a data, cleaned with Nepomuk's image cleaning and approximate final cuts applied ($HADRONNESS < 0.6$). On the left side, the parameters obtained with a point spread function of $PSF = 0.05°\sigma$ are shown, on the right side with $PSF = 0.07°\sigma$. Top: Reconstructed energy vs. true energy, center: Energy resolution $\Delta E = \frac{E_{rec}-E_{true}}{E_{true}}$ for the bin $100\,\mathrm{GeV} < E_{rec} < 200\,\mathrm{GeV}$, bottom: Energy resolution $\Delta E = \frac{E_{rec}-E_{true}}{E_{true}}$ for the bin $200\,\mathrm{GeV} < E_{rec} < 500\,\mathrm{GeV}$.

8.3 Tests of the Parameters used for the RF training

In the following, we test how well the parameters used for the RF training are reproduced by the MC. For this reason, we separate a rather clean gamma sample from the Mrk501 data, using the following test cuts:

$$\begin{aligned}
ISLANDS &< 2 \\
LEAKAGE &< 0.005 \\
0.45 &< DIST < 0.78 \\
SIZE &> 90 \\
120 &< ENERGY < 200 \\
HADRONNESS &< 0.08 \quad \text{for absolute cleanings} \\
HADRONNESS &< 0.13 \quad \text{for Nepomuk's cleaning} \\
HADRONNESS &< 0.2 \quad \text{for Markus' cleaning} \\
ALPHA &< 10. \quad \text{for absolute cleanings} \\
ALPHA &< 18. \quad \text{for Nepomuk's cleaning} \\
ALPHA &< 15. \quad \text{for Markus' cleaning}
\end{aligned} \tag{7}$$

These choices provide us with gamma samples at rather low energy, contaminated by less than 15% hadrons. In the following, the variables used for the RF training, were plotted and a Kolmogorov-Smirnov (KS) test applied between the MC simulated gamma distribution and the ON distribution, subtracted with the OFF data distribution. Figures 41 to 46 show the results. Within the limited statistics which provide this sample, all distributions agree well, i.e. the KS probability is larger than 10%, except for the variables $CONC$ and $CONC4$ in combination with the absolute image cleaning using 7 and 4 photo-electrons as thresholds (Prob KS $< 0.1\%$ and $< 1.8\%$ for $CONC$ and $CONC4$, respectively) and Markus algorithm (Prob KS $= 3\%$ for $CONC$ and $<1.7\%$ for $CONC4$). On can also note a clear shift of these distributions w.r.t. the one predicted from the MC simulated gamma showers.

We conclude that some caution has to be used with the results coming from the absolute 7 4 and Markus image cleaning because some of the background rejection may have been affected by a systematic difference between MC and real data. Nepomuk's algorithm seems to be un-affected, at least within the scope of this small test.

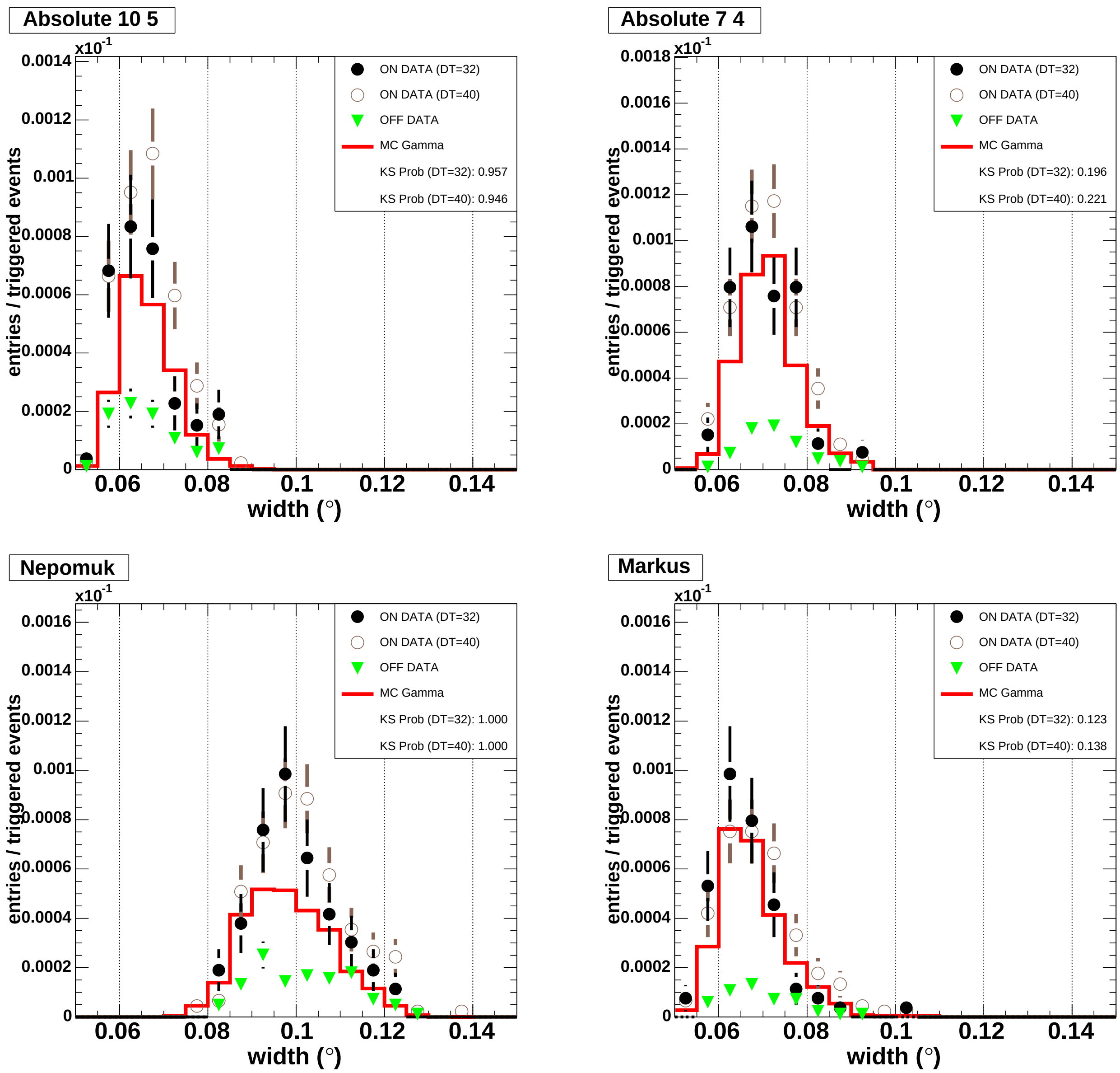

Figure 41: Normalized distributions of the parameter $WIDTH$ for the various image cleaning algorithms and a gamma-enriched Mrk501 data sample.. Top left: absolute cleaning with levels 10 and 5 photo-electrons, top right: absolute cleaning with levels 7 and 4 photo-electrons, bottom left: Nepomuk's image cleaning using time coincidence, bottom right: Markus image cleaning using time coincidence.

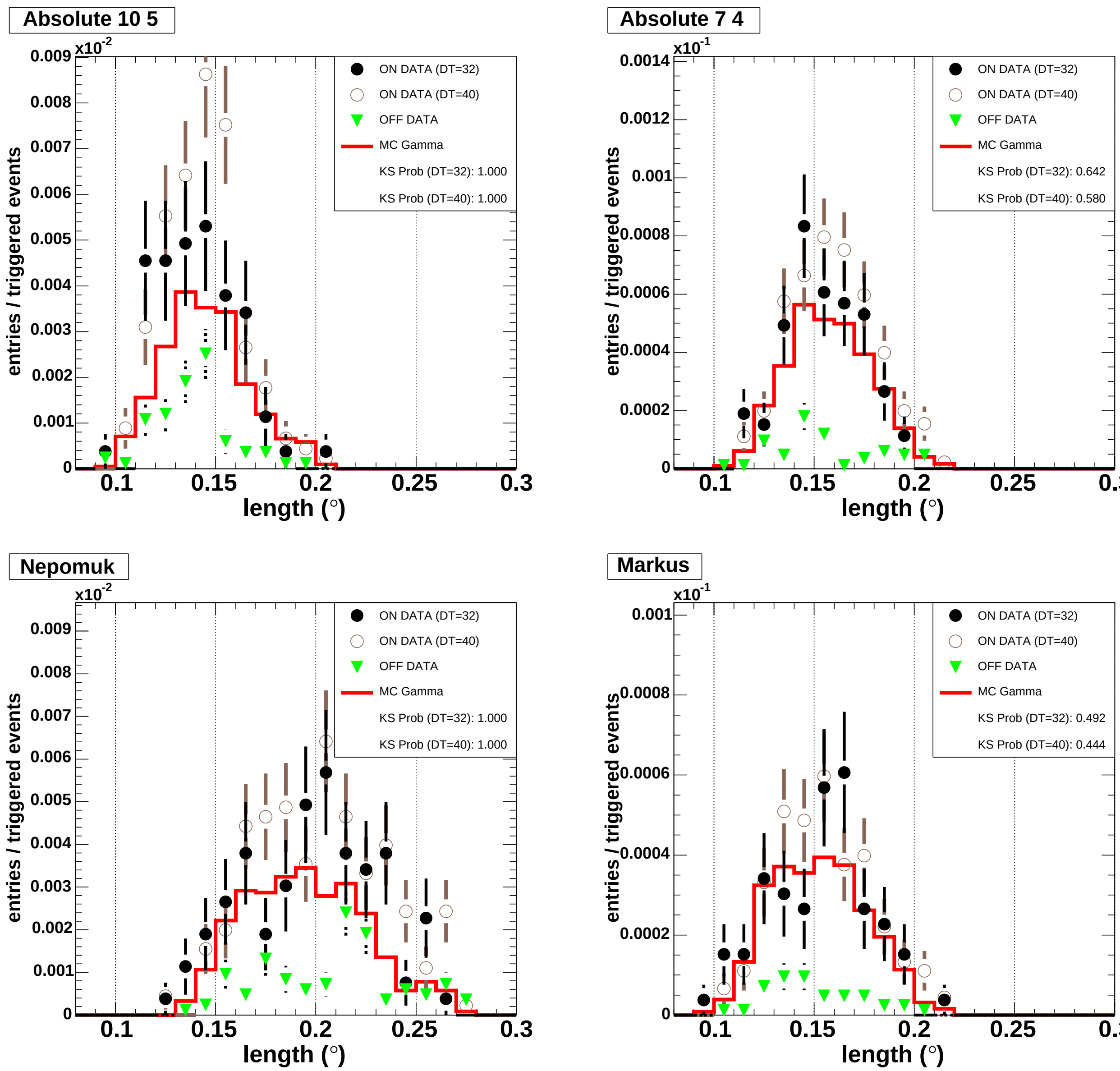

Figure 42: Normalized distributions of the parameter $LENGTH$ for the various image cleaning algorithms and a gamma-enriched Mrk501 data sample. Top left: absolute cleaning with levels 10 and 5 photo-electrons, top right: absolute cleaning with levels 7 and 4 photo-electrons, bottom left: Nepomuk's image cleaning using time coincidence, bottom right: Markus image cleaning using time coincidence.

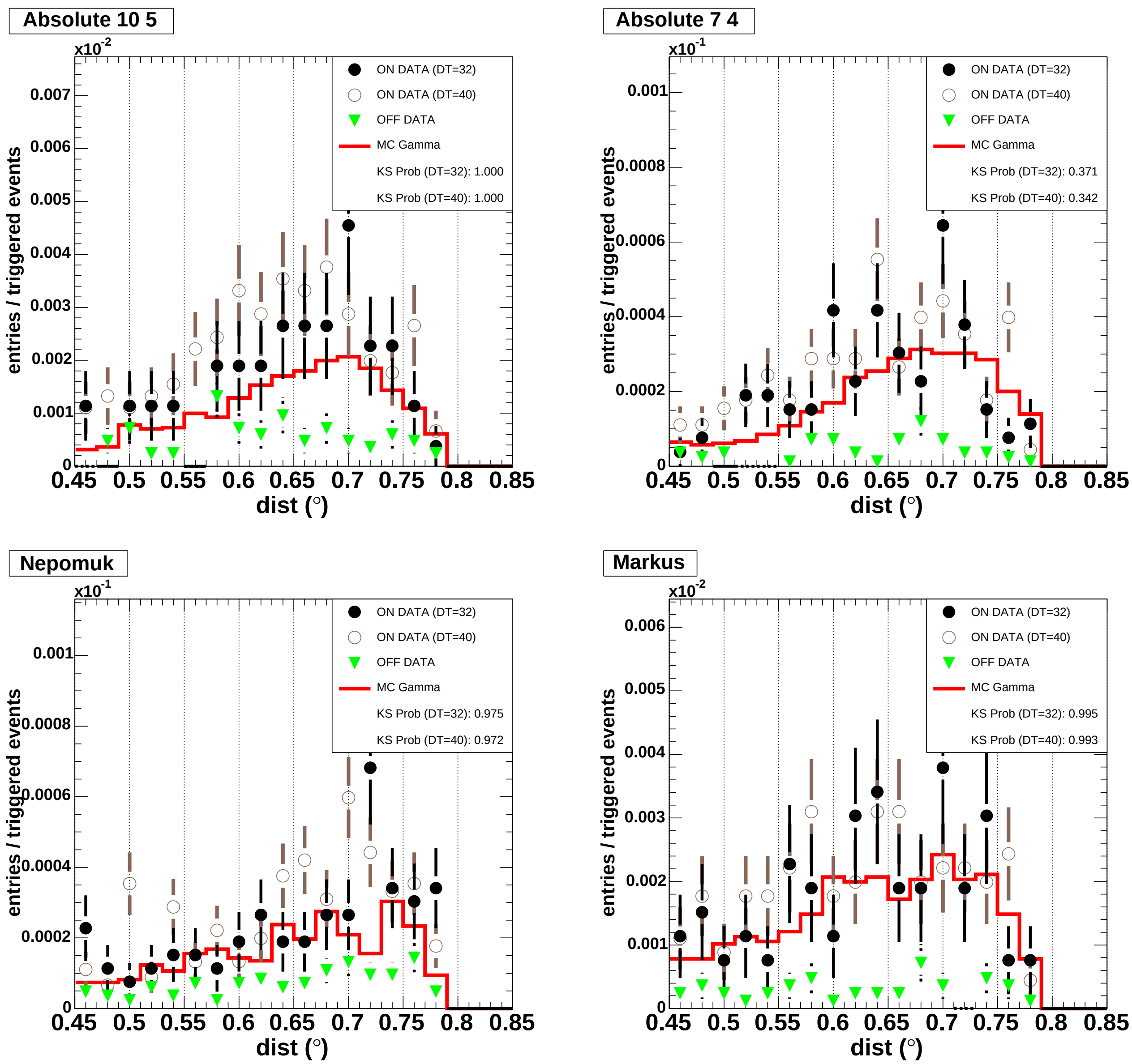

Figure 43: Normalized distributions of the parameter *DIST* for the various image cleaning algorithms and a gamma-enriched Mrk501 data sample. Top left: absolute cleaning with levels 10 and 5 photo-electrons, top right: absolute cleaning with levels 7 and 4 photo-electrons, bottom left: Nepomuk's image cleaning using time coincidence, bottom right: Markus image cleaning using time coincidence.

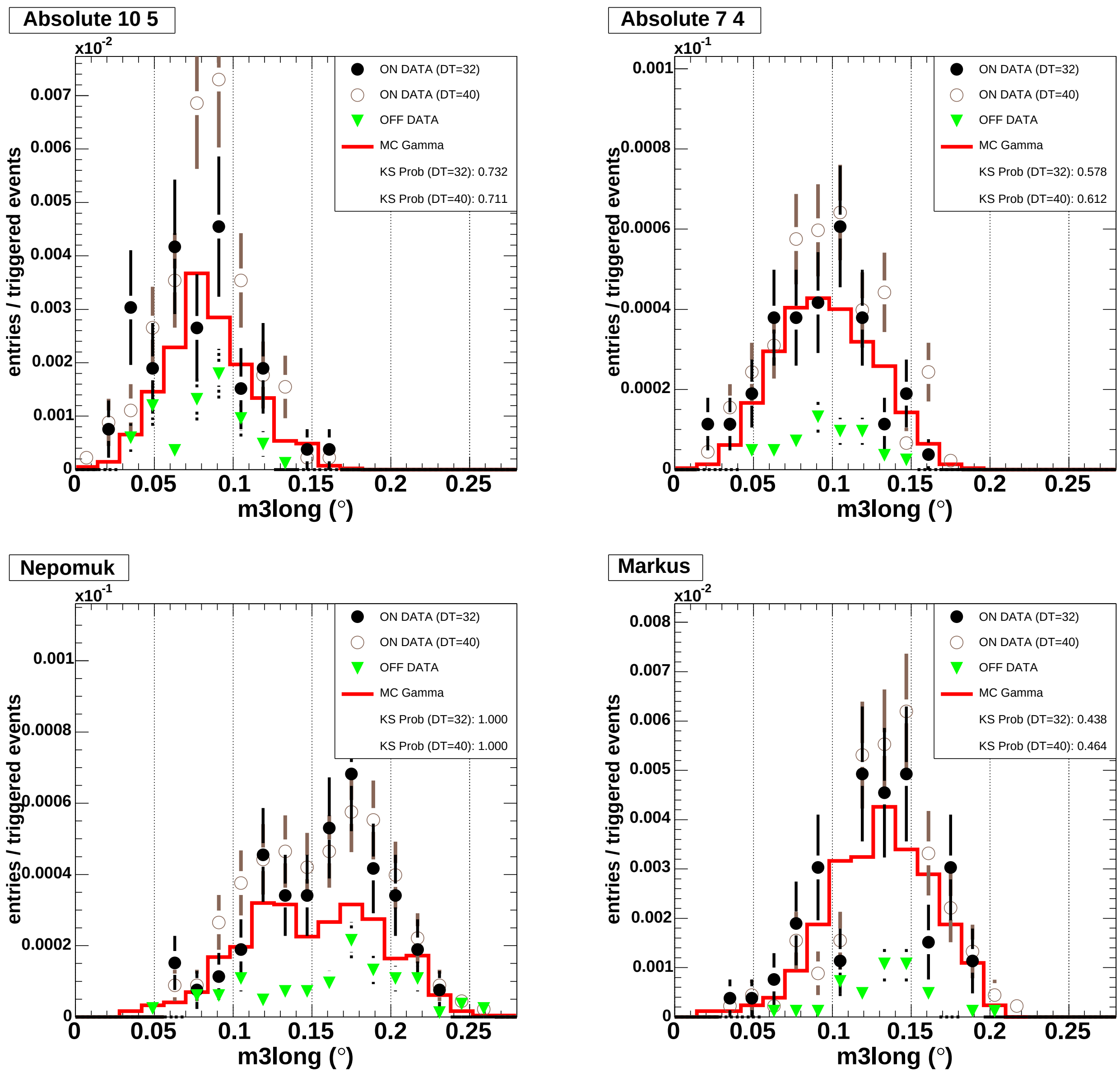

Figure 44: Normalized distributions of the parameter $M3LONG$ for the various image cleaning algorithms and a gamma-enriched Mrk501 data sample. Top left: absolute cleaning with levels 10 and 5 photo-electrons, top right: absolute cleaning with levels 7 and 4 photo-electrons, bottom left: Nepomuk's image cleaning using time coincidence, bottom right: Markus image cleaning using time coincidence.

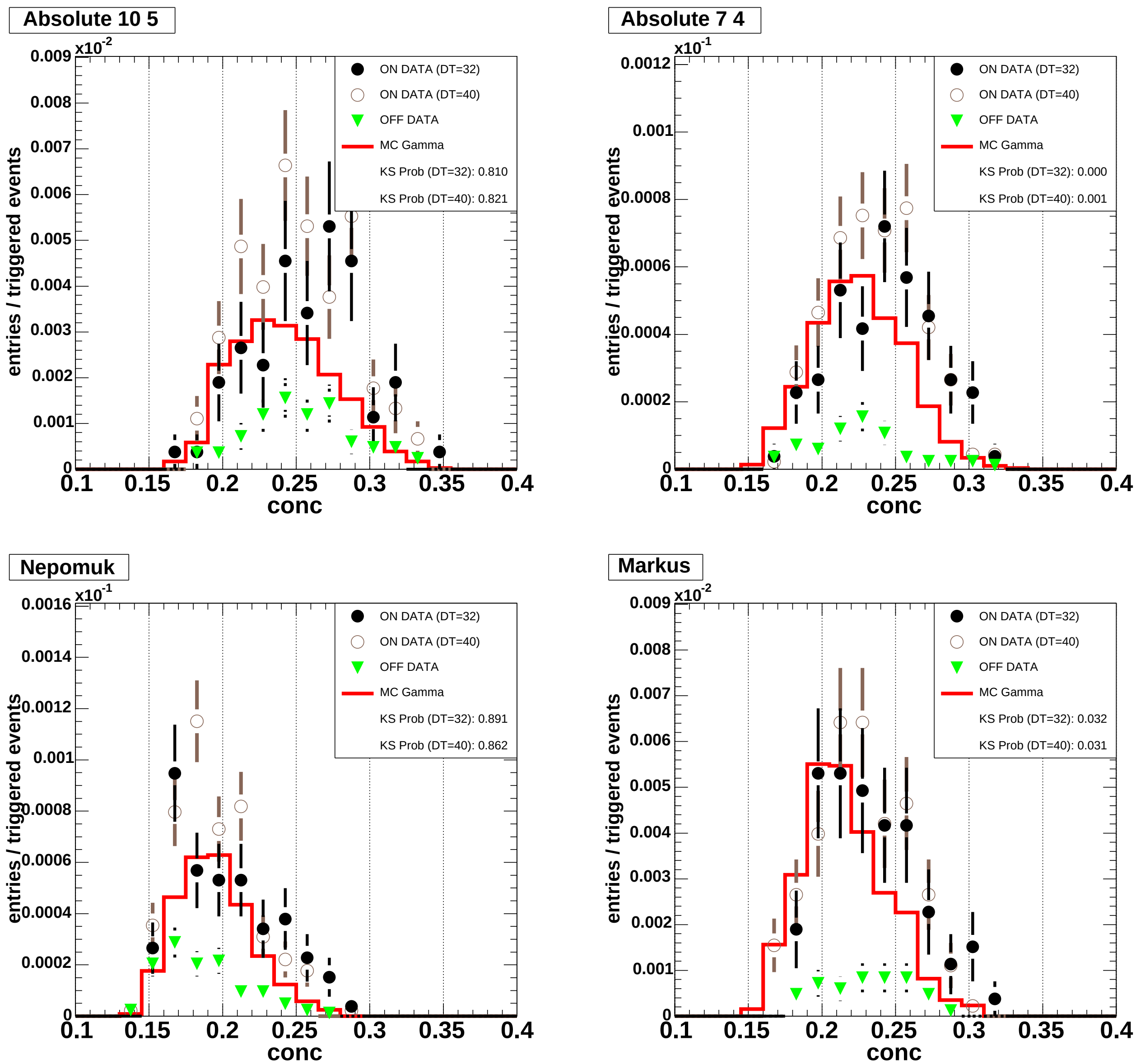

Figure 45: Normalized distributions of the parameter *CONC* for the various image cleaning algorithms and a gamma-enriched Mrk501 data sample. Top left: absolute cleaning with levels 10 and 5 photo-electrons, top right: absolute cleaning with levels 7 and 4 photo-electrons, bottom left: Nepomuk's image cleaning using time coincidence, bottom right: Markus image cleaning using time coincidence.

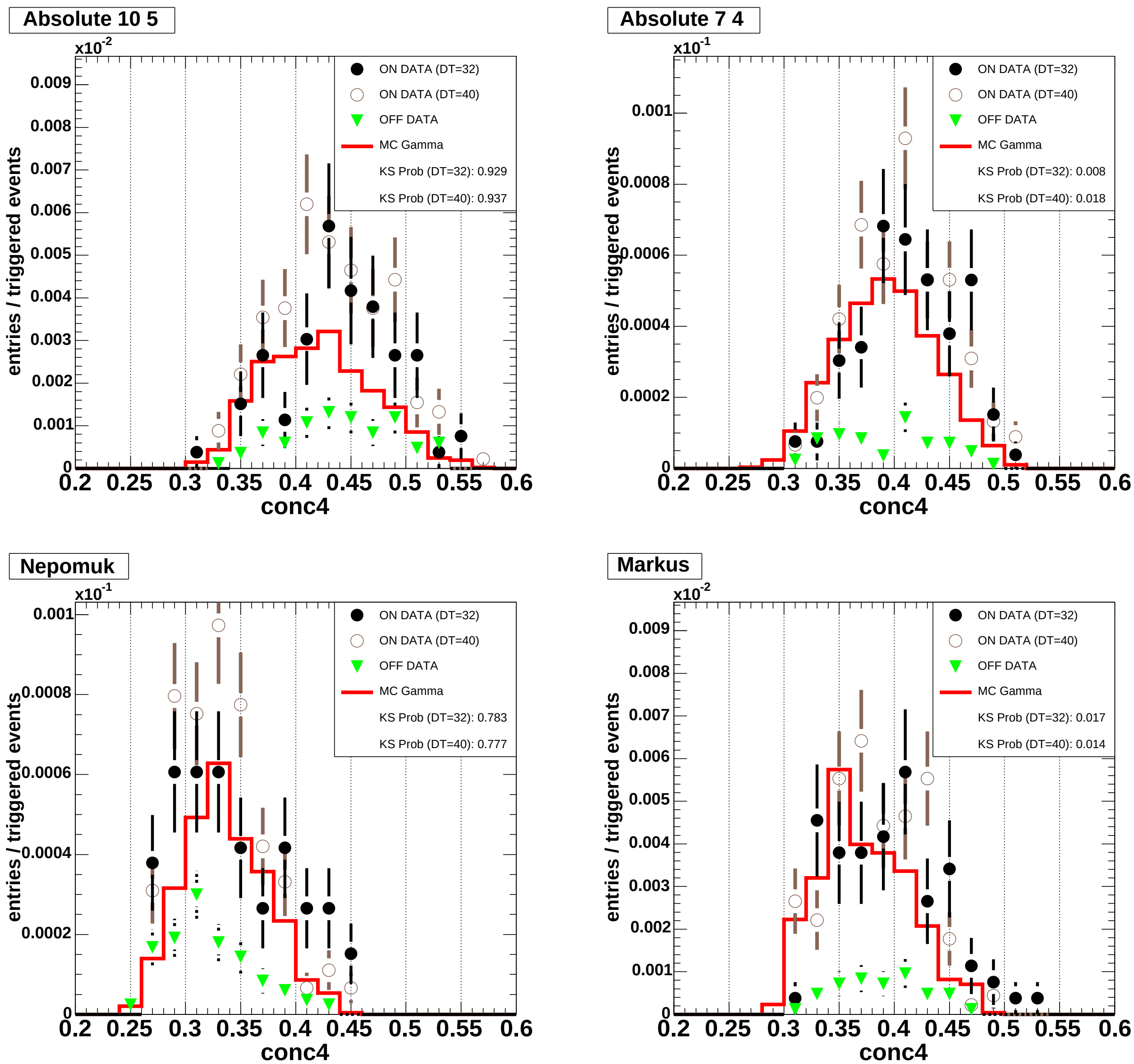

Figure 46: Normalized distributions of the parameter $CONC4$ for the various image cleaning algorithms and a gamma-enriched Mrk501 data sample. Top left: absolute cleaning with levels 10 and 5 photo-electrons, top right: absolute cleaning with levels 7 and 4 photo-electrons, bottom left: Nepomuk's image cleaning using time coincidence, bottom right: Markus image cleaning using time coincidence.

9 Alpha Analysis

At the beginning of the *ALPHA*-analysis, two cuts were re-inforced with respect to the values set in the previous analysis step:

$$ISLANDS < 2 \tag{8}$$
$$LEAKAGE < 0.005 \tag{9}$$

These cuts were found to increase the significances and are not explained in more detail here. In principle, it would have been more efficient to introduce these cuts already before the training of the random forest. However, as we were not completely sure about them, we needed a slightly larger sample for more detailed investigations. In the future, these cuts should be moved to the pre-cuts.

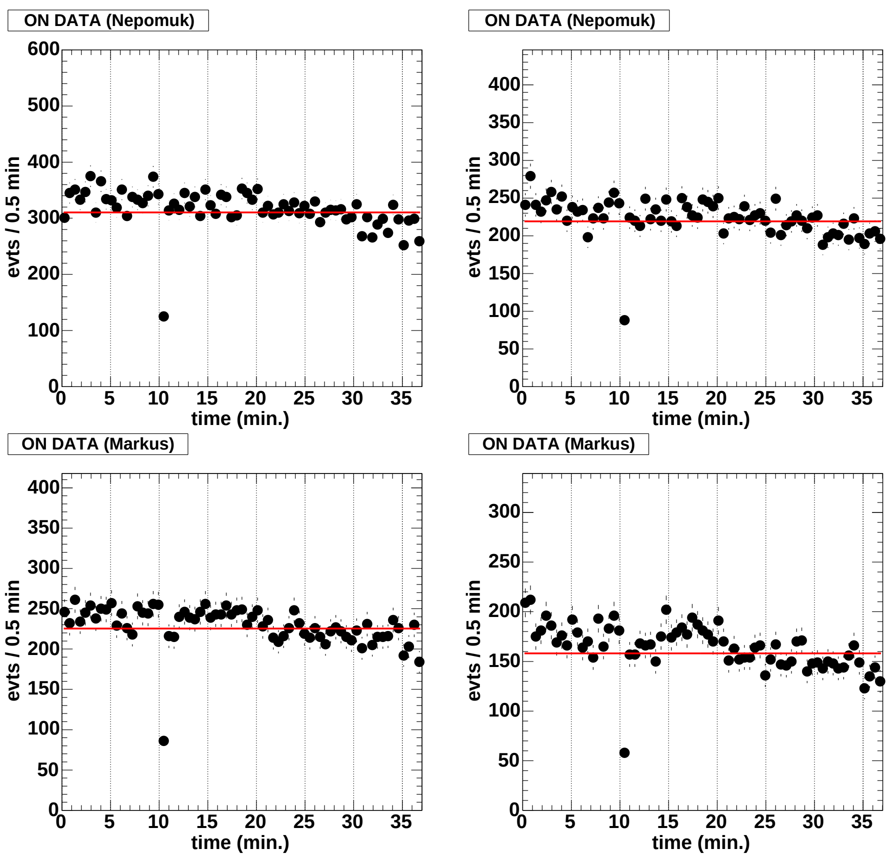

Figure 47: Event rates after very loose cuts on *HADRONNESS* and *ALPHA*, shown in bins of 30 seconds. Top: Nepomuk's image cleaning, bottom: Markus' image cleaning. On the left side, the *HADRONNESS* has been trained using simulated gamma showers and a PSF of $0.05\circ\sigma$, on the right side a PSF of $0.07°\sigma$ was used. All four distributions were fitted to a straight line from after the drop at $T = 10.5$ min. to the end. The fit result is shown as red line (and drawn from $T = 0$ on).

With the resulting sample and very loose cuts on $HADRONNESS < 0.8$ and $ALPHA < 30.$, we plotted the rates, as shown in figure 47. One can observe a global decrease in event rate for both shown image cleanings and used point-spread functions to train the *HADRONNESS*. Additionally, the drop in event rate at $T \approx 10.5\,\text{min.}$ can be seen in all four plots which was due to a stop of data taking. Only the last plot, obtained with Markus' image cleaning and a PSF of $0.07°\sigma$ shows two evident features: A drop at the beginning of the observation and another rise between 15 and 20 minutes. These two features were not found back in the later analysis.

For the subsequent analysis, an additional cut on $SIZE$ was applied:

$$SIZE > 90 \tag{10}$$

This cut follows from inspection of the data with sizes between 60 and 90 photo-electrons and the conclusion that their contributions lead to such a widening of the $ALPHA$-distributions that the results do not look plausible enough any more, even if the significances rise somewhat. In the future, a more detailed inspection of this sample may eventually lead to their inclusion, but we decided to leave them out for the moment for clarity reasons.

Two more cuts are set on the $DIST$ and the $HADRONNESS$ parameters. These cuts, in turn, had to be chosen with special care. Figure 49 shows the distribution of the parameter $DIST$, plotted against the parameter $ALPHA$, obtained with the different image cleaning algorithms and for different data samples. One can see that unfortunately, all image cleaning algorithms result in a structured $ALPHA$-distribution for real data above $DIST \approx 0.8$. Even worse, the structures appear slightly different between ON and OFF data samples. In order to obtain data samples which are in first order un-affected by this effect, we applied a rather strong cut on $DIST$:

$$0.45 < DIST < 0.78 \qquad \text{(Mrk501 data)} \tag{11}$$
$$0.42 < DIST < 0.75 \qquad \text{(GRB050713a data)} \tag{12}$$

Furthermore, the analysis was split into the following bins of reconstructed energy ($ENERGY$). For the Mrk501 data, the following bins were chosen:

1. 45 GeV < $ENERGY$ < 75 GeV
2. 60 GeV < $ENERGY$ < 100 GeV
3. 100 GeV < $ENERGY$ < 150 GeV
4. 150 GeV < $ENERGY$ < 300 GeV

Bins nr. 2–4 correspond to consecutive energy bins containing more or less the same number of events while bin nr. 1 is an attempt to push the energy limit to the absolute minimum.

The GRB050713a data was analysed in two bins:

1. 100 GeV < $ENERGY$ < 200 GeV
2. 200 GeV < $ENERGY$ < 500 GeV

Above 500 GeV, no event survived the $SIZE$ cut of the previous data reduction step.

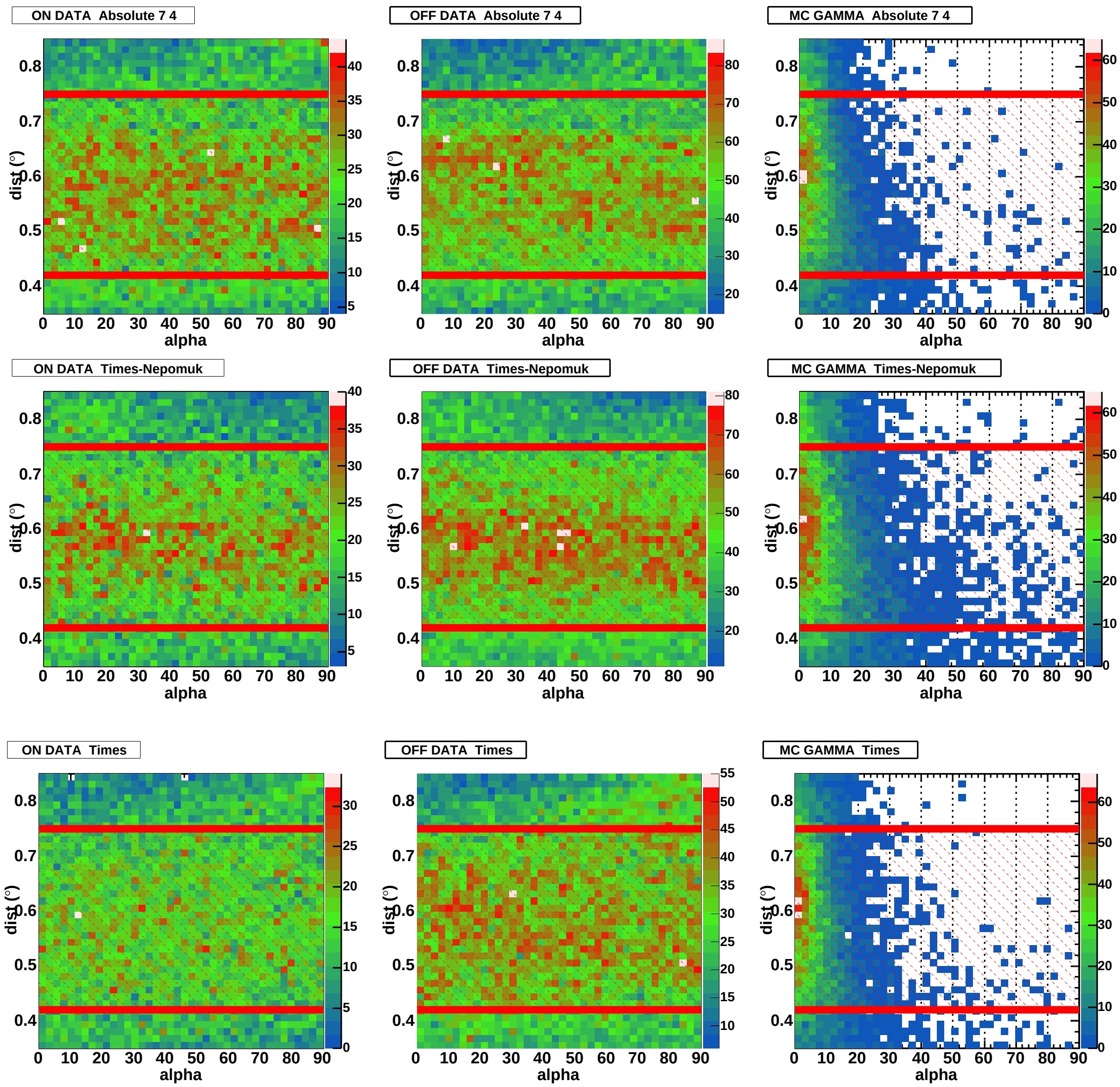

Figure 48: Distributions of the parameters $DIST$ vs. $ALPHA$ for the various image cleaning algorithms and the GRB050713a data. Top: absolute cleaning with levels 7 and 4 photo-electrons, center: Nepomuks image cleaning using time coincidence, bottom: Markus image cleaning using time coincidence. The red lines indicate the final cuts on $DIST$.

9.1 Optimizing Cut on HADRONESS

Figure 49 shows the distributions of the parameter $HADRONNESS$ for the GRB050713a data, obtained with the different image cleaning algorithms and the two different samples of gamma showers, simulated with different point spread functions. One can see a rather good overall agreement between ON and OFF data. Moreover, the algorithms using the time information seem to yield a better separability between the gamma- and hadron- samples. The effect of the worsening of the PSF is rather large if the absolute image cleaning is used and smaller in case that one of the time image cleanings (however still present).

In the following, the cut on $HADRONNESS$ was chosen separately for each bin in $ENERGY$ and each image cleaning algorithm with the following procedure:

1. Determine the cut value on $ALPHA$ by fitting the simulated gamma distribution with a Gaussian. Figure 50 gives examples of such fits. One can see that the width of the $ALPHA$ distribution depends slightly on the energy range. The cut value $ALPHA_{cut}$ was chosen to be 2.5 times the sigma of the Gaussian.

2. Test significances (Li&Ma, form. 5) were calculated scanning the cuts on $HADRONNESS$ from 0 to 1, identifying the following variables:

   - The number of excess events N_{ex} with the number of remaining simulated gamma events, scaled down by a constant factor F_{scale}.
   - The number of background events in the signal region N_{bg} with the number of remaining OFF events, multiplied with $ALPHA_{cut}/90$.
   - The normalization factor with the number of ON events divided by the number of OFF events before any cuts.

   This procedure works if the following conditions are met:

   - Almost the entire signal is contained between $ALPHA = 0$ and $ALPHA = ALPHA_{cut}$. This condition is met automatically by the fact that the gamma events are indeed distributed as a Gaussian around $ALPHA = 0$.
   - A flat distribution of $ALPHA$ for the OFF data such that the number of background events in the signal region is estimated correctly. This condition is almost always met because of the tight cuts applied in $DIST$.
   - The number of ON data before cuts in $HADRONNESS$ and $ALPHA$ is much larger than after such that a possible signal does not modify significantly the estimated normalization factor.
   - ON and OFF data are distributed equally in $HADRONNESS$ such that the estimated normalization factor does not change during the scan through cuts in that variable.
   - The number of excess events matches more or less the expected signal. This condition is met by choosing the signal scale factor F_{scale} such that the obtained maximum test significance is about $5\,\sigma$. In principle, the $HADRONNESS$ position H_{cut} of the maximum significance S_{max} is in first order independent from the total gamma flux, if the expected signal is weak, since:

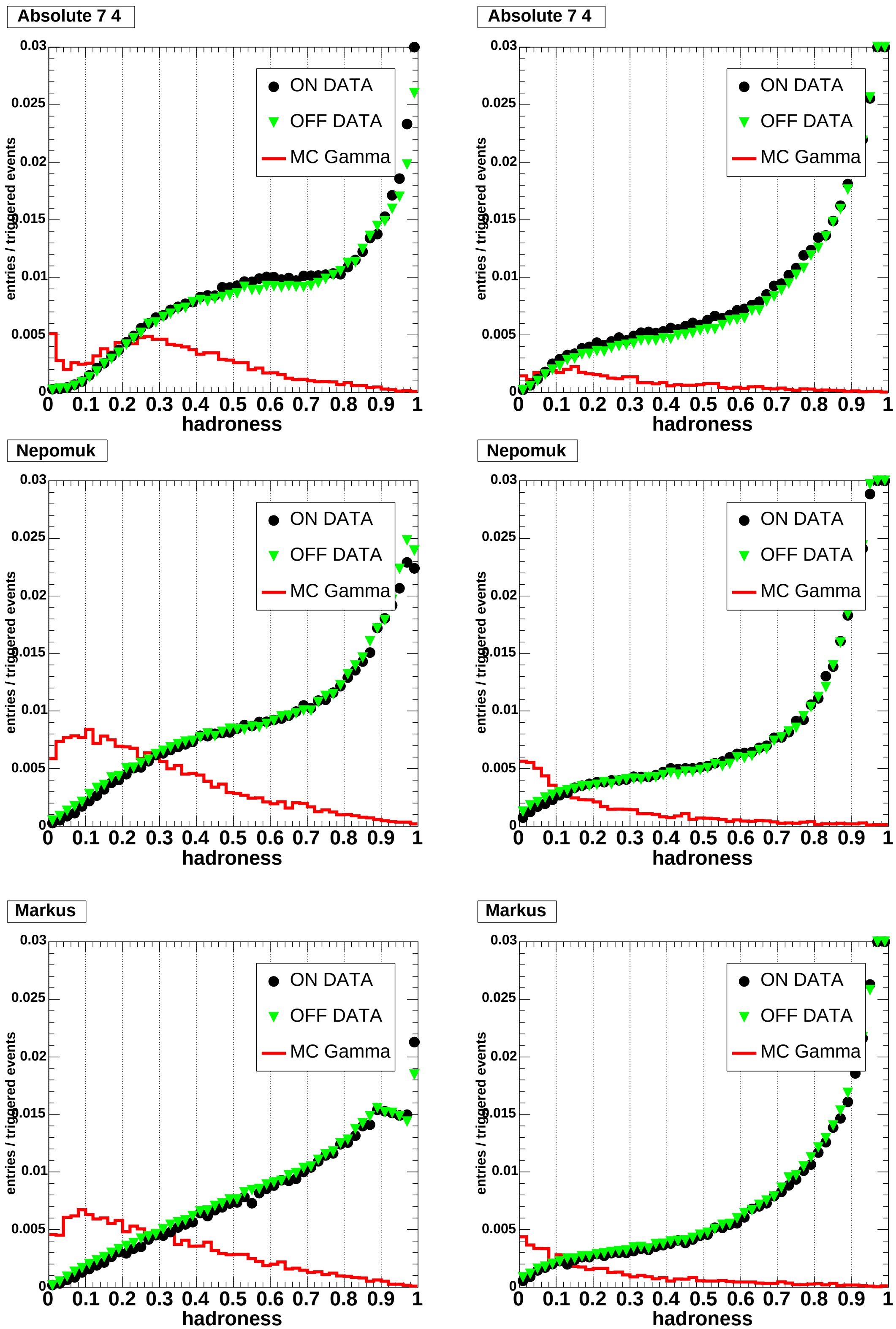

Figure 49: Distributions of the parameter $HADRONESS$ for the various image cleaning algorithms and the GRB050713A data. Top: absolute cleaning with levels 7 and 4 photo-electrons, center: Nepomuk's image cleaning using time coincidence, bottom: Markus image cleaning using time coincidence. On the left side, the Random Forest was trained with the simulated gamma showers and the better PSF ($0.05°\sigma$), one the right side the worse PSF was used ($0.07°\sigma$).

$$\frac{\partial S}{\partial H_{cut}} = \frac{\partial}{\partial H_{cut}} \frac{F_{scale} \cdot N_{ex}}{\sqrt{F_{scale} \cdot N_{ex} + \gamma \cdot N_{bg} + \gamma^2 \cdot N_{bg}}}$$
$$\longrightarrow \quad F_{scale} \cdot \frac{\partial S|_{F=1}}{\partial H_{cut}} \qquad \text{for} \quad F_{scale} \cdot N_{ex} \ll \gamma \cdot N_{bg} \tag{13}$$

With an approximate choice of F_{scale}, we eliminate an error in second order already.

Figure 51 gives an example of such a dependency of the significance on a cut on the parameter $HADRONNESS$ for the two bins in $ENERGY$, obtained from simulated gamma signals and using the ON-data only to compute the normalization factor between ON and OFF-data. It is important to note that this procedure is completely unbiased with respect to fluctuations of the ON data; a very important characteristic for dealing with small or no signals at all.

3. Last, the position of the maximum is taken as cut value on $HADRONNESS$ for all samples, including the ON data.

With this procedure, individual cut values on $HADRONNESS$ were obtained for every bin in $ENERGY$ and every image cleaning algorithm, in the case of the GRB050713a data, the cuts also differ according to the investigated ON data duration.

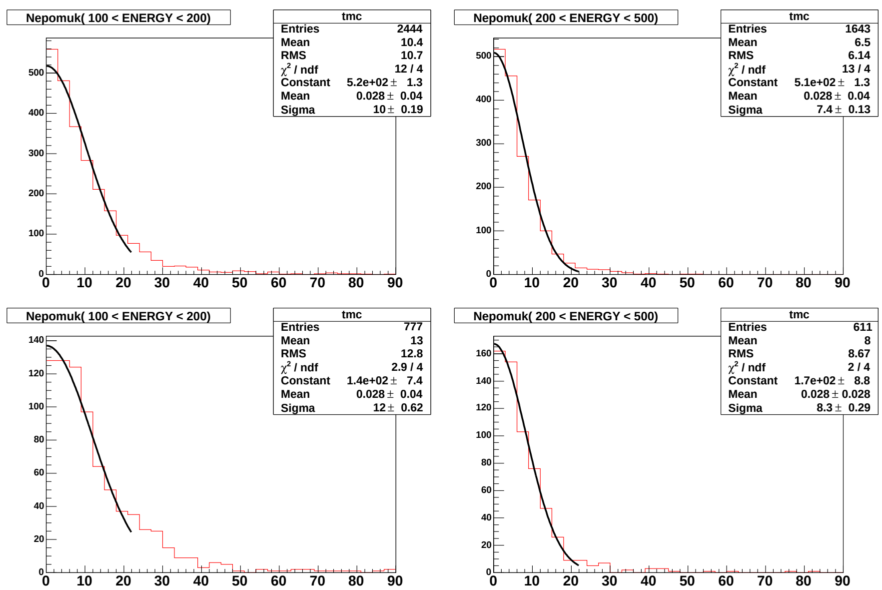

Figure 50: Distributions of $ALPHA$, obtained from simulated gammas with the Nepomuk's image cleaning, for the cuts on $HADRONESS$ obtained for the prompt emission phase of GRB050713a. The left plots correspond to the 100 to 200 GeV slices in reconstructed $ENERGY$, the right plots to 200 to 500 GeV. Top: The better PSF ($0.05°\sigma$), bottom: the worse PSF ($0.07°\sigma$).

9.2 Results Mrk501 Data

Figures 53 through 55 show the resulting $ALPHA$-plots in the different bins of reconstructed energy ("$ENERGY$") with the calculated significances (Li&Ma, form. 17) using ON and OFF-data. Table 6

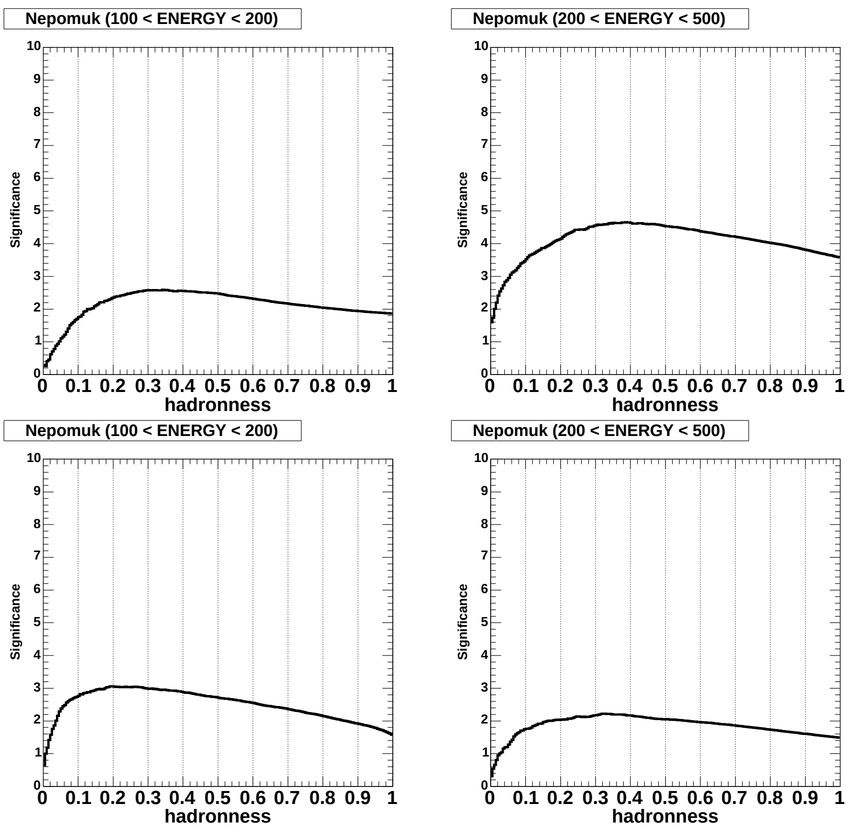

Figure 51: Significance (Li&Ma, form. 5), obtained from simulated gammas, for different cuts on $HADRONESS$ obtained with the Nepomuk's image cleaning The left plots correspond to the 100 to 200 GeV slices in reconstructed $ENERGY$, the right plots to 200 to 500 GeV. Top: The better PSF ($0.05°\sigma$), bottom: the worse PSF ($0.07°\sigma$).

lists the results. One can see that at energies above 100 GeV, the different image cleaning algorithms yield equivalent results, except for Nepomuk's algorithm which results in a lower significance between 100 and 150 GeV. This may be due to a statistical fluctuation of the OFF data between $ALPHA = 10°$ and $ALPHA = 20°$. Below 100 GeV, the image cleaning algorithms using times yield better results, however the absolute cleaning with thresholds of 7 and 4 photo-electrons still produce acceptable significances. It seems, that Markus' algorithm yields the "cleanest" distribution in $ALPHA$, although this criterium should not be taken too serious since the signal is always affected by strong statistical fluctuations.

Figure 52 shows the distribution of the simulated gamma shower energies for the four bins in reconstructed energy, exemplary for Nepomuk's image cleaning. One can see that a mean energy of 61 GeV is obtained in the lowest energy bin, marginally detected with $3.9\,\sigma$. However, the signal in the subsequent bin is detected significantly well above $5\,\sigma$ at a mean energy of 78 GeV. We stress that all numbers on Mrk501 can be improved easily if the OFF data statistics is increased, the data is abundantly available since the telescope conditions did not change during the entire June and the beginning of July, 2005.

The distribution of effective areas for one representative image cleaning is shown in figure 56. We did not perform any unfolding and subsequent calculation of spectra which is out of the scope of this small work on GRB050713a. However, one can already see well the effect of the time image cleaning onto the effective areas in the lowest energy bin: Using e.g. Nepomuk's cleaning more than doubles the effective area below 75 GeV w.r.t. the absolute image cleaning with 7 and 4 photo-electrons.

Concluding this chapter, we have shown to be able to extract a detectable signal well below 80 GeV from only one hour of Mrk501 flare data with our analysis.

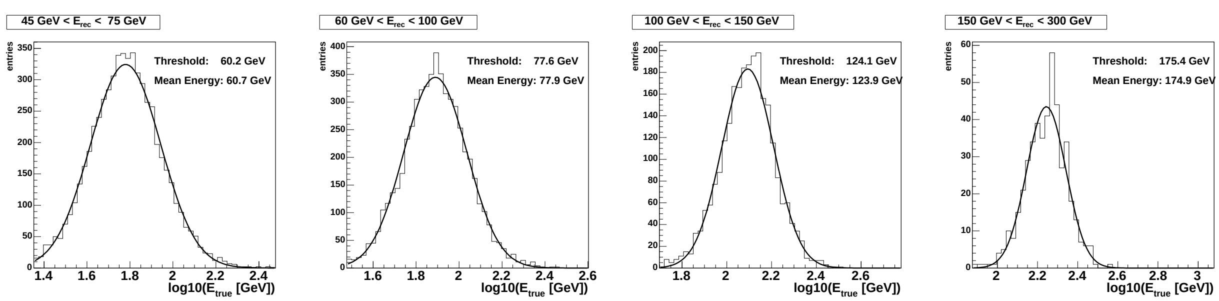

Figure 52: Distributions of the simulated MC energy for the Mrk501 data, obtained with Nepomuk's image cleaning and all cuts applied. The four plots correspond to 4 slices of the $ENERGY$ parameters: 45 to 75, 60 to 100, 100 to 150 and 150 to 300 GeV reconstructed energy.

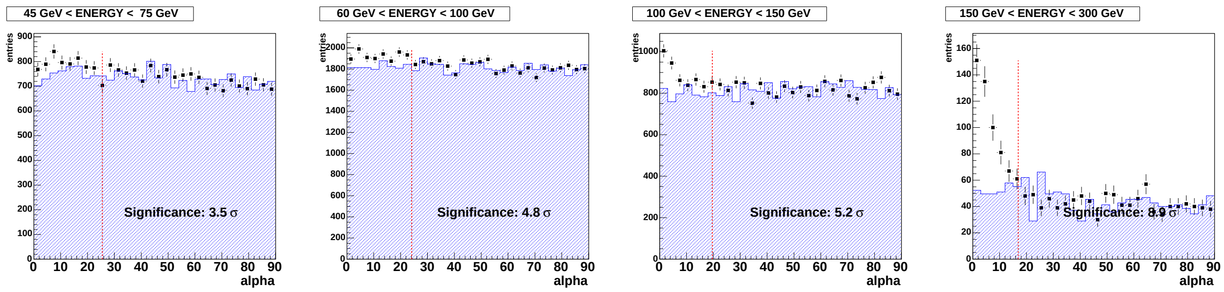

Figure 53: Distributions of the parameter $ALPHA$ for the Mrk501 data, obtained with the absolute image cleaning using 7 and 4 photo-electrons. The four plots correspond to 4 slices of the $ENERGY$ parameters: 45 to 75, 60 to 100, 100 to 150 and 150 to 300 GeV reconstructed energy.

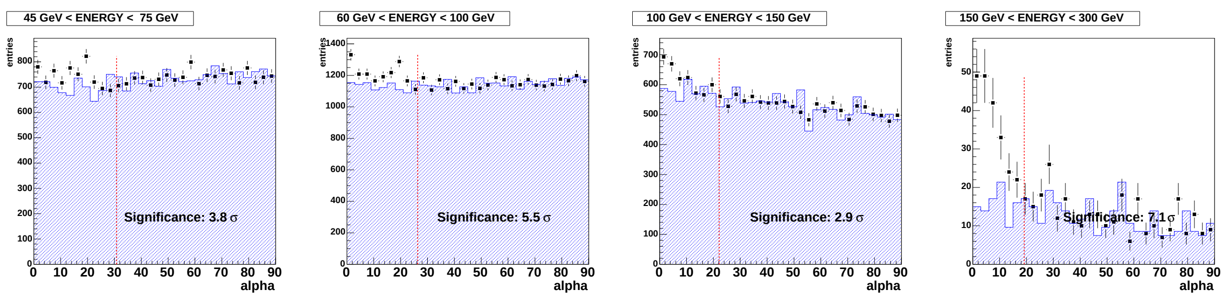

Figure 54: Distributions of the parameter $ALPHA$ for the Mrk501 data, obtained with the Nepomuk's time image cleaning. The four plots correspond to 4 slices of the $ENERGY$ parameters: 45 to 75, 60 to 100, 100 to 150 and 150 to 300 GeV reconstructed energy.

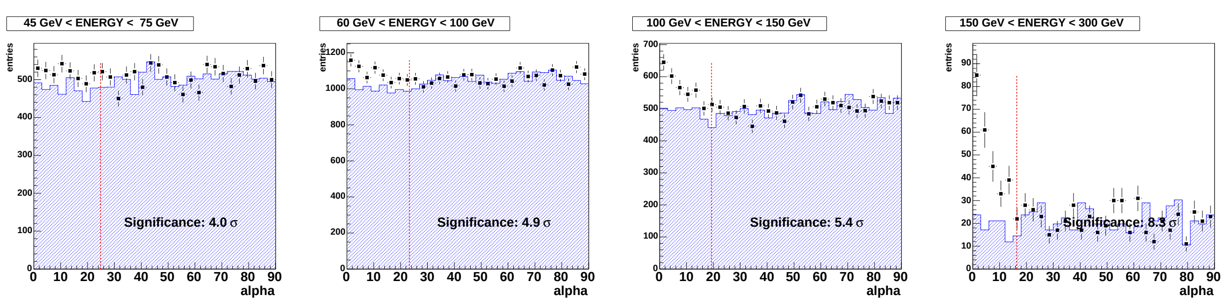

Figure 55: Distributions of the parameter $ALPHA$ for the Mrk501 data, obtained with the Markus' time image cleaning. The four plots correspond to 4 slices of the $ENERGY$ parameters: 45 to 75, 60 to 100, 100 to 150 and 150 to 300 GeV reconstructed energy.

Image Cleaning Method	Reconst. Energy Range (GeV)	cut $HADR.-NESS$	cut alpha (°)	Number Excess Events	Sign. Li Ma	Mean MC Energy (GeV)	Coll. Area at $< E_\gamma >$ 10^8 (cm^2)
Abs. 10 5	45 - 75	0.82	27	140 ± 92	1.5	71	0.1
	60 - 100	0.80	25	702 ± 179	3.9	84	0.7
	100 - 150	0.59	20	567 ± 110	5.1	120	1.4
	150 - 300	0.33	16	318 ± 36	8.7	182	1.4
Abs. 7 4	45 - 75	0.69	26	368 ± 106	3.5	68	0.3
	60 - 100	0.70	24	816 ± 171	4.8	80	1.2
	100 - 150	0.61	20	553 ± 105	5.2	120	1.5
	150 - 300	0.30	17	260 ± 19	8.9	178	1.3
Nepomuk	45 - 75	0.53	31	424 ± 112	3.8	61	0.8
	60 - 100	0.58	26	745 ± 134	5.5	78	1.3
	100 - 150	0.54	22	280 ± 97	2.9	124	1.5
	150 - 300	0.23	19	126 ± 18	7.1	175	0.7
Markus	45 - 75	0.55	25	335 ± 84	4.0	65	0.6
	60 - 100	0.58	23	583 ± 119	4.9	78	1.2
	100 - 150	0.56	19	450 ± 83	5.4	122	1.5
	150 - 300	0.34	16	168 ± 20	8.3	177	0.9

Table 6: Results of the $ALPHA$-analysis for the Mrk501 data.

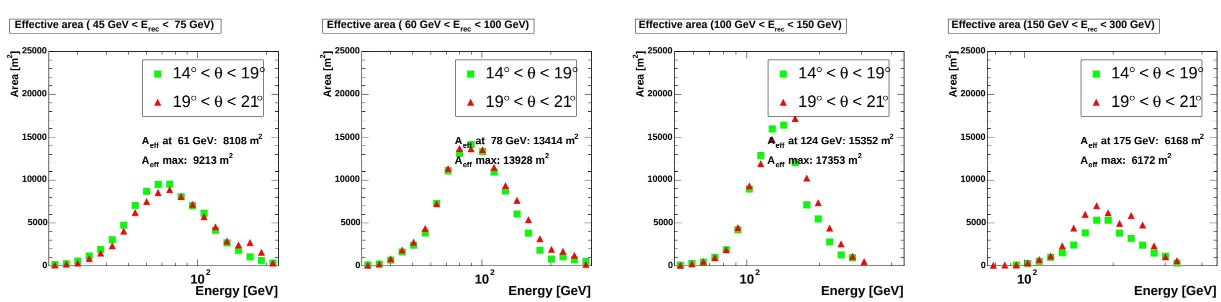

Figure 56: Distributions of the effective area for the Mrk501 data, obtained with the Nepomuk's time image cleaning and all cuts applied. The four plots correspond to 4 slices of the $ENERGY$ parameters: 45 to 75, 60 to 100, 100 to 150 and 150 to 300 GeV reconstructed energy.

9.3 Results GRB050713a Data

The GRB050713a data was analyzed in four ways:

1. Taking the first 90 s of observation which correspond to the prompt emission phases in either the BAT and/or the XRT instrument on SWIFT. The remaining six runs (starting at about 7.7 min after start) as OFF data.
2. Taking the first three runs (about 16 min) as ON data and the rest as OFF data.
3. Taking the entire ON data, compared with the OFF data taken two days later.
4. Searching in time bins of 100 s ON data, using the data outside the corresponding time bin as OFF data.

After applying all the previously explained analysis steps, none of these four searches showed a significant excess over background. For this reason, upper limits were placed starting from the observed number of excess events and the number of background events in the same “signal” region of the alpha distribution. In order to determine the 99% CL upper limit on the number of events in each energy bin, we followed the approach outline in [10]. In a later chapter, the derivation of the averaged effective areas and the differential and integral upper limits will be shown.

9.3.1 Prompt emission phase

After determining the cuts on $HADRONNESS$ and $ALPHA$, energy thresholds of 150 GeV (for the lower bin in reconstructed energy) and 280 GeV (for the upper bin) were obtained (see figure 57).

Figures 58 and 59 show the resulting $ALPHA$-plots in the different bins of reconstructed energy (“$ENERGY$”) with the calculated significances (Li&Ma, form. 17) using ON and OFF-data and Nepomuk’s and Markus’ image cleaning, respectively. No signal can be seen in neither of the two energy bins.

All results of the analysis on the prompt emission phase are summarized in table 7. The obtained significances vary around zero, never exceeding $1.5\,\sigma$. Like in the case of the Mrk501 data, Nepomuk’s algorithm yields the lowest threshold, followed by Markus’ one. The highest effective collection area is also obtained with Nepomuk’s algorithm (for the derivation see chapter 9.4), again followed by Markus’ cleaning.

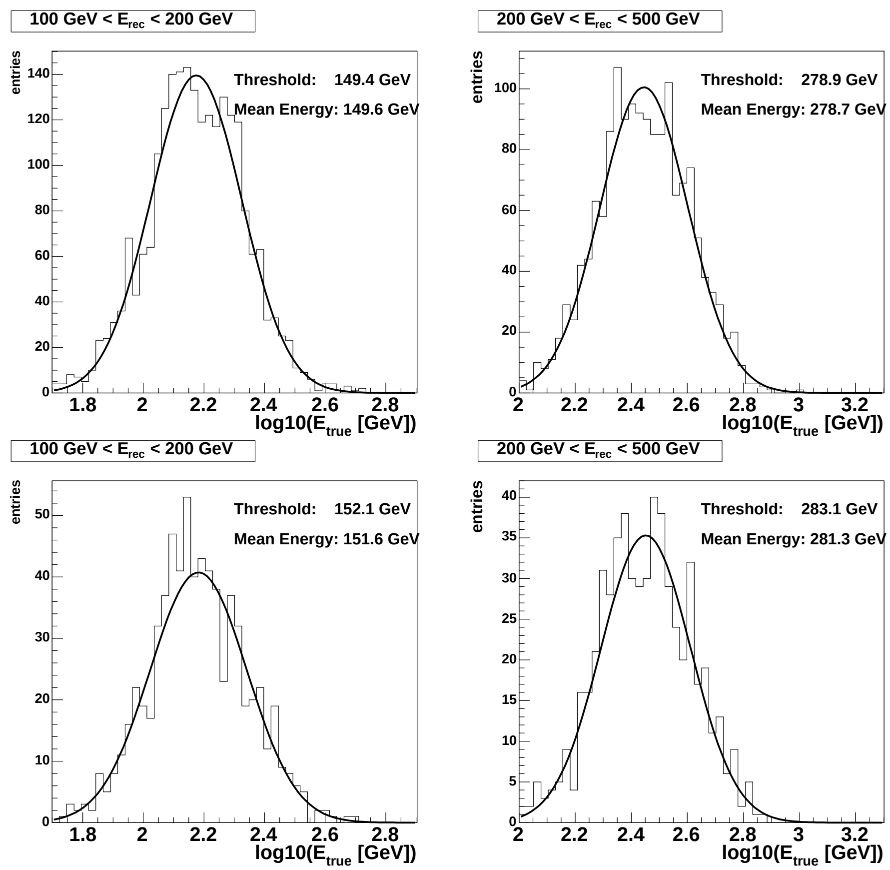

Figure 57: Distributions of the simulated MC energy for the prompt emission phase of GRB050713a, obtained with Nepomuk's image cleaning and all cuts applied. The four plots correspond to two slices of the $ENERGY$ parameters: Left: 100 to 200 GeV and right: >200 GeV reconstructed energy; Top: with cuts optimized using $PSF = 0.05°\sigma$, bottom: using $PSF = 0.07°\sigma$.

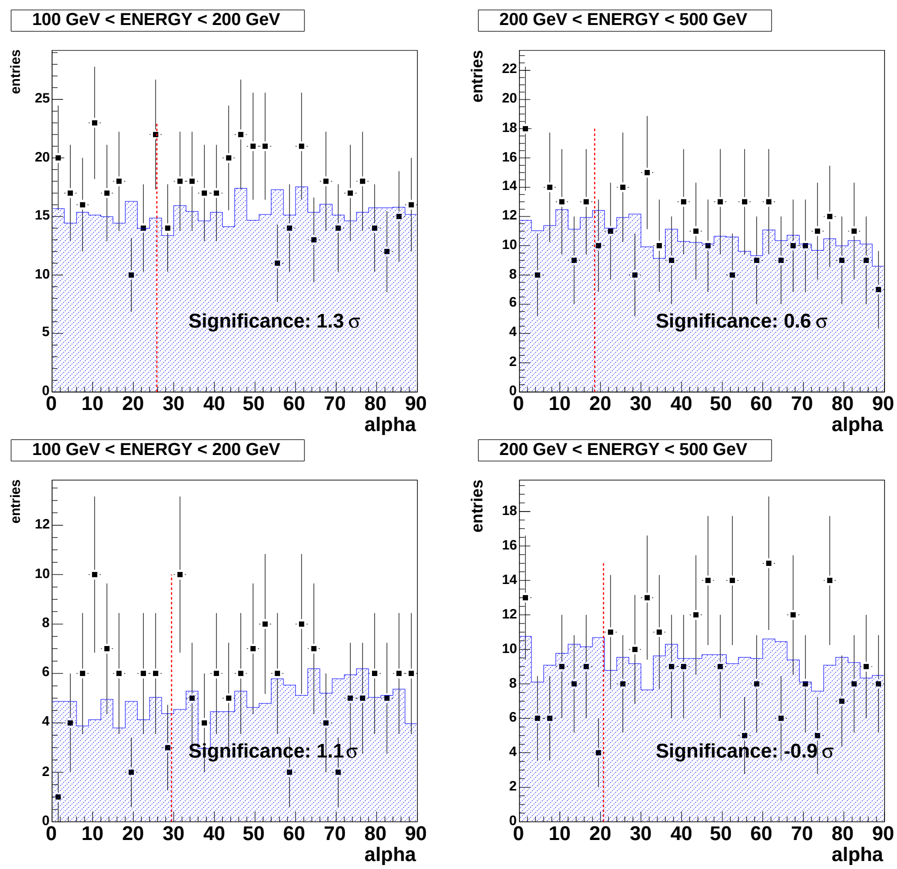

Figure 58: Distributions of the parameter $ALPHA$ for the 90 s of the prompt GRB emission, obtained with the Nepomuk's time image cleaning. The four plots correspond to two slices of the $ENERGY$ parameters: Left: 100 to 200 GeV and right: >200 GeV reconstructed energy; Top: with cuts optimized using $PSF = 0.05°\sigma$, bottom: using $PSF = 0.07°\sigma$. The red line indicates the region where a possible signal is expected.

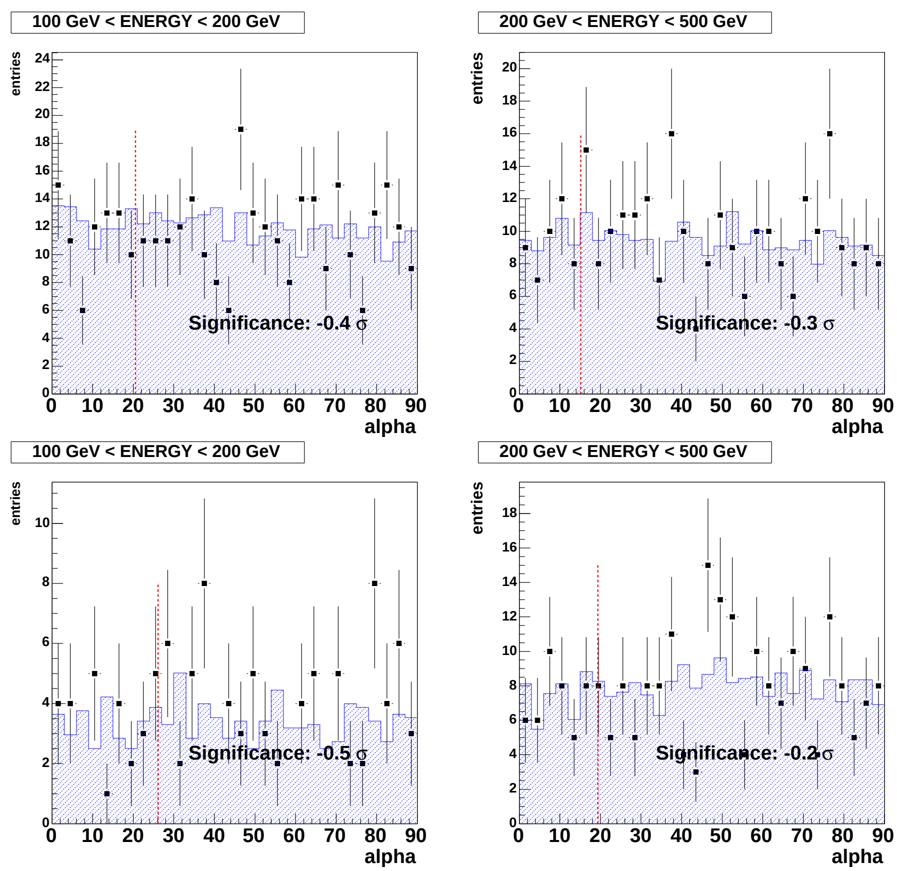

Figure 59: Distributions of the parameter $ALPHA$ for the 90 s of the prompt GRB emission, obtained with the Markus' time image cleaning. The four plots correspond to two slices of the $ENERGY$ parameters: Left: 100 to 200 GeV and right: 200 to 500 GeV reconstructed energy; T Top: with cuts optimized using $PSF = 0.05°\sigma$, bottom: using $PSF = 0.07°\sigma$. The red line indicates the region where a possible signal is expected.

Image Cleaning Method	Reconst. Energy Range (GeV)	cut hadr.-ness	cut alpha (°)	Ex-cess Evts	Sign. Li Ma	U.L. Excess Evts (99% CL)	Mean E_γ MC (GeV)	Coll. Area at $< E_\gamma >$ (10^8 cm^2)	Mean Coll. Area (10^8 cm^2)
Abs. 7 4 (PSF= 0.05°σ)	100 - 200	0.58	23	-2	-0.2	24	173	1.8	1.2
	200 - 500	0.46	16	-2	-0.3	20	288	5.5	5.5
Abs. 7 4 (PSF= 0.07°σ)	100 - 200	0.36	30	-3	-0.6	13	184	1.0	0.9
	200 - 500	0.34	21	-24	-3.2	17	289	7.2	5.4
Nepomuk (PSF= 0.05°σ)	100 - 200	0.52	26	15	1.3	43	150	3.0	2.2
	200 - 500	0.44	19	5	0.6	27	279	5.0	4.8
Nepomuk (PSF= 0.07°σ)	100 - 200	0.28	29	7	1.1	25	152	2.7	1.4
	200 - 500	0.35	21	-7	-0.9	19	281	5.3	4.8
Markus (PSF= 0.05°σ)	100 - 200	0.59	21	-3	-0.4	22	161	2.1	1.6
	200 - 500	0.49	15	-2	-0.3	18	283	4.8	4.8
Markus (PSF= 0.07°σ)	100 - 200	0.26	26	-3	-0.5	13	165	1.7	1.3
	200 - 500	0.36	19	-1	-0.2	18	288	5.6	5.0

Table 7: Results of the *ALPHA*-analysis for the GRB050713a prompt emission data, using the later runs as OFF-data.

9.3.2 First 1000 Seconds

Figure 60 shows the obtained energy thresholds for the two energy bins and the two gamma samples, simulated with the different point spread functions. Like in the case of the prompt emission, thresholds of 150 GeV and 280 GeV are obtained using Nepomuk's image cleaning.

Figure 61 shows the resulting *ALPHA*-plots in the different bins of reconstructed energy ("*ENERGY*") with the calculated significances (Li&Ma, form. 17) using *ON* and *OFF*-data and Nepomuk's image cleaning. No signal can be seen in neither of the two energy bins.

All results of the analysis on the first 1000 seconds observation data are summarized in table 8. The obtained signficances vary around zero, once a signficance of 2.2 *sigma* was seen. The corresponding *ALPHA* plot is shown in figure 61 bottom left. Given the many trials, this excess is perfectly compatible with a statistical fluctuation and therefore considered as background.

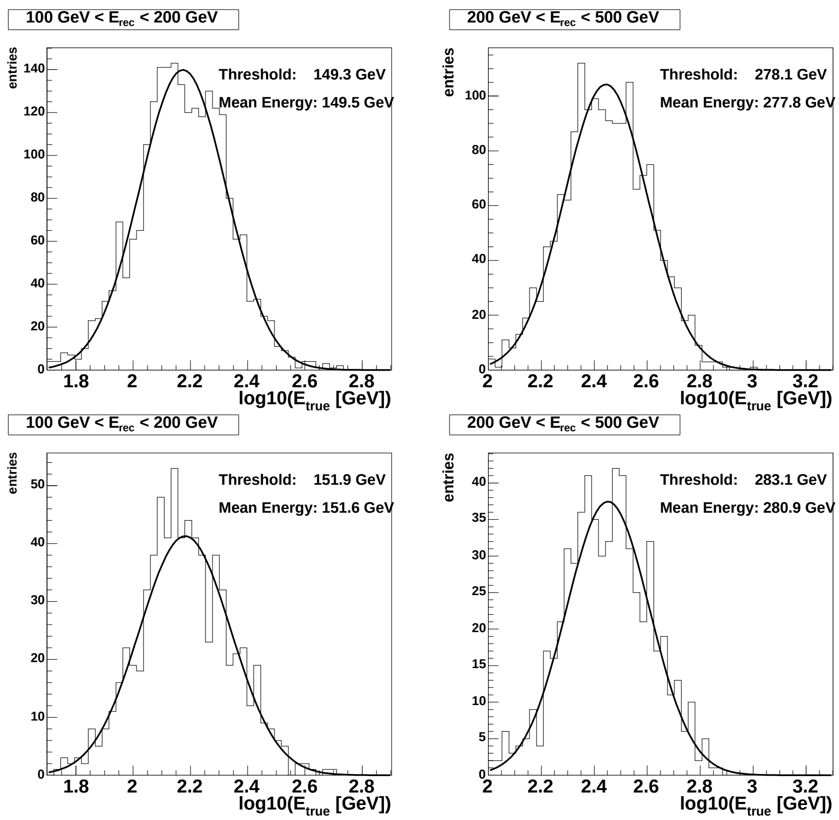

Figure 60: Distributions of the simulated MC energy for the first 1000 s of GRB050713a data, obtained with Nepomuk's image cleaning and all cuts applied. The four plots correspond to two slices of the *ENERGY* parameters: Left: 100 to 200 GeV and right: >200 GeV reconstructed energy; Top: with cuts optimized using $PSF = 0.05°\sigma$, bottom: using $PSF = 0.07°\sigma$. The red line indicates the region where a possible signal is expected.

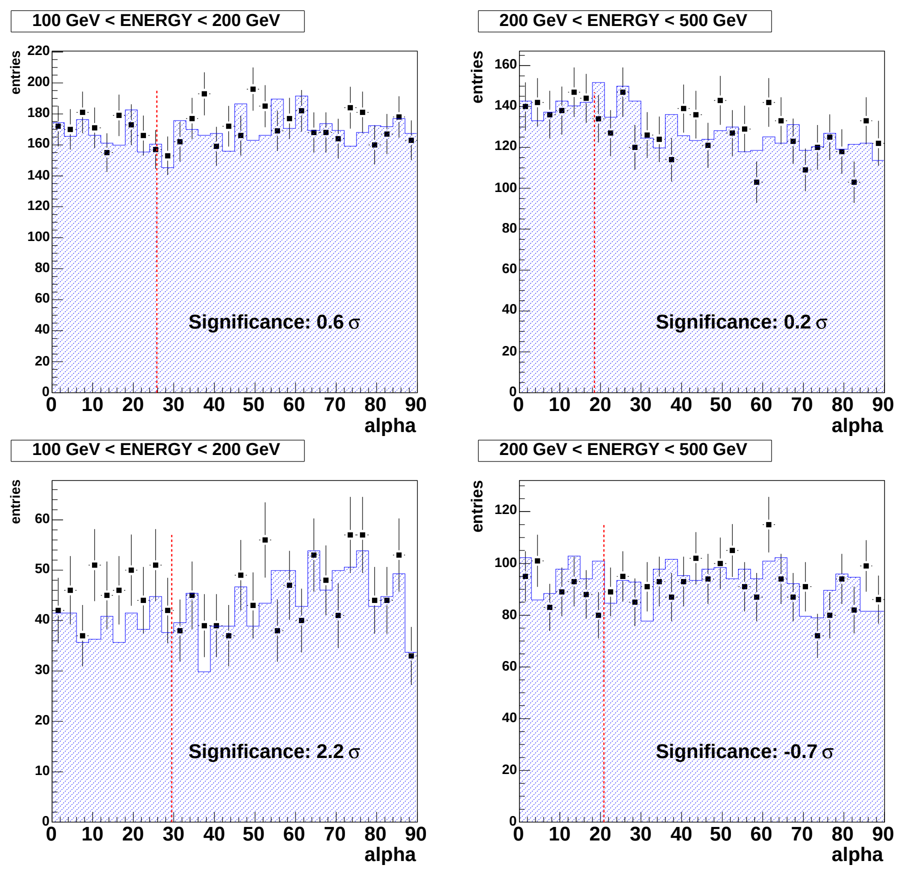

Figure 61: Distributions of the parameter $ALPHA$ for first 1000 s of GRB050713a observation, obtained with the Nepomuk's time image cleaning. The four plots correspond to two slices of the $ENERGY$ parameters: Left: 100 to 200 GeV and right: 200 to 500 GeV reconstructed energy, Top: with cuts optimized using $PSF = 0.05°\sigma$, bottom: using $PSF = 0.07°\sigma$.

Image Cleaning Method	Reconst. Energy Range (GeV)	cut hadr.-ness	cut alpha (°)	Ex-cess Evts	Sign. Li Ma	U.L. Excess Evts (99% CL)	Mean E_γ MC (GeV)	Coll. Area at $< E_\gamma >$ (10^8 cm^2)	Mean Coll. Area (10^8 cm^2)
Abs. 7 4	100 - 200	0.60	23	32	0.8	125	173	1.8	1.2
(PSF= 0.05°σ)	200 - 500	0.50	16	11	0.3	98	286	5.7	5.7
Abs. 7 4	100 - 200	0.36	30	15	0.7	63	184	1.0	0.9
(PSF= 0.07°σ)	200 - 500	0.35	20	-18	-0.6	76	289	7.1	5.4
Nepomuk	100 - 200	0.52	26	26	0.6	141	149	3.0	2.2
(PSF= 0.05°σ)	200 - 500	0.48	19	9	0.2	102	278	5.1	4.9
Nepomuk	100 - 200	0.29	29	56	2.2	116	152	2.8	1.4
(PSF= 0.07°σ)	200 - 500	0.38	21	-22	-0.7	78	281	5.7	5.0
Markus	100 - 200	0.60	21	-16	-0.5	89	161	2.1	1.6
(PSF= 0.05°σ)	200 - 500	0.51	15	-32	-1.1	74	282	5.0	4.8
Markus	100 - 200	0.32	27	9	0.4	57	165	1.9	1.4
(PSF= 0.07°σ)	200 - 500	0.37	19	8	0.3	71	287	5.7	5.0

Table 8: Results of the *ALPHA*-analysis for the GRB050713a data, using the first three run as ON data and the rest as OFF-data.

9.3.3 Entire Data Sample

As with the previous data samples, the same energy thresholds (150 GeV and 280 GeV) were obtained using Nepomuk's image cleaning.

Figures 62 and 63 show the resulting $ALPHA$-plots in the different bins of reconstructed energy ("$ENERGY$") with the calculated significances (Li&Ma, form. 17) using ON and OFF-data and Nepomuk's and Markus' image cleaning, respectively. In one case, on excess of $2.2\,\sigma$ significance was found, which we consider again a statistical fluctuation. These plots and the following tables have to be considered as possibly problematic due to the found disagreements between ON and OFF data. For instance, we know already that the OFF data does not describe too well the background of the ON data (see e.g. figure 49 where offsets between ON and OFF data are observed at small values of $HADRONNESS$).

All results of the analysis on the prompt emission phase are summarized in table 9. The obtained significances seem to be slightly shifted towards positive values, although again not with sufficient significance.

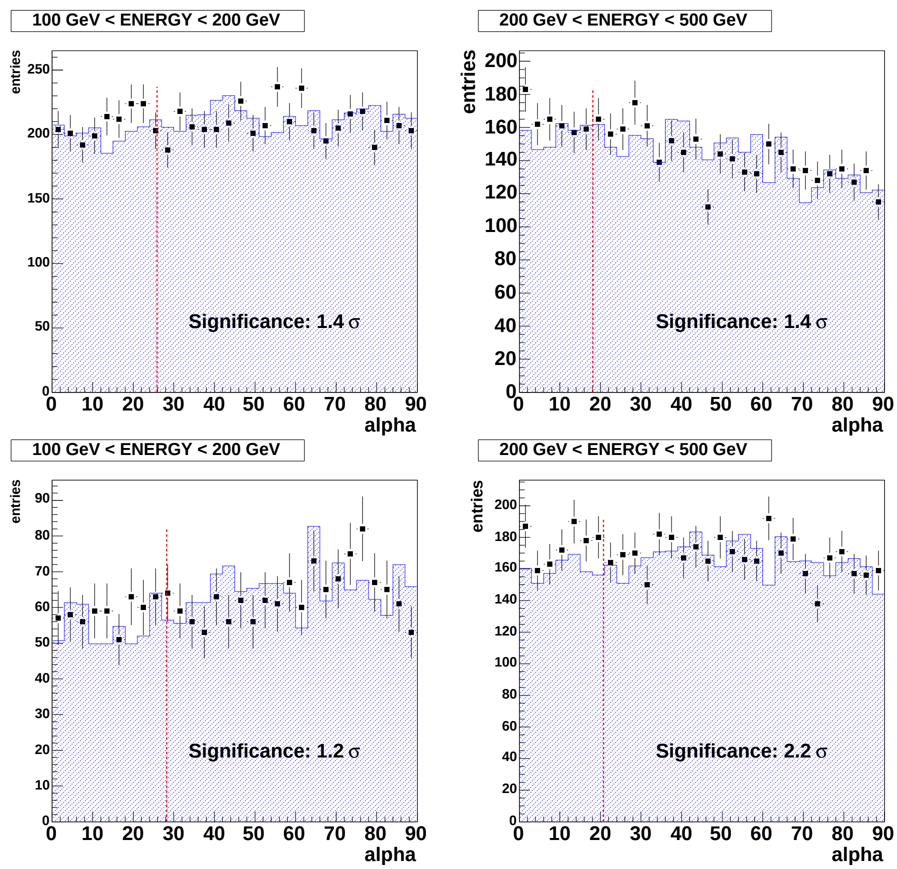

Figure 62: Distributions of the parameter $ALPHA$ for the entire GRB050713a data set, obtained with the Nepomuk's time image cleaning. The four plots correspond to two slices of the $ENERGY$ parameters: Left: 100 to 200 GeV and right: >200 GeV reconstructed energy. Top: with cuts optimized using $PSF = 0.05°\sigma$, bottom: using $PSF = 0.07°\sigma$.

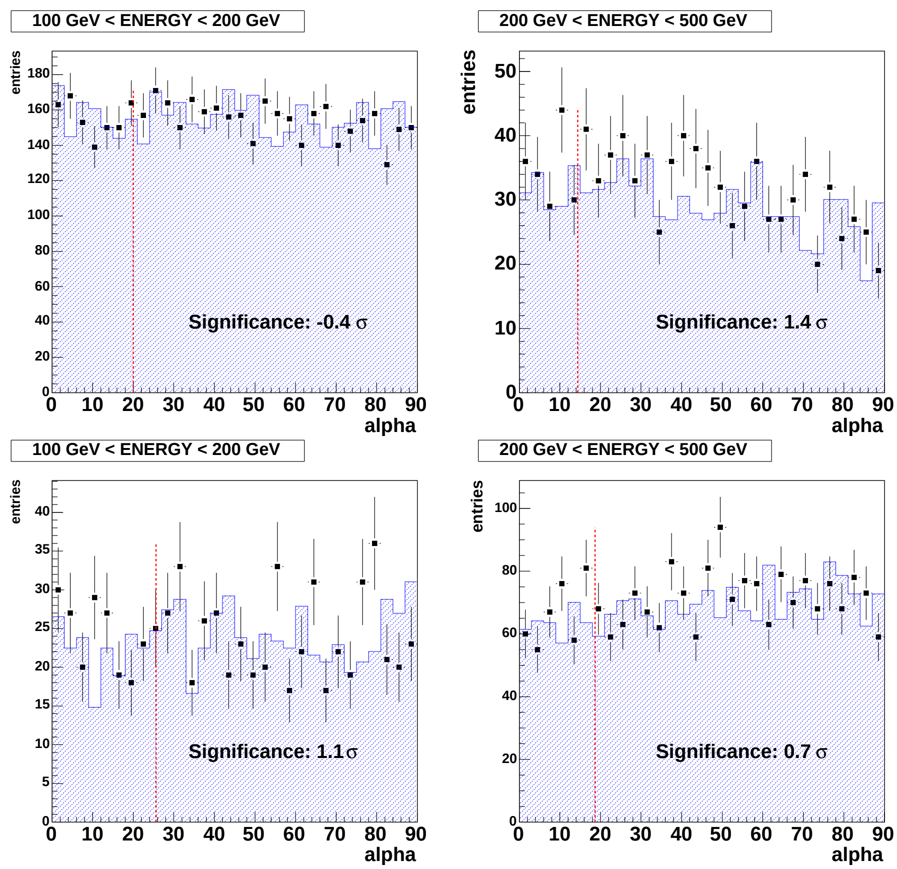

Figure 63: Distributions of the parameter $ALPHA$ for the entire GRB050713a data set, obtained with the Markus' time image cleaning. The four plots correspond to two slices of the $ENERGY$ parameters: Left: 100 to 200 GeV and right: >200 GeV reconstructed energy. T Top: with cuts optimized using $PSF = 0.05°\sigma$, bottom: using $PSF = 0.07°\sigma$.

Image Cleaning Method	Reconst. Energy Range (GeV)	cut hadr.-ness	cut alpha (°)	Ex-cess Evts	Sign. Li Ma	U.L. Excess Evts (99% CL)	Mean E_γ MC (GeV)	Coll. Area at $< E_\gamma >$ (10^8 cm^2)	Mean Coll. Area (10^8 cm^2)
Abs. 7 4 (PSF= 0.05°σ)	100 - 200	0.56	23	-22	-0.4	131	173	1.8	1.2
	200 - 500	0.15	15	33	1.8	77	330	3.8	5.7
Abs. 7 4 (PSF= 0.07°σ)	100 - 200	0.33	30	-9	-0.3	67	182	1.0	0.9
	200 - 500	0.15	19	21	0.9	74	311	4.5	5.4
Nepomuk (PSF= 0.05°σ)	100 - 200	0.39	26	68	1.4	184	148	2.4	2.2
	200 - 500	0.33	18	52	1.4	142	287	4.1	4.7
Nepomuk (PSF= 0.07°σ)	100 - 200	0.21	28	33	1.2	98	152	2.4	1.4
	200 - 500	0.34	21	87	2.2	180	281	5.3	5.0
Markus (PSF= 0.05°σ)	100 - 200	0.46	20	-15	-0.4	95	162	1.8	1.6
	200 - 500	0.18	14	20	1.4	54	318	3.4	4.8
Markus (PSF= 0.07°σ)	100 - 200	0.17	26	17	1.1	57	165	1.4	1.4
	200 - 500	0.21	19	17	0.7	77	299	5.3	5.0

Table 9: Results of the *ALPHA*-analysis for the whole GRB050713a data, using the OFF-data taken two days afterwards.

9.4 Calculation of Effective Areas

We present here our approach to calculate an effective area to be used for an upper limit. The upper limit will be placed at the mean energy E_0, obtained with the chosen cuts, which in our case contain cuts on the reconstructed energy E_{rec}. Our analysis obtains therefore a detector acceptance at and around the mean gamma-ray energy E_0, represented by an energy-dependent effective area $A(E)$ in the chosen energy bin, where E is the "true" energy, obtained from the simulated MC gamma showers. As we derive the limit only in two bins, we neglect further the spill over of events from the lower bin into the larger one and vice-verse. The effective area peaks at or very close to the mean energy E_0. Figure 64 shows a typical distribution of $A(E)$, obtained with Nepomuk's image cleaning.

If we would have to calculate now the detector response to a mono-energetic flux $dN_\gamma/dE = N_0 \cdot \delta(E_0)$, the task would be easy: Take the effective area A_0 at energy E_0 to obtain the number of detected events $N_{det} = N_0/A_0$. In case of an incident gamma ray spectrum, also events with energies lower or higher E_0 produce a detector signal. As the gamma ray spectrum (probably a power law) as well as the energy-dependent effective area are asymmetric around E_0, the results will be different from the case of a mono-energetic flux. Even worse, the derived limit will depend on the assumed gamma-ray spectrum.

We adopt therefore the approach to calculate the effective areas for different representative incident gamma ray spectra:

$$
\begin{aligned}
\frac{dN_\gamma}{dE} &= N_0 \cdot \big(\frac{E}{E_0}\big)^{-\alpha} \\
\frac{dN_\gamma}{dE} &= N_0 \cdot \exp\big(-\frac{E-E_0}{E_b}\big)\ ,
\end{aligned}
\tag{14}
$$

where E_0 is the mean energy at which the limit is calculated and α the tried spectral indices: 1.0, 2.0, 2.25, 2.5 and 3.0. A second function simulating an exponential cut-off with a break energy at $E_b = 200\,\mathrm{GeV}$ was also tested [1]. Derived limits apply then to the constant N_0, i.e.: $N_0 = N_0(\alpha) < N_{U.L.}$.

The next step is straight-forward: We average the effective area $A(E)$ using the spectrum dN_γ/dE:

$$
< A_{eff}(\alpha) >= \frac{\int_{E_{min}}^{E_{max}} A(E) \frac{dN_\gamma}{dE}\, d\,E}{\int_{E_{min}}^{E_{max}} \frac{dN_\gamma}{dE}\, d\,E}
\tag{15}
$$

Because we have dA/dE only in bins of energy ΔE_i around E_i, we discretize equation 15:

$$
< A_{eff}^{disc.}(\alpha) >= \frac{\sum_{E_{min}}^{E_{max}} A_i N_\gamma(E_i)}{\sum_{E_{min}}^{E_{max}} N_\gamma(E_i)}\ ,
\tag{16}
$$

where $N_\gamma(E_i)$ is the integral number of gamma events in the energy bin i. Tables 7, 8 and 9 have already listed some effective areas $A_{eff}(< E_\gamma >)$ at the mean gamma energy E_0 and the mean effective areas $< A_{eff}^{disc} >$, obtained with a spectral index of $\alpha = 2.25$. One observes that the mean effective areas are usually lower than the peak area.

[1] We also tested lower break energies, with the effect that all upper limits simply improved. These results are not further shown in the tables.

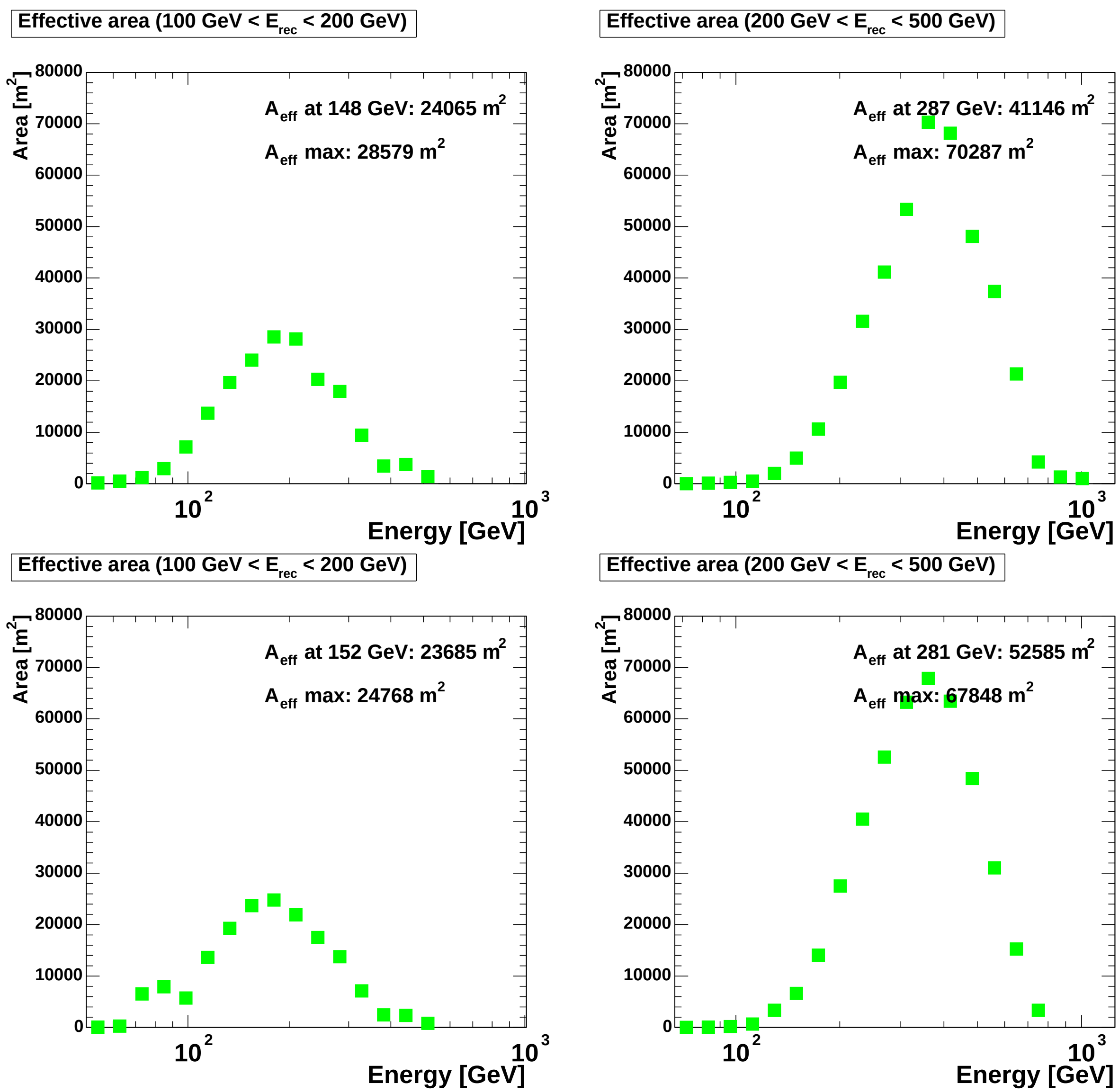

Figure 64: Distributions of the effective area, obtained with the Nepomuk's time image cleaning and the cuts derived for the entire sample of GRB050713a. The four plots correspond to two slices of the $ENERGY$ parameters: Left: 100 to 200 GeV and right: 200 to 500 GeV reconstructed energy. Top: with cuts optimized using $PSF = 0.05°\sigma$, bottom: using $PSF = 0.07°\sigma$.

9.5 Calculation of the Upper Limits

Usually, knowing a flux $d\Phi_\gamma/dE$ and an energy-dependent effective area $A(E)$, one can calculate the number of events registered by the detector following:

$$N_{obs} = \int_{E_{min}}^{E_{max}} \frac{d\Phi}{dE} \cdot A(E)\, dE \cdot T_{obs} \tag{17}$$

where E_{min} and E_{max} are the limits of our (small) energy bin and T_{obs} is the observation time.
We now want to go backwards to define an average flux as

$$\int_{E_{min}}^{E_{max}} \frac{d\Phi}{dE} \cdot A(E)\, dE \quad \longrightarrow \quad < \frac{d\Phi}{dE} > \cdot < A_{eff}(E_0) > \cdot < dE > \tag{18}$$

and subsequently a differential upper flux limit of the form:

$$< \frac{d\Phi}{dE} > |_{E_0} \qquad < \qquad \frac{N_{>\,99\%}}{< A_{eff}(E_0) > \cdot < dE > \cdot T_{obs}} \tag{19}$$

Identifying the terms $< A_{eff} >$ with equation 15 and:

$$< dE > \quad = \quad \int_{E_{min}}^{E_{max}} \frac{dN_\gamma}{dE}\, dE \quad / \quad \frac{dN_\gamma}{dE}\, |_{E_0} \tag{20}$$

and

$$N_{obs} \;=\; N_0 \;\equiv\; N_{>99\%} \tag{21}$$

yields equation 17.
Analogously, the integral limit on the energy fluence is obtained using:

$$< \Phi > |_{E_{min}}^{E_{max}} \qquad = \qquad \frac{N_{>\,99\%} \cdot < E_0 >}{< A_{eff}^{E} >}\ , \tag{22}$$

where $< E_0 >$ is the average energy and $< A_{eff}^{E} >$ the energy averaged effective area:

$$< A_{eff}^{E}(\alpha) > \quad = \quad \frac{\int_{E_{min}}^{E_{max}} A(E) \frac{dN_\gamma}{dE} \cdot E_\gamma\, dE}{\int_{E_{min}}^{E_{max}} \frac{dN_\gamma}{dE} \cdot E_\gamma\, dE}\ . \tag{23}$$

Discretized, equation 23 is written:

$$< A_{eff}^{E,disc}(\alpha) > \quad = \quad \frac{\sum_{E_{min}}^{E_{max}} A_i \cdot N_\gamma(E_i) \cdot E_i}{\sum_{E_{min}}^{E_{max}} N_\gamma(E_i) \cdot E_i}\ . \tag{24}$$

Note that the total fluence limit depends on the integration limits and is not very useful, if provided in fine energy bins. We list these numbers here only to be comparable with the results from [1].

All obtained limits are compatible w.r.t. the different image cleaning methods if a global statistical uncertainty of about 10% is assumed and the fact taken into account that the limits are placed at slightly different energies.

Tables 10, 11 and 12 list the differential upper flux limits, obtained from the first 90 seconds of GRB050713a observation, the first 1000 seconds and the whole data sample, respectively. As the observation times scale more or less like 1:10:25, the derived differential flux limits should scale more or less like the one over the square root of these numbers which is the case.

The limit at the lowest mean energy is obtained with Nepomuk's image cleaning. Taking into account the uncertainties due to the unknown incident spectrum and the possible degradation of the point spread function, the following global result is obtained:

$$< \frac{d\Phi}{dE} > |_{150\,\mathrm{GeV}} \quad < \quad 1.1 \cdot 10^{-17}\ \mathrm{ph/cm^2/keV/s} \qquad \text{first } 90\,\mathrm{s} \tag{25}$$
$$< \frac{d\Phi}{dE} > |_{150\,\mathrm{GeV}} \quad < \quad 3.4 \cdot 10^{-18}\ \mathrm{ph/cm^2/keV/s} \qquad \text{first } 1000\,\mathrm{s} \tag{26}$$
$$< \frac{d\Phi}{dE} > |_{150\,\mathrm{GeV}} \quad < \quad 2.5 \cdot 10^{-18}\ \mathrm{ph/cm^2/keV/s} \qquad \text{entire } 2223\,\mathrm{s} \tag{27}$$

$$< \frac{d\Phi}{dE} > |_{280\,\mathrm{GeV}} \quad < \quad 1.9 \cdot 10^{-18}\ \mathrm{ph/cm^2/keV/s} \qquad \text{first } 90\,\mathrm{s} \tag{28}$$
$$< \frac{d\Phi}{dE} > |_{280\,\mathrm{GeV}} \quad < \quad 6.4 \cdot 10^{-19}\ \mathrm{ph/cm^2/keV/s} \qquad \text{first } 1000\,\mathrm{s} \tag{29}$$
$$< \frac{d\Phi}{dE} > |_{280\,\mathrm{GeV}} \quad < \quad 5.3 \cdot 10^{-19}\ \mathrm{ph/cm^2/keV/s} \qquad \text{entire } 2223\,\mathrm{s} \tag{30}$$

Tables 13, 14 and 15 list the integral upper fluence limits, obtained from the first 90 seconds of GRB050713a observation, the first 1000 seconds and the whole data sample, respectively. As the observation times scale more or less like 1:10:25, the derived fluence limits should scale more or less like the square root of these numbers which is the case.

Unfortunately, the integration limits change slightly due to the different efficiencies at the edges of the different cleaning algorithms. If we consider again the results obtained with Nepomuk's image cleaning, we get:

$$< \Phi > (70 - 550\mathrm{GeV}) \quad < \quad 7.0 \cdot 10^{-8}\ \mathrm{erg/cm^2} \qquad \text{first } 90\,\mathrm{s} \tag{31}$$
$$< \Phi > (70 - 550\mathrm{GeV}) \quad < \quad 2.3 \cdot 10^{-7}\ \mathrm{erg/cm^2} \qquad \text{first } 1000\,\mathrm{s} \tag{32}$$
$$< \Phi > (70 - 550\mathrm{GeV}) \quad < \quad 3.0 \cdot 10^{-7}\ \mathrm{erg/cm^2} \qquad \text{entire } 2223\,\mathrm{s} \tag{33}$$

$$< \Phi > (160 - 700\mathrm{GeV}) \quad < \quad 2.9 \cdot 10^{-8}\ \mathrm{erg/cm^2} \qquad \text{first } 90\,\mathrm{s} \tag{34}$$
$$< \Phi > (160 - 700\mathrm{GeV}) \quad < \quad 1.0 \cdot 10^{-7}\ \mathrm{erg/cm^2} \qquad \text{first } 1000\,\mathrm{s} \tag{35}$$
$$< \Phi > (160 - 700\mathrm{GeV}) \quad < \quad 1.9 \cdot 10^{-7}\ \mathrm{erg/cm^2} \qquad \text{entire } 2223\,\mathrm{s} \tag{36}$$

Using Markus' image cleaning, the integral limits go down by 5–10% in general.

Image Cleaning Method	Differential Flux Upper Limits - PROMPT EMISSION						
	Mean Energy E_0 (GeV)	$\alpha = 1$	$\alpha = 2$	$\alpha = 2.25$	$\alpha = 2.5$	$\alpha = 3$	$E_b = 200$
		$d\Phi/dE$ 10^{-18} $\mathrm{cm^{-2}keV^{-1}s^{-1}}$	$d\Phi/dE$ 10^{-18} $\mathrm{cm^{-2}keV^{-1}s^{-1}}$	$d\Phi/dE$ 10^{-18} $\mathrm{cm^{-2}keV^{-1}s^{-1}}$	$d\Phi/dE$ 10^{-18} $\mathrm{cm^{-2}keV^{-1}s^{-1}}$	$d\Phi/dE$ 10^{-18} $\mathrm{cm^{-2}keV^{-1}s^{-1}}$	$d\Phi/dE$ 10^{-18} $\mathrm{cm^{-2}keV^{-1}s^{-1}}$
Abs. 7 4 (PSF= $0.05°\sigma$)	173	8.5	9.9	10.	10.	10.	9.1
	288	0.9	1.1	1.1	1.1	1.1	1.1
Abs. 7 4 (PSF= $0.07°\sigma$)	184	8.9	9.4	9.4	9.3	9.0	9.4
	289	0.8	0.9	0.9	0.9	0.9	1.0
Nepomuk (PSF= $0.05°\sigma$)	150	9.2	11.	11.	11.	11.	9.5
	279	1.6	1.8	1.8	1.9	1.8	1.9
Nepomuk (PSF= $0.07°\sigma$)	152	6.4	6.7	6.6	6.5	6.0	6.7
	281	1.2	1.3	1.3	1.3	1.3	1.4
Markus (PSF= $0.05°\sigma$)	161	6.7	7.7	7.9	7.9	7.9	7.0
	283	1.0	1.2	1.2	1.2	1.2	1.2
Markus (PSF= $0.07°\sigma$)	165	5.2	5.8	5.9	5.9	5.8	5.5
	288	1.0	1.1	1.1	1.1	1.1	1.2

Table 10: Differential upper limits obtained with the $ALPHA$-analysis for the GRB050713a prompt emission data, using the later runs as OFF-data. The variable α denotes the (unknown) incident gammas spectral index and E_b the break energy for the exponential cut-off spectrum.

Image Cleaning Method	Mean Energy E_0 (GeV)	Differential Flux Upper Limits - FIRST 1000 SECONDS					
		$\alpha = 1$	$\alpha = 2$	$\alpha = 2.25$	$\alpha = 2.5$	$\alpha = 3$	$E_b = 200$
		$d\Phi/dE$ 10^{-18} $\mathrm{cm^{-2}keV^{-1}s^{-1}}$	$d\Phi/dE$ 10^{-18} $\mathrm{cm^{-2}keV^{-1}s^{-1}}$	$d\Phi/dE$ 10^{-18} $\mathrm{cm^{-2}keV^{-1}s^{-1}}$	$d\Phi/dE$ 10^{-18} $\mathrm{cm^{-2}keV^{-1}s^{-1}}$	$d\Phi/dE$ 10^{-18} $\mathrm{cm^{-2}keV^{-1}s^{-1}}$	$d\Phi/dE$ 10^{-18} $\mathrm{cm^{-2}keV^{-1}s^{-1}}$
Abs. 7 4 (PSF= $0.05°\sigma$)	173	4.1	4.7	4.8	4.8	4.8	4.3
	286	0.40	0.48	0.50	0.50	0.50	0.51
Abs. 7 4 (PSF= $0.07°\sigma$)	184	4.0	4.2	4.2	4.2	4.0	4.2
	289	0.34	0.39	0.39	0.39	0.38	0.41
Nepomuk (PSF= $0.05°\sigma$)	149	2.8	3.3	3.4	3.4	3.4	2.9
	278	0.53	0.62	0.63	0.64	0.64	0.65
Nepomuk (PSF= $0.07°\sigma$)	152	2.7	2.9	2.8	2.8	2.6	2.8
	281	0.43	0.48	0.48	0.48	0.47	0.50
Markus (PSF= $0.05°\sigma$)	161	2.5	2.9	2.9	3.0	3.0	2.6
	282	0.37	0.44	0.45	0.46	0.46	0.46
Markus (PSF= $0.07°\sigma$)	165	1.9	2.1	2.1	2.1	2.1	2.0
	287	0.35	0.40	0.40	0.40	0.39	0.42

Table 11: Differential upper limits obtained with the *ALPHA*-analysis for first 1000 s of GRB050713a data, using the later runs as OFF-data. The variable α denotes the (unknown) incident gammas spectral index and E_b the break energy for the exponential cut-off spectrum.

Image Cleaning Method	Differential Flux Upper Limits - TOTAL SAMPLE						
	Mean Energy E_0 (GeV)	$\alpha = 1$	$\alpha = 2$	$\alpha = 2.25$	$\alpha = 2.5$	$\alpha = 3$	$E_b = 200$
		$d\Phi/dE$ 10^{-18} $\mathrm{cm^{-2}keV^{-1}s^{-1}}$	$d\Phi/dE$ 10^{-18} $\mathrm{cm^{-2}keV^{-1}s^{-1}}$	$d\Phi/dE$ 10^{-18} $\mathrm{cm^{-2}keV^{-1}s^{-1}}$	$d\Phi/dE$ 10^{-18} $\mathrm{cm^{-2}keV^{-1}s^{-1}}$	$d\Phi/dE$ 10^{-18} $\mathrm{cm^{-2}keV^{-1}s^{-1}}$	$d\Phi/dE$ 10^{-18} $\mathrm{cm^{-2}keV^{-1}s^{-1}}$
Abs. 7 4 (PSF= $0.05°\sigma$)	173	1.9	2.2	2.3	2.3	2.3	2.0
	330	0.20	0.23	0.24	0.24	0.25	0.25
Abs. 7 4 (PSF= $0.07°\sigma$)	182	2.0	2.1	2.1	2.1	2.0	2.1
	311	0.21	0.24	0.24	0.24	0.24	0.25
Nepomuk (PSF= $0.05°\sigma$)	149	2.1	2.4	2.4	2.5	2.5	2.1
	287	0.37	0.43	0.44	0.45	0.45	0.46
Nepomuk (PSF= $0.07°\sigma$)	152	1.2	1.2	1.2	1.1	1.1	1.2
	281	0.45	0.50	0.51	0.51	0.50	0.53
Markus (PSF= $0.05°\sigma$)	162	1.4	1.6	1.6	1.6	1.6	1.5
	318	0.17	0.20	0.21	0.21	0.21	0.21
Markus (PSF= $0.07°\sigma$)	165	1.2	1.3	1.4	1.4	1.4	1.2
	299	0.20	0.22	0.22	0.22	0.22	0.24

Table 12: Differential upper limits obtained with the *ALPHA*-analysis for the total 2223 s of GRB050713a data, using the OFF data taken two nights later. The variable α denotes the (unknown) incident gammas spectral index and E_b the break energy for the exponential cut-off spectrum.

Image Cleaning Method	Integral Fluence Upper Limits - PROMPT EMISSION					
	Energy Range Energy (GeV)	$\alpha = 1$	$\alpha = 2$	$\alpha = 2.25$	$\alpha = 2.5$	$\alpha = 3$
		Φ (10^{-8}) $\mathrm{erg\,cm^{-2}}$	Φ (10^{-8}) $\mathrm{erg\,cm^{-2}}$	Φ (10^{-8}) $\mathrm{erg\,cm^{-2}}$	Φ (10^{-8}) $\mathrm{erg\,cm^{-2}}$	Φ (10^{-8}) $\mathrm{erg\,cm^{-2}}$
Abs. 7 4	110 - 550	7.1	6.2	6.1	6.0	5.9
(PSF= $0.05°\sigma$)	160 - 800	1.8	1.8	1.8	1.8	2.0
Abs. 7 4	100 - 410	6.4	6.1	6.1	6.1	6.2
(PSF= $0.07°\sigma$)	140 - 800	1.7	1.7	1.8	1.8	2.0
Nepomuk	80 - 550	7.0	5.9	5.8	5.8	5.9
(PSF= $0.05°\sigma$)	160 - 700	2.6	2.6	2.7	2.7	2.9
Nepomuk	70 - 470	4.7	4.2	4.2	4.2	4.3
(PSF= $0.07°\sigma$)	160 - 700	2.0	2.0	2.0	2.0	2.1
Markus	90 - 470	4.6	4.2	4.2	4.2	4.2
(PSF= $0.05°\sigma$)	160 - 700	1.7	1.7	1.8	1.8	1.9
Markus	90 - 470	3.9	3.4	3.4	3.4	3.4
(PSF= $0.07°\sigma$)	160 - 700	1.7	1.8	1.8	1.8	1.9

Table 13: Integral upper Limits obtained with the $ALPHA$-analysis for the GRB050713a prompt emission data, using the later runs as OFF-data. The variable α denotes the (unkown) incident gammas spectral index.

Image Cleaning Method	Integral Fluence Upper Limits - FIRST 1000 SECONDS					
	Energy Range Energy (GeV)	$\alpha = 1$	$\alpha = 2$	$\alpha = 2.25$	$\alpha = 2.5$	$\alpha = 3$
		Φ (10^{-8}) erg cm^{-2}	Φ (10^{-8}) erg cm^{-2}	Φ (10^{-8}) erg cm^{-2}	Φ (10^{-8}) erg cm^{-2}	Φ (10^{-8}) erg cm^{-2}
Abs. 7 4	110 - 550	36.	32.	31.	31.	30.
(PSF= $0.05°\sigma$)	160 - 800	8.4	8.4	8.5	8.7	9.2
Abs. 7 4	110 - 410	31.	30.	30.	30.	30.
(PSF= $0.07°\sigma$)	140 - 800	7.7	7.7	7.9	8.1	8.8
Nepomuk	80 - 550	23.	19.	19.	19.	19.
(PSF= $0.05°\sigma$)	160 - 700	9.5	9.7	9.8	10.	10.
Nepomuk	70 - 480	21.	19.	19.	19.	20.
(PSF= $0.07°\sigma$)	160 - 700	8.1	7.9	8.0	8.0	8.3
Markus	90 - 480	19.	17.	17.	17.	17.
(PSF= $0.05°\sigma$)	160 - 700	6.8	7.0	7.2	7.3	7.8
Markus	90 - 480	15.	13.	13.	13.	13.
(PSF= $0.07°\sigma$)	160 - 700	6.8	6.8	6.9	7.0	7.3

Table 14: Integral upper limits obtained with the *ALPHA*-analysis for first 1000 s of GRB050713a data, using the later runs as OFF-data. The variable α denotes the (unkown) incident gammas spectral index.

Image Cleaning Method	Integral Fluence Upper Limits - TOTAL SAMPLE					
	Energy Range Energy (GeV)	$\alpha = 1$	$\alpha = 2$	$\alpha = 2.25$	$\alpha = 2.5$	$\alpha = 3$
		Φ (10^{-8}) erg cm^{-2}	Φ (10^{-8}) erg cm^{-2}	Φ (10^{-8}) erg cm^{-2}	Φ (10^{-8}) erg cm^{-2}	Φ (10^{-8}) erg cm^{-2}
Abs. 7 4	110 - 550	38.	33.	33.	32.	32.
(PSF= $0.05°\sigma$)	160 - 800	7.6	7.6	7.7	7.9	8.3
Abs. 7 4	110 - 410	33.	31.	31.	31.	31.
(PSF= $0.07°\sigma$)	140 - 800	8.1	8.1	8.3	8.5	9.2
Nepomuk	80 - 550	30.	25.	24.	24.	25.
(PSF= $0.05°\sigma$)	160 - 700	16.	16.	17.	17.	18.
Nepomuk	70 - 480	18.	16.	16.	16.	17.
(PSF= $0.07°\sigma$)	160 - 700	19.	18.	18.	19.	19.
Markus	90 - 480	20.	18.	19.	18.	18.
(PSF= $0.05°\sigma$)	160 - 700	5.6	5.8	5.9	6.0	6.4
Markus	90 - 480	15.	13.	13.	13.	13.
(PSF= $0.07°\sigma$)	160 - 700	7.6	7.7	7.8	7.9	8.3

Table 15: Integral upper limits obtained with the *ALPHA*-analysis for the total 2223 s of GRB050713a data, using the OFF data taken two nights later. The variable α denotes the (unkown) incident gammas spectral index.

9.6 Search in time slices of 100 seconds

An additional search for peak emission in steps of 100 seconds was performed. To do so, the entire GRB050713a data sample was divided into 22 slices of equal time duration (exactly 101 seconds). Table 16 lists the used parameters for the peak emission search. Only Nepomuk's and Markus' image cleanings were used, every of the 22 time slices was taken as ON data while the remaining data set was used as OFF data. A second search was performed shifting the phase of the time slice by 50 seconds.

Figures 65 to 68 show the distribution of obtained significances, with and without phase shift and with Nepomuk's and Markus' image cleaning, respectively. Moreover, the number of excess events are distributed in general randomly over time, as can be seen in figures 69 and 72. One significant excess of $4.3\,\sigma$ was observed (figures 66 and 70 bottom left). Figure 70 shows the corresponding distribution of $ALPHA$ which shows that the majority of the events causing the excess occur in a bin around $ALPHA = 25$. This and the fact that the probability for an excess of $4.3\,\sigma$ due to statistical fluctuations to occur within of 176 trials is still an acceptable 10%, we believe that this excess is not due an emission from GRB050713a. Note that the small excess in rate, found in figure 47 with Markus' image cleaning and a $HADRONNESS$-cut, trained with a simulated PSF of $0.07°\sigma$, is not found back in these plots. We therefore assume that the assumption of no signal still holds.

From the absence of a signal in the peak emission search, a global upper limit can be derived from the time slice yielding the biggest number of excess events:

$$< \frac{d\Phi}{dE} >|_{150\,\mathrm{GeV}} \quad < \quad 1.5 \cdot 10^{-17}\ \mathrm{ph/cm^2/keV/s} \qquad \text{any } 100\,\mathrm{s} \text{ interval} \tag{37}$$

$$< \frac{d\Phi}{dE} >|_{280\,\mathrm{GeV}} \quad < \quad 4.0 \cdot 10^{-18}\ \mathrm{ph/cm^2/keV/s} \qquad \text{any } 100\,\mathrm{s} \text{ inverval} \tag{38}$$

Image Cleaning Method	Reconst. Energy Range (GeV)	cut hadr.-ness	cut alpha (°)	Mean E_γ MC (GeV)	Mean Coll. Area (10^8 cm^2)
Nepomuk (PSF= $0.05°\sigma$)	100 - 200	0.55	26	150	2.2
	200 - 500	0.48	19	279	4.8
Nepomuk (PSF= $0.07°\sigma$)	100 - 200	0.29	29	152	1.4
	200 - 500	0.39	21	281	4.8

Table 16: Results of the $ALPHA$-analysis for the GRB050713a 100 seconds time slices search, using all ON data except that slice as OFF-data.

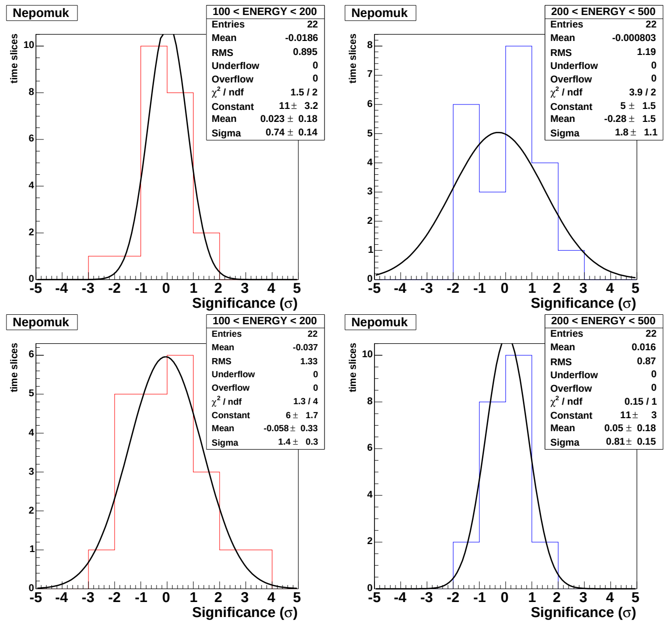

Figure 65: Distributions of the obtained significances during the peak search, obtained with the Nepomuk's time image cleaning. The four plots correspond to two slices of the $ENERGY$ parameters: Left: 100 to 200 GeV and right: 200 to 500 GeV reconstructed energy. Top: with cuts optimized using $PSF = 0.05°\sigma$, bottom: using $PSF = 0.07°\sigma$.

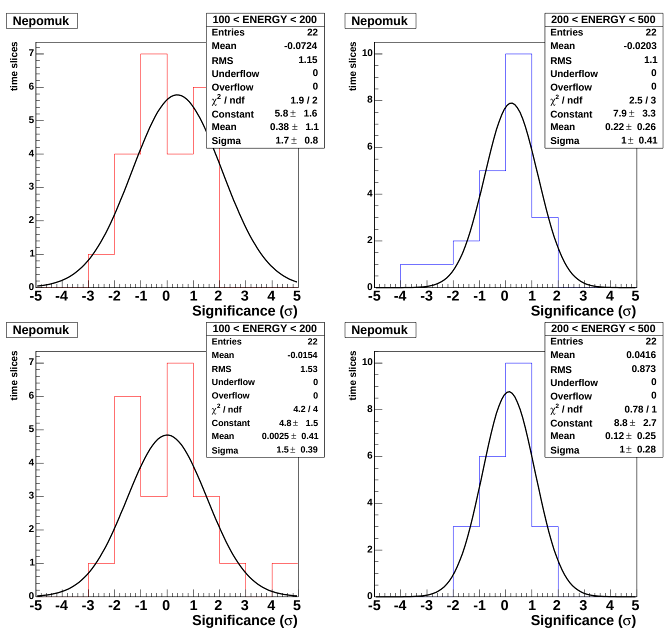

Figure 66: Distributions of the obtained significances during the peak search, times shifted by half a period. The data was cleaned with Nepomuk's time image cleaning. The four plots correspond to two slices of the $ENERGY$ parameters: Left: 100 to 200 GeV and right: 200 to 500 GeV reconstructed energy. Top: with cuts optimized using $PSF = 0.05°\sigma$, bottom: using $PSF = 0.07°\sigma$.

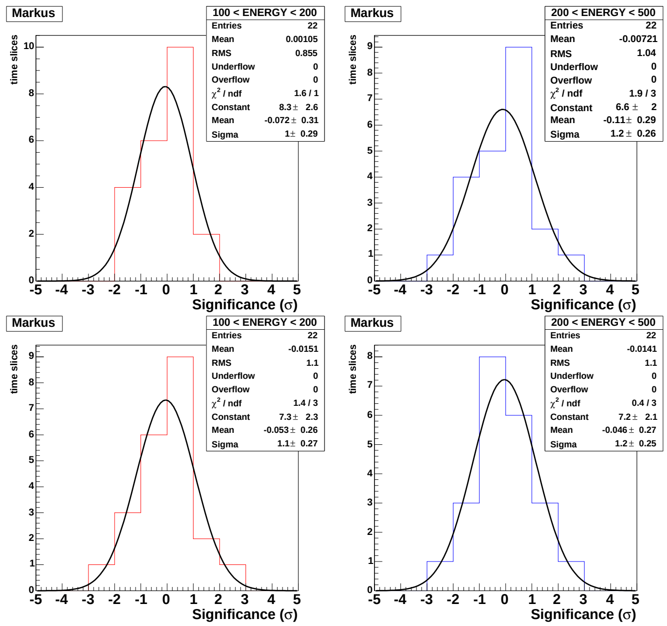

Figure 67: Distributions of the obtained significances during the peak search, obtained with the Markus' image cleaning. The four plots correspond to two slices of the $ENERGY$ parameters: Left: 100 to 200 GeV and right: 200 to 500 GeV reconstructed energy. Top: with cuts optimized using $PSF = 0.05°\sigma$, bottom: using $PSF = 0.07°\sigma$.

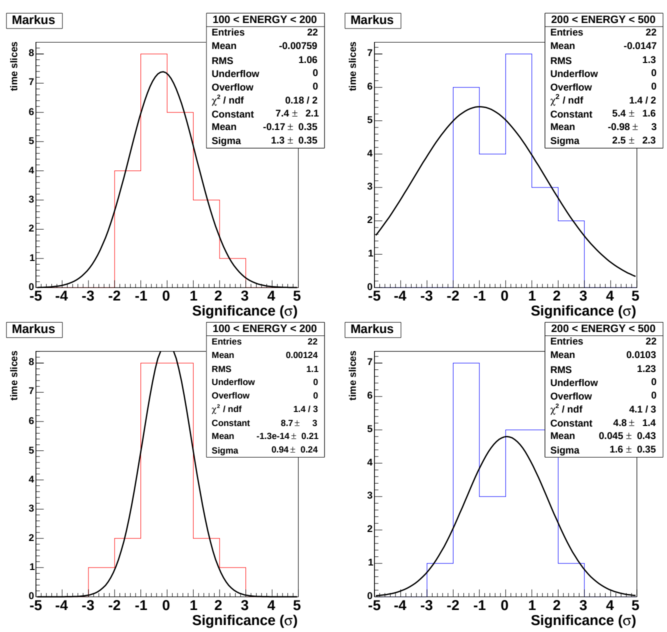

Figure 68: Distributions of the obtained significances during the peak search, times shifted by half a period. The data was cleaned with Markus' image cleaning. The four plots correspond to two slices of the $ENERGY$ parameters: Left: 100 to 200 GeV and right: 200 to 500 GeV reconstructed energy. Top: with cuts optimized using $PSF = 0.05°\sigma$, bottom: using $PSF = 0.07°\sigma$.

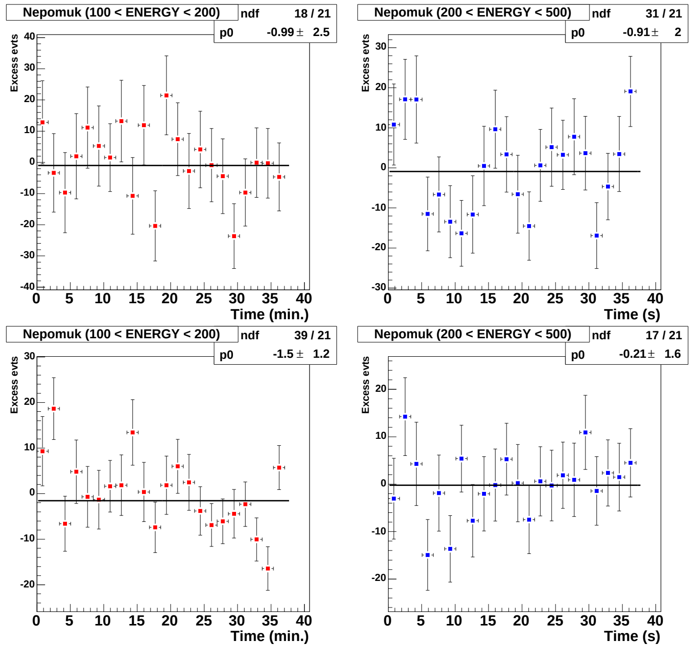

Figure 69: Number of excess events vs. time for the peak search, obtained with the Nepomuk's time image cleaning. The four plots correspond to two slices of the $ENERGY$ parameters: Left: 100 to 200 GeV and right: 200 to 500 GeV reconstructed energy. Top: with cuts optimized using $PSF = 0.05°\sigma$, bottom: using $PSF = 0.07°\sigma$..

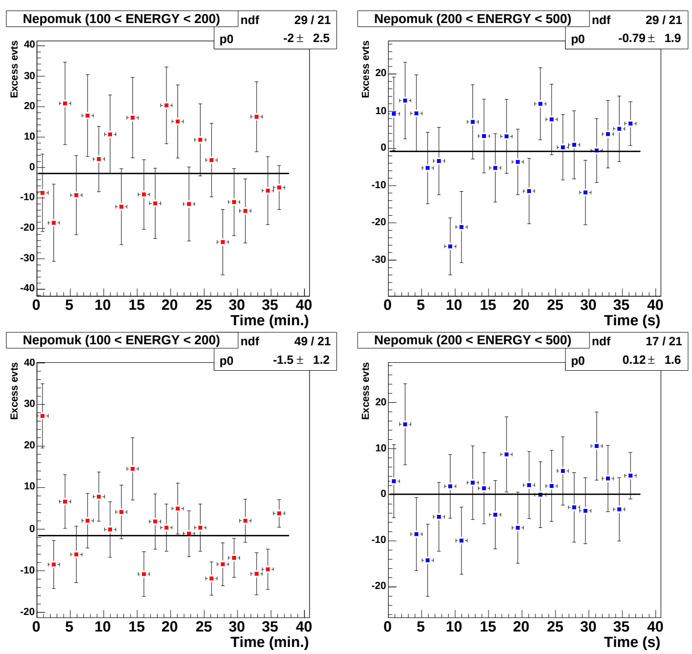

Figure 70: Number of excess events vs. time for the peak search, times shifted by half a period. The data was cleaned with Nepomuk's image cleaning. The four plots correspond to two slices of the $ENERGY$ parameters: Left: 100 to 200 GeV and right: 200 to 500 GeV reconstructed energy. Top: with cuts optimized using $PSF = 0.05°\sigma$, bottom: using $PSF = 0.07°\sigma$.

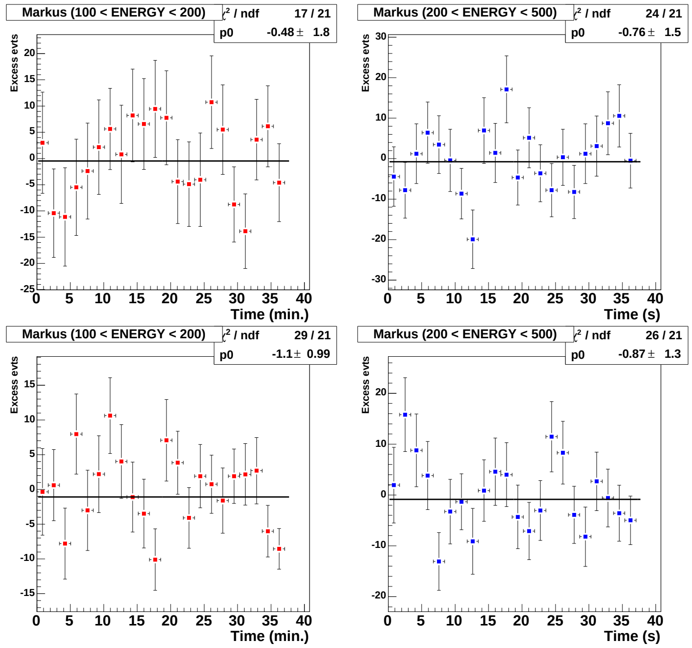

Figure 71: Number of excess events vs. time for the peak search, obtained with the Markus's time image cleaning. The four plots correspond to two slices of the $ENERGY$ parameters: Left: 100 to 200 GeV and right: 200 to 500 GeV reconstructed energy. Top: with cuts optimized using $PSF = 0.05°\sigma$, bottom: using $PSF = 0.07°\sigma$..

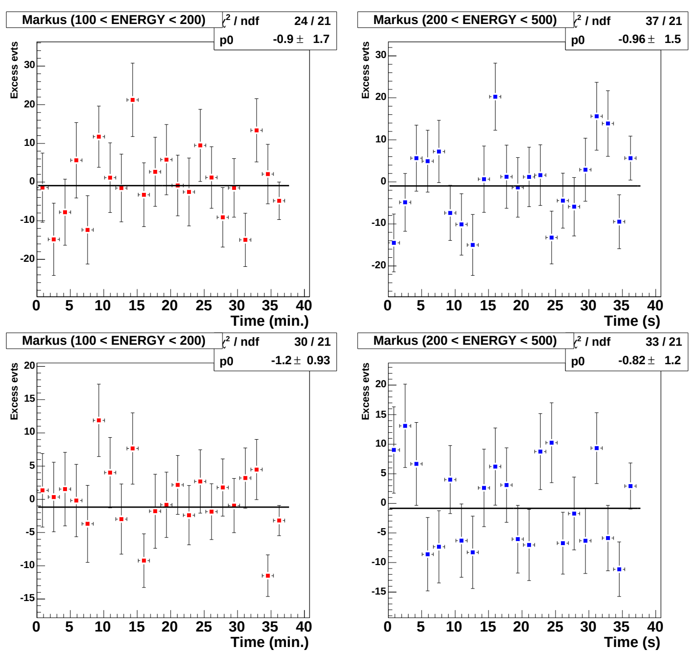

Figure 72: Number of excess events vs. time for the peak search, times shifted by half a period. The data was cleaned with Markus' image cleaning. The four plots correspond to two slices of the $ENERGY$ parameters: Left: 100 to 200 GeV and right: 200 to 500 GeV reconstructed energy. Top: with cuts optimized using $PSF = 0.05°\sigma$, bottom: using $PSF = 0.07°\sigma$.

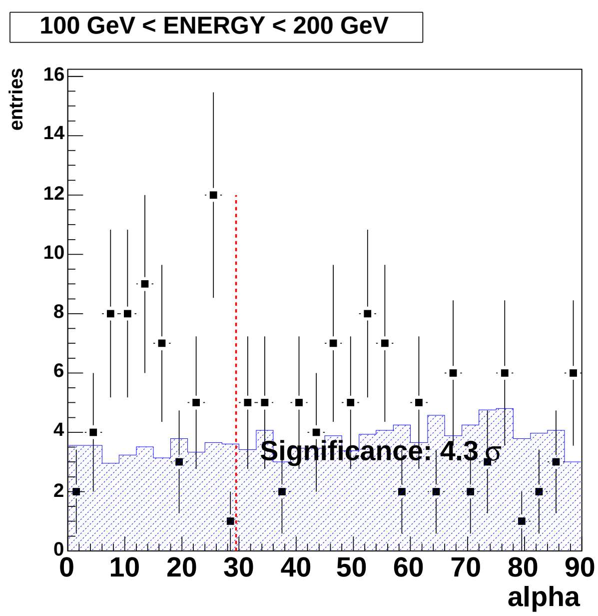

Figure 73: Distribution of $ALPHA$ for the time slice which obtained the largest significance. (Nepomuk's image cleaning, $PSF = 0.07°\sigma$ used for Gamma simulation.

9.7 Effect of systematic uncertainties on the limits

Two major systematic uncertainties have to be added to this limit:

1. Inefficiencies in the camera due to trigger inefficiencies.

2. Uncertainties in the absolute calibration.

Figure 74 shows the center of gravity with all cuts applied for the entire set of GRB050713a data, with Nepomuk's image cleaning applied. One can see that the lower energy bin seems to exhibit voids at the right side of the camera and the lower left part. These voids coincide with the one already seen in chapter 7 and we suspect that they come from trigger inefficiencies in parts of the camera.

In order to quantify the effect, the azimuthal projection of the center of gravity was inspected and the relative deficit of the two bins corresponding to the two voids calculated. Figures 75 show such examples. In none of the investigated cuts and data samples, the deficit exceeded 10%. For this reason, we apply a systematic increase of 10% to all derived upper limits to account for this effect.

Concerning the uncertainty in the absolute calibration, a first look at the "Blind Pixel" and the "PIN Diode" calibrations give indications that we over-estimate our total efficiency by about 10%. We include this systematic uncertainty by raising the upper limit by another 10%.

In total, all upper limits are thus raised by 20% to include the systematic uncertainties which we could detect so far.

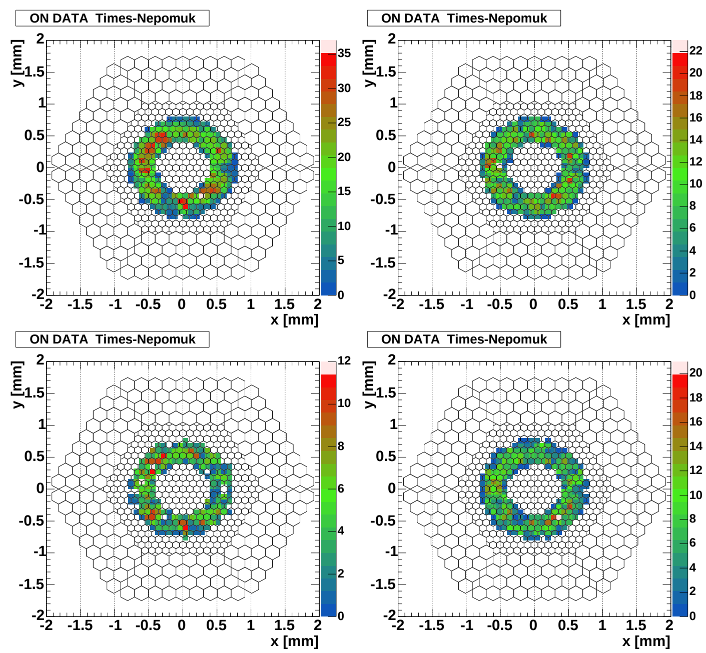

Figure 74: Distributions of the center of gravity, obtained with the Nepomuk's time image cleaning and the cuts derived for the entire sample of GRB050713a. The four plots correspond to two slices of the *ENERGY* parameters: Left: 100 to 200 GeV and right: 200 to 500 GeV reconstructed energy. Top: with cuts optimized using $PSF = 0.05°\sigma$, bottom: using $PSF = 0.07°\sigma$.

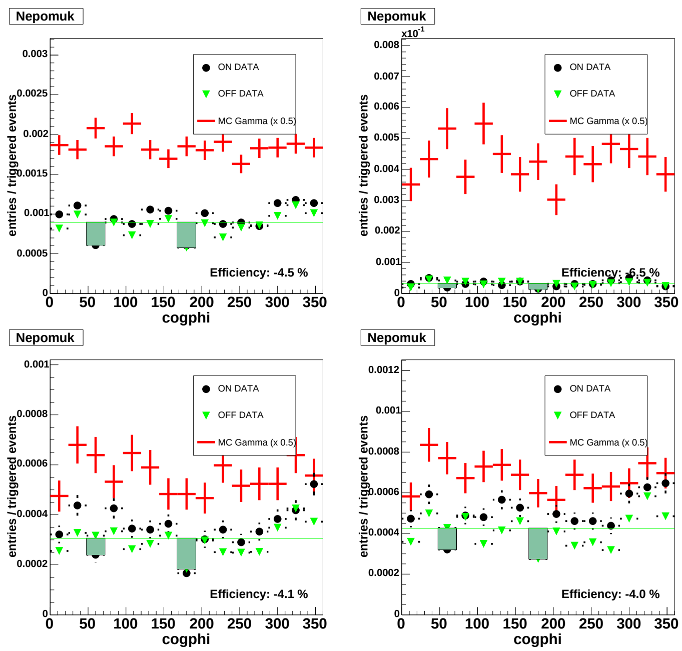

Figure 75: Azimuthal projections of the center of gravity, obtained with the Nepomuk's time image cleaning and the cuts derived for the entire sample of GRB050713a. The four plots correspond to two slices of the *ENERGY* parameters: Left: 100 to 200 GeV and right: 200 to 500 GeV reconstructed energy. Top: with cuts optimized using $PSF = 0.05°\sigma$, bottom: using $PSF = 0.07°\sigma$.

10 Disp Analysis

At the beginning of the *DISP*-analysis, two cuts were re-inforced with respect to the values set in the previous analysis step:

$$ISLANDS < 2 \tag{39}$$
$$LEAKAGE < 0.005 \tag{40}$$

These are the same cuts, as already applied in the *ALPHA*-analysis (chapter 9) and are not explained in more detail here. As in the case of the *ALPHA*-analysis, these cuts will be moved to the pre-cuts in the future.

No further cut is applied on the *DIST* parameter, unlike in the *ALPHA*-analysis, mainly because a further cut on *DIST* would make the θ^2 distributions even steeper towards low values of θ^2.

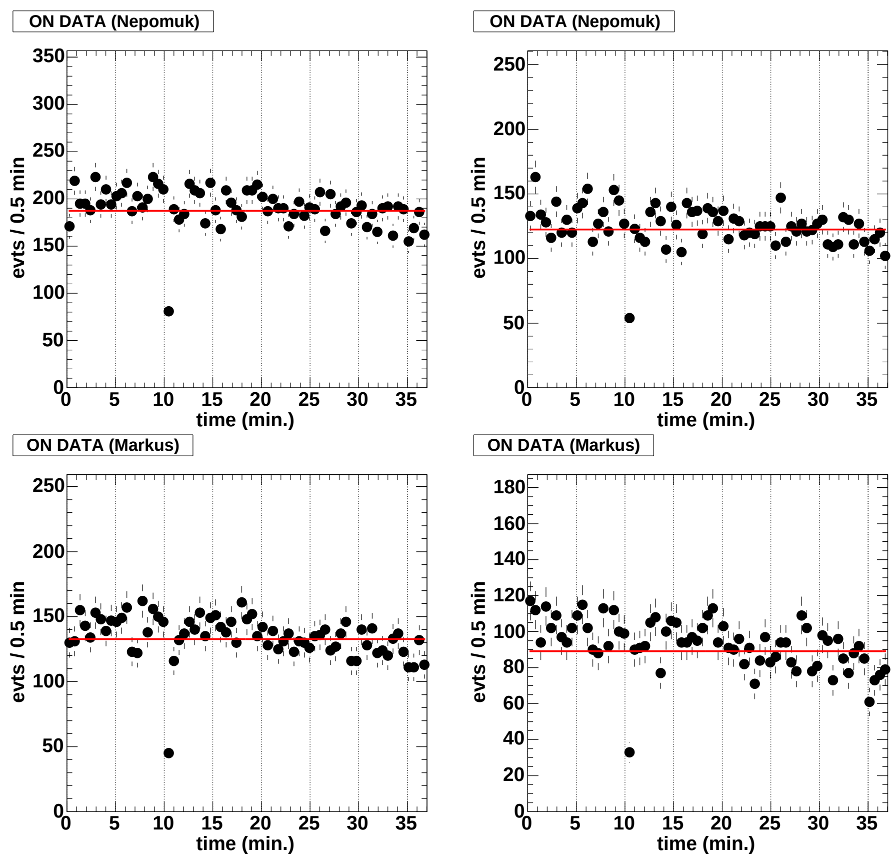

Figure 76: Event rates after very loose cuts on $HADRONNESS$ and $THETA^2$, shown in bins of 30 seconds. Top: Nepomuk's image cleaning, bottom: Markus's image cleaning. On the left side, the $HADRONNESS$ has been trained using simulated gamma showers and a PSF of $0.05°\sigma$, on the right side a PSF of $0.07°\sigma$ was used. All four distributions were fitted to a straight line from after the drop at $T = 10.5$ min. to the end. The fit result is shown as red line (and drawn from $T = 0$ on).

With the resulting sample and very loose cuts on $HADRONNESS < 0.8$ and $THETA^2 < 0.1$, we plotted the rates, as shown in figure 76. One can observe a global decrease in event rate for both shown image cleanings and used point-spread functions to train the $HADRONNESS$. Additionally, the drop in event rate at $T \approx 10.5$ min. can be seen in all four plots which was due to a stop of data taking. Only the last plot, obtained with Markus' image cleaning and a PSF of $0.07°\sigma$ shows two more evident features: A drop at the beginning of the observation and another rise between 15 and 20 minutes. These two features were already found in the event rate plot of the $ALPHA$-analysis (figure 47), but again not found back in the later analysis.

Furthermore, the analysis was split into the following bins of reconstructed energy ($ENERGY$). For the Mrk501 data, the following bins were chosen:

1. 45 GeV $<$ $ENERGY$ $<$ 75 GeV
2. 60 GeV $<$ $ENERGY$ $<$ 100 GeV
3. 100 GeV $<$ $ENERGY$ $<$ 150 GeV
4. 150 GeV $<$ $ENERGY$ $<$ 300 GeV

Bins nr. 2–4 correspond to consecutive energy bins containing more or less the same number of events while bin nr. 1 is an attempt to push the energy limit to the absolute minimum.

The GRB050713a data was analysed in two bins:

1. 100 GeV $<$ $ENERGY$ $<$ 200 GeV
2. 200 GeV $<$ $ENERGY$ $<$ 500 GeV

Above 500 GeV, no event survived the $SIZE$ cut of the previous data reduction step.

Figures 77 show the distributions of the parameter $HADRONNESS$ for the GRB050713a data, obtained with the different image cleaning algorithms. One can see a rather good agreement between all ON and OFF data. Moreover, the algorithms using the time information seem to yield a better separability of the gamma- and hadron-samples.

Like in the case of the $ALPHA$-analysis, the best suited cut on $HADRONESS$ was searched calculating the significance of the excess events in the signal region versus the remaining background for different cut values on $HADRONNESS$. Here, special care had to be taken with the MC events reconstructed out of the signal region because the "ghost-busting" had swapped the pointing direction of the cascade. In order to estimate the number of excess events correctly, an additional cut was introduced during this procedure:

$$THETA^2 < 0.6 \tag{41}$$

Then, the procedure could continue like shown in the $ALPHA$-analysis chapter: First fit the distribution of excess events over background in a θ^2 plot, obtained from MC and OFF-data to a Gaussian. Then determine the signal region, defined as:

$$SIGNAL\ REGION = [0, 2.5\sigma] \tag{42}$$

Finally, scan through the number of events left after a given cut on $HADRONNESS$ and calculate the significance using the number of remaining MC events as "excess events" and the normalized OFF-data.

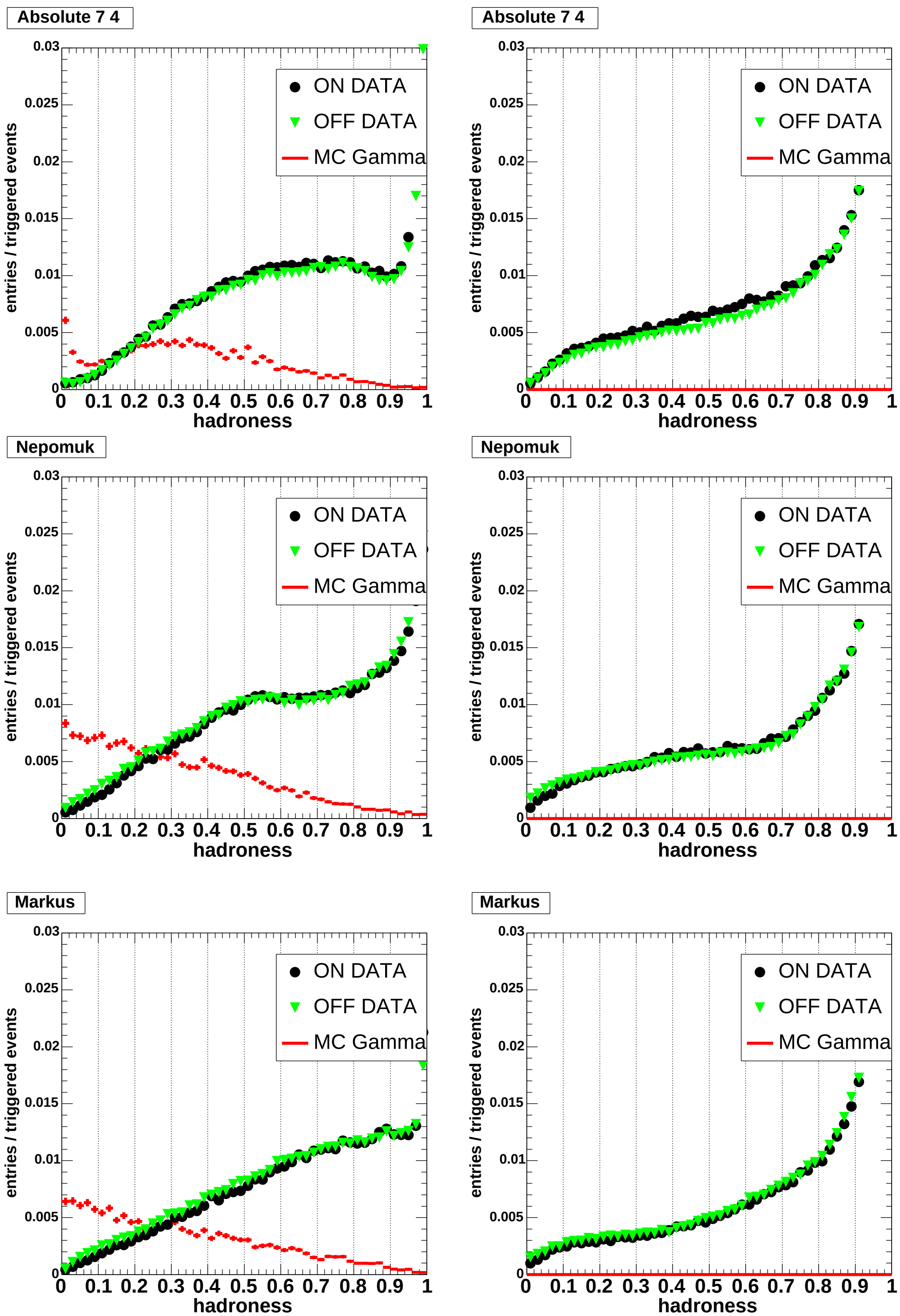

Figure 77: Distributions of the parameter $HADRONESS$ for the various image cleaning algorithms and the GRB050713a data. Top: absolute cleaning with levels 7 and 4 photo-electrons, center: Nepomuk's image cleaning using time coincidence, bottom: Markus image cleaning using time coincidence. On the left side, the Random Forest was trained with the simulated gamma showers and the better PSF ($0.05°\sigma$), one the right side the worse PSF was used ($0.07°\sigma$).

10.1 Results Mrk501 Data

Figures 79 through 81 show the resulting θ^2-plots in the different bins of reconstructed energy ("$ENERGY$") with the calculated significances (Li&Ma, form. 17) using ON and OFF-data. Figure 82 shows the distribution of the $DISP$ parameter projected into the MAGIC camera, with the signal excesses visible in the camera center or slightly off at the lowest energies. One can also see a large void in the lowest energy bin right below the camera center. Table 17 lists the parameters and results obtained from the $DISP$-analysis for the Mrk501 data. At energies above 100 GeV, the different image cleaning algorithms yield equivalent results. Below 100 GeV, the image cleaning algorithms using times yield better results, however less significant than the ones obtained with the $ALPHA$-analysis.

Figure 78 shows the distribution of the simulated gamma shower energies for the four bins in reconstructed energy, exemplary for Nepomuk's image cleaning. One can see that a mean energy of 78 GeV is obtained in the second lowest energy bin, marginally detected with $3.9\,\sigma$. Although the thresholds are very much comparable to the ones obtained with the $ALPHA$-analysis, the significances are clearly worse, also the effective areas are about 20% lower. The reason for this result is not yet understood, it may have to do with the observed fact that the "ghost-busting" does not work any more at all at these energies and therefore half of the signal is lost because reconstructed at very high values of θ^2. These events are reconstructed at low values of the $ALPHA$ parameter, though, and therefore recovered in the $ALPHA$-analysis.

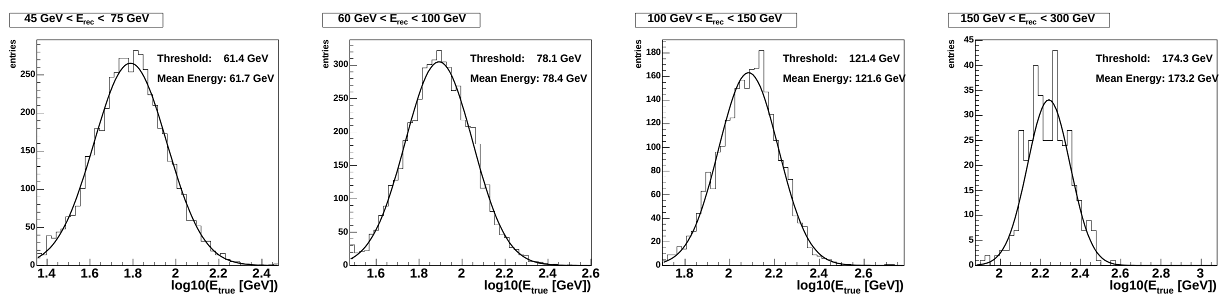

Figure 78: Distributions of the simulated MC energy for the Mrk501 data, obtained with Nepomuk's image cleaning and all cuts applied. The four plots correspond to 4 slices of the $ENERGY$ parameters: 45 to 75, 60 to 100, 100 to 150 and 150 to 300 GeV reconstructed energy.

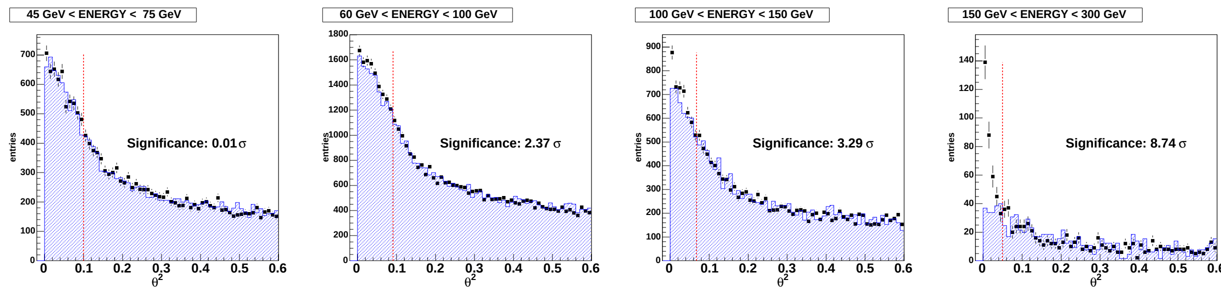

Figure 79: Distributions of the parameter θ^2 for the Mrk501 data, obtained with the absolute image cleaning using 7 and 4 photo-electrons. The four plots correspond to 4 slices of the $ENERGY$ parameters: 45 to 75, 60 to 100, 100 to 150 and 150 to 300 GeV reconstructed energy.

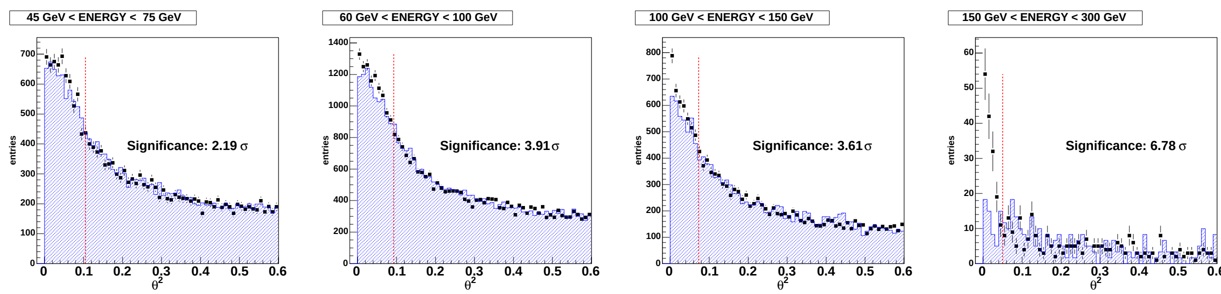

Figure 80: Distributions of the parameter θ^2 for the Mrk501 data, obtained with the Nepomuk's time image cleaning. The four plots correspond to 4 slices of the $ENERGY$ parameters: 45 to 75, 60 to 100, 100 to 150 and 150 to 300 GeV reconstructed energy.

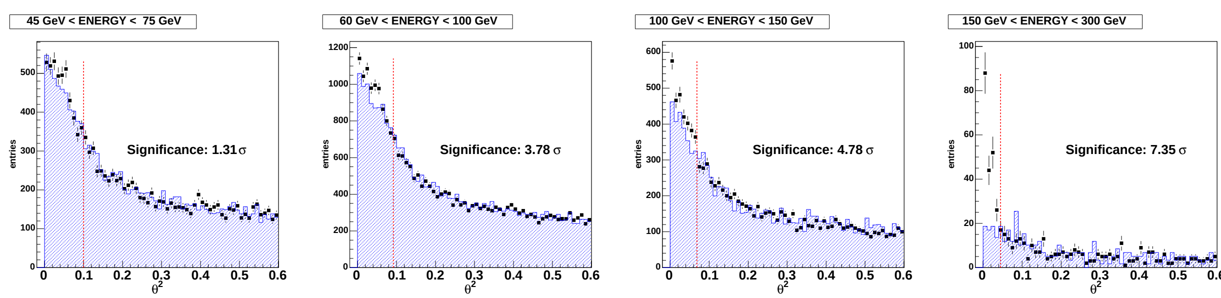

Figure 81: Distributions of the parameter θ^2 for the Mrk501 data, obtained with the Markus's time image cleaning. The four plots correspond to 4 slices of the $ENERGY$ parameters: 45 to 75, 60 to 100, 100 to 150 and 150 to 300 GeV reconstructed energy.

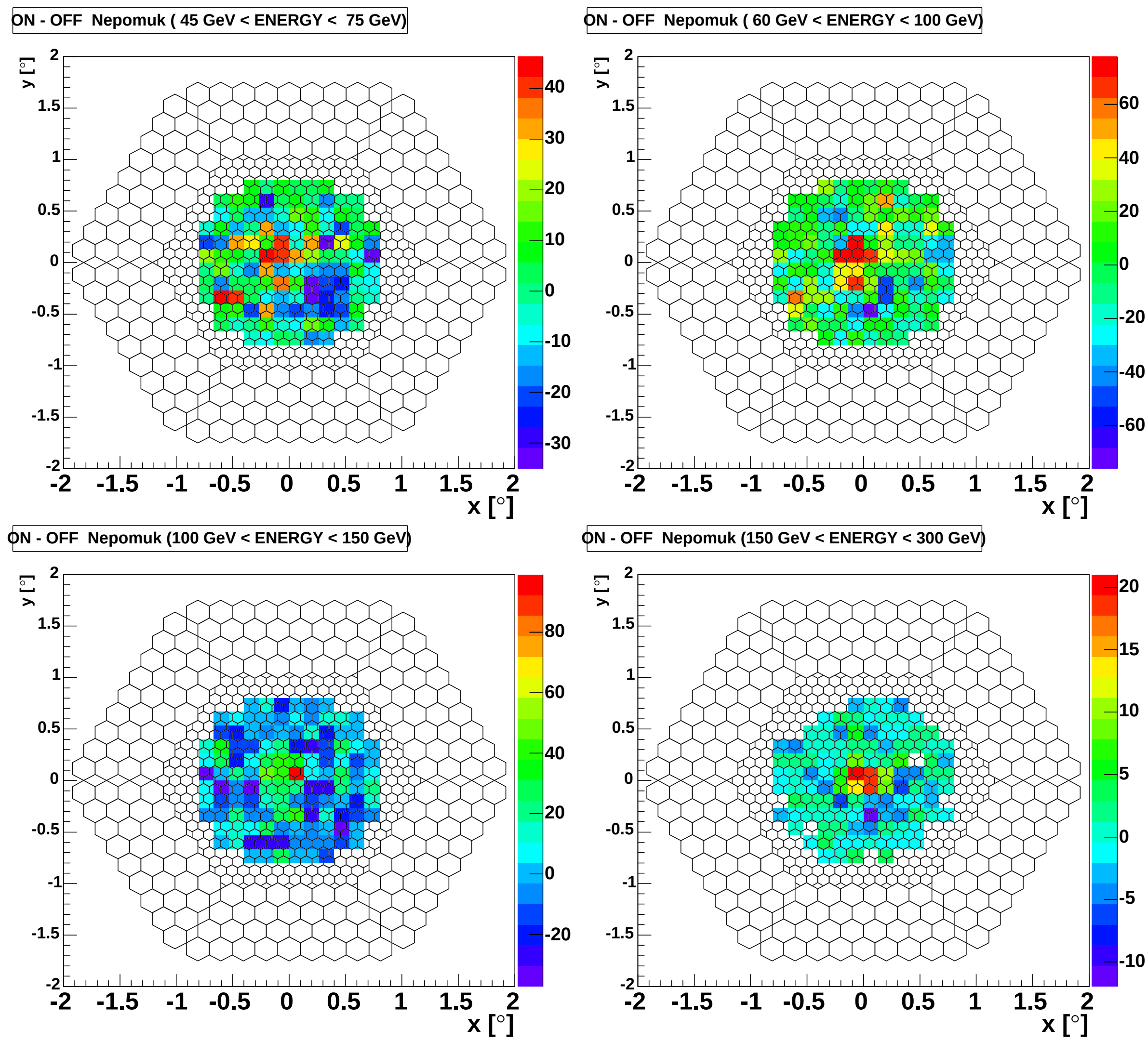

Figure 82: Distributions of the parameter *DISP* for the Mrk501 data, subtracted by normalized OFF data, Nepomuk's time image cleaning. The four plots correspond to 4 slices of the *ENERGY* parameters: 45 to 75, 60 to 100, 100 to 150 and 150 to 300 GeV reconstructed energy.

Image Cleaning Method	Reconst. Energy Range (GeV)	cut $HADR.-NESS$	cut θ^2 (°)	Number Excess Events	Sign. Li Ma	Mean MC Energy (GeV)	Coll. Area at $< E_\gamma >$ 10^8 (cm^2)
Abs. 10 5	45 - 75	0.85	0.11	-18 $\pm$ 76	-0.2	74	0.06
	60 - 100	0.78	0.10	314 $\pm$ 169	1.9	87	0.6
	100 - 150	0.58	0.07	473 $\pm$ 108	4.3	120	1.0
	150 - 300	0.26	0.05	261 $\pm$ 29	8.5	182	1.1
Abs. 7 4	45 - 75	0.73	0.10	1 $\pm$ 100	0.0	70	0.2
	60 - 100	0.69	0.09	385 $\pm$ 162	2.4	82	0.8
	100 - 150	0.58	0.07	316 $\pm$ 96	3.3	120	1.2
	150 - 300	0.20	0.05	221 $\pm$ 24	8.7	179	0.9
Nepomuk	45 - 75	0.57	0.10	229 $\pm$ 105	2.2	62	0.6
	60 - 100	0.61	0.09	552 $\pm$ 141	3.9	78	1.2
	100 - 150	0.57	0.07	345 $\pm$ 95	3.6	122	1.3
	150 - 300	0.16	0.05	111 $\pm$ 15	6.8	173	0.4
Markus	45 - 75	0.63	0.10	120 $\pm$ 91	1.3	67	0.4
	60 - 100	0.62	0.09	491 $\pm$ 130	3.8	79	1.0
	100 - 150	0.52	0.07	366 $\pm$ 76	4.8	121	1.1
	150 - 300	0.26	0.04	142 $\pm$ 18	7.4	177	0.7

Table 17: Results of the $DISP$-analysis for the Mrk501 data.

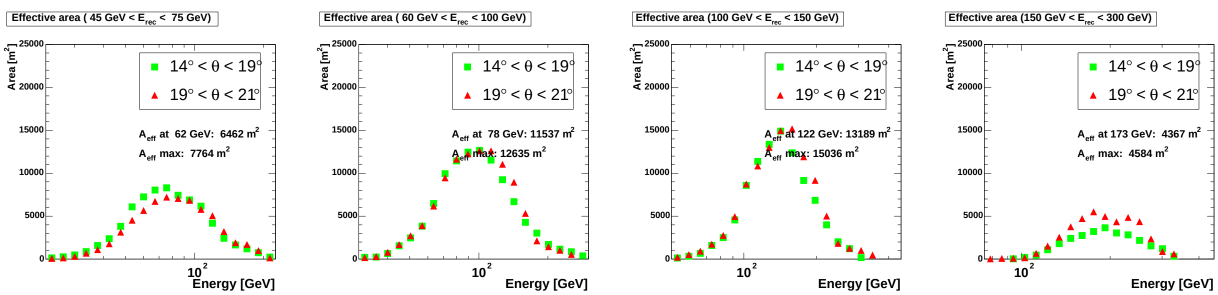

Figure 83: Distributions of the effective area for the Mrk501 data, obtained with the Nepomuk's time image cleaning and all cuts applied. The four plots correspond to 4 slices of the *ENERGY* parameters: 45 to 75, 60 to 100, 100 to 150 and 150 to 300 GeV reconstructed energy.

10.2 Results GRB050713a Data

Because of the smaller sensitivity of the $DISP$ analysis, the GRB050713a data was analyzed only in two ways, in principle to have a result to be used for cross-checks with the $ALPHA$-analysis:

1. Taking the first 90 s of observation which correspond to the prompt emission phases in either the BAT and/or the XRT instrument on SWIFT. The remaining six runs (starting at about 7.7 min after start) as OFF data.
2. Searching in time bins of 100 s ON data, using the data outside the corresponding time bin as OFF data.

Like in the case of the $ALPHA$-analysis, none of these four searches showed a significant excess over background. Upper limits were placed starting from the observed number of excess events and the number of background events in the same "signal" region of the θ^2-distribution. In order to determine the 99% CL upper limit on the number of events in each energy bin, we followed the approach outline in [10].

10.2.1 Prompt emission phase

After determining the cuts on $HADRONNESS$ and θ^2, energy thresholds of 150 GeV (for the lower bin in reconstructed energy) and 280 GeV (for the upper bin) were obtained (see figure 84).

Figure 86 shows the resulting θ^2-plots in the different bins of reconstructed energy ("$ENERGY$") with the calculated significances (Li&Ma, form. 17) using ON and OFF-data and Nepomuk's image cleaning. No signal can be seen in neither of the two energy bins. Also, the distribution of the $DISP$ parameter (figure 85) shows no significant excess in any part of the camera.

The results of the $DISP$-analysis on the prompt emission phase are summarized in table 18. Like in the case of the $ALPHA$-analysis, Nepomuk's algorithm yields the lowest threshold, followed by Markus's one, although the threshold is somewhat higher here (156 GeV vs. 150 GeV in the case of the $ALPHA$-analysis). One can also see that the effective areas are about 20% lower than in the case of the $ALPHA$-analysis, a fact already noted in the Mrk501 test analysis (chapter 10.1). The highest effective collection area is also obtained with Nepomuk's algorithm, again followed by Markus's cleaning.

The effect of the worse effective areas translates directly into a loss of energy threshold, obtained with the $DISP$-analysis. Although the upper limits compare well with the ones, obtained from the $ALPHA$-analysis, the lowest limit is now placed at 155–157 GeV instead of 150 GeV (see table 19). Also the upper limit has risen somewhat. The limit at the lowest mean energy is again obtained with Nepomuk's image cleaning. Taking into account the uncertainties due to the unknown incident spectrum and the possible degradation of the point spread function, the following result is obtained:

$$< \frac{d\Phi}{dE} > |_{156\,\mathrm{GeV}} \quad < \quad 8.3 \cdot 10^{-18}\ \mathrm{ph/cm^2/keV/s} \qquad \text{first } 90\,\mathrm{s} \tag{43}$$

$$< \frac{d\Phi}{dE} > |_{288\,\mathrm{GeV}} \quad < \quad 1.9 \cdot 10^{-18}\ \mathrm{ph/cm^2/keV/s} \qquad \text{first } 90\,\mathrm{s} \tag{44}$$

$$\tag{45}$$

While the first limit is 25% lower than the one obtained with the $ALPHA$-analysis, the second is equal, only the energies, they apply to, are higher.

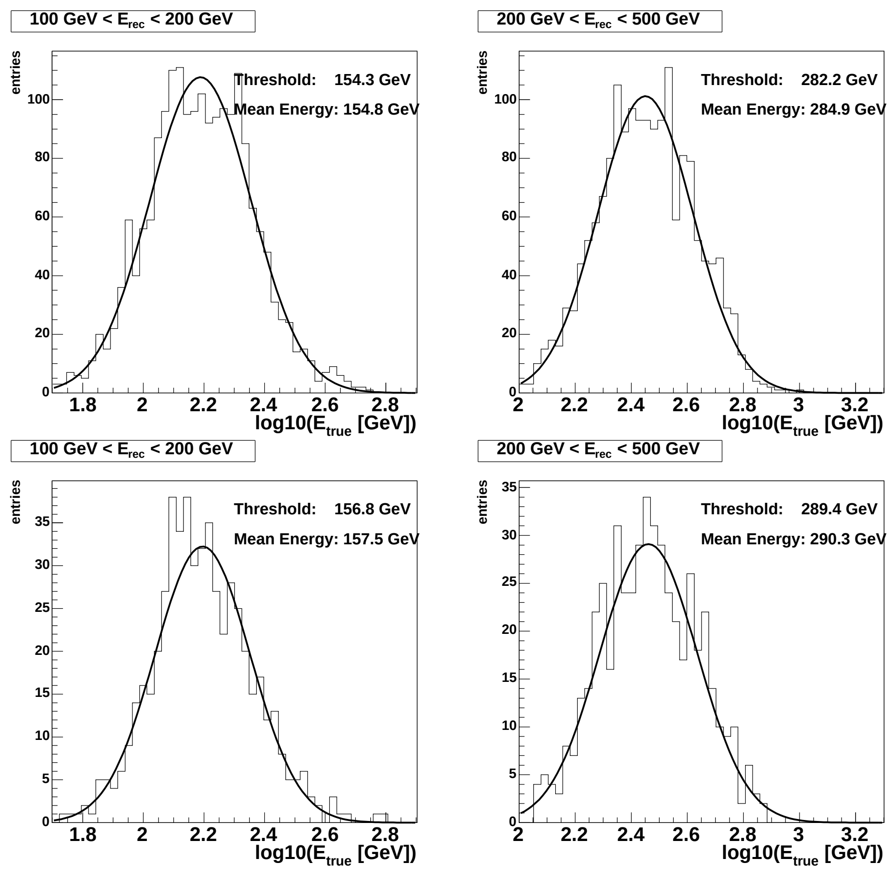

Figure 84: Distributions of the simulated MC energy for the prompt emission phase of GRB050713a, obtained with Nepomuk's image cleaning and all cuts applied. The four plots correspond to two slices of the $ENERGY$ parameters: Left: 100 to 200 GeV and right: >200 GeV reconstructed energy; Top: with cuts optimized using $PSF = 0.05^{\circ}\sigma$, bottom: using $PSF = 0.07^{\circ}\sigma$.

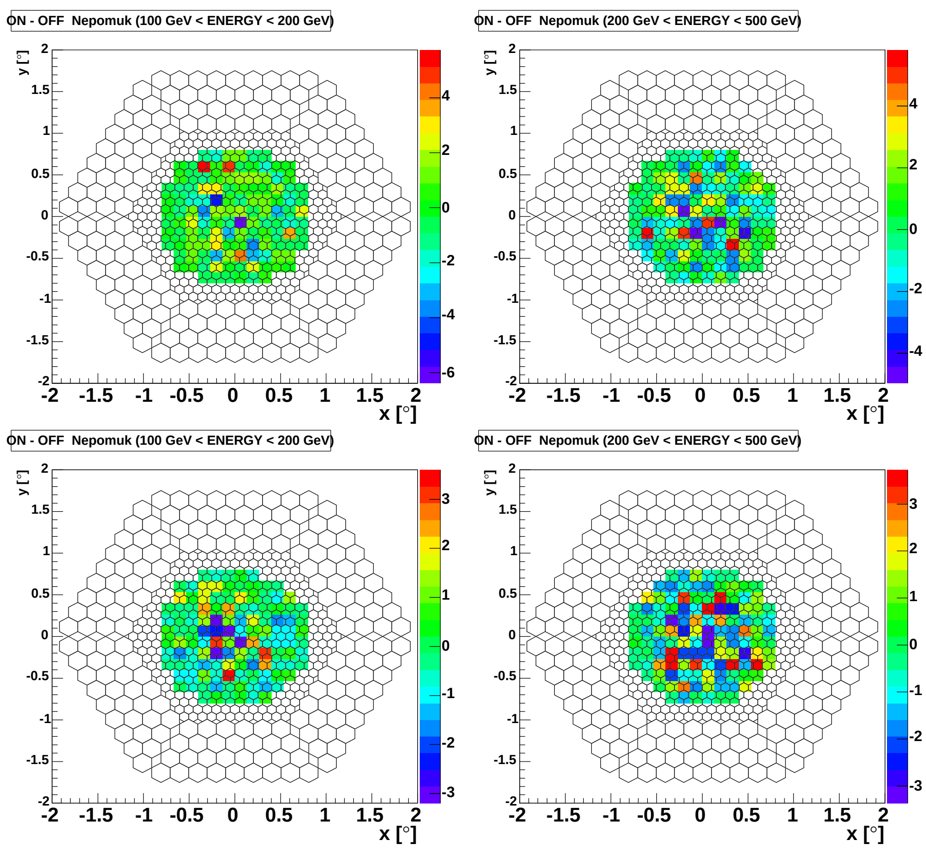

Figure 85: Distributions of the parameter $DISP$ for the 90 s of the prompt GRB emission, obtained with the Nepomuk's time image cleaning. The four plots correspond to two slices of the $ENERGY$ parameters: Left: 100 to 200 GeV and right: >200 GeV reconstructed energy; Top: with cuts optimized using $PSF = 0.05°\sigma$, bottom: using $PSF = 0.07°\sigma$. The red line indicates the region where a possible signal is expected.

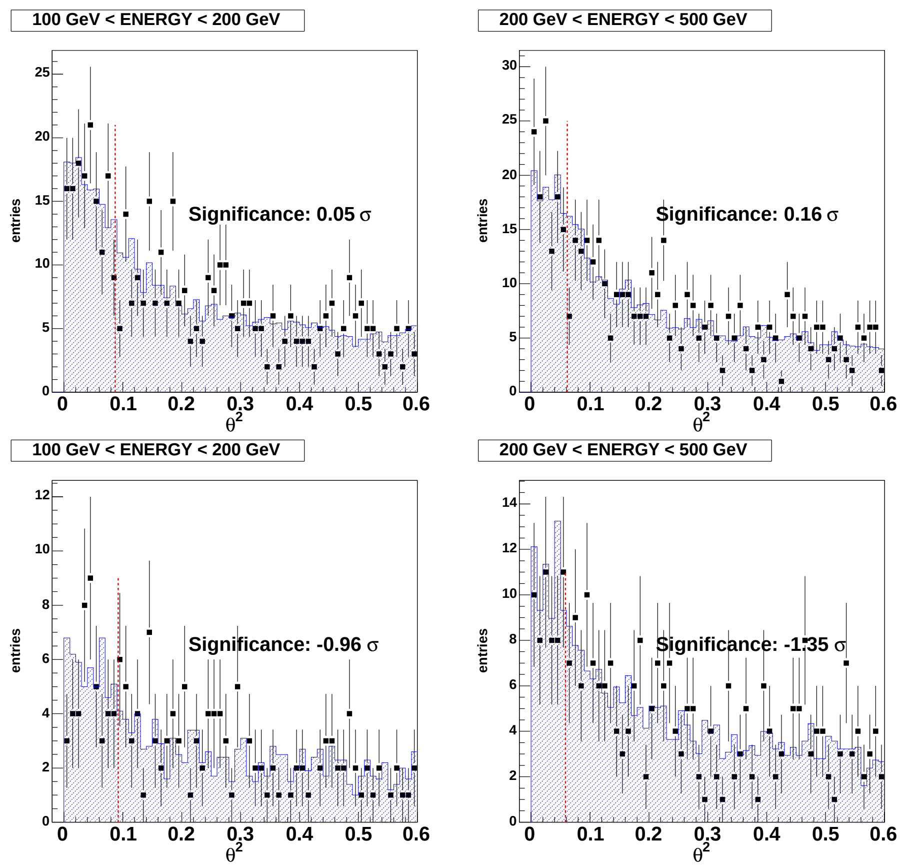

Figure 86: Distributions of the parameter θ^2 for the 90 s of the prompt GRB emission, obtained with the Nepomuk's time image cleaning. The four plots correspond to two slices of the $ENERGY$ parameters: Left: 100 to 200 GeV and right: >200 GeV reconstructed energy; Top: with cuts optimized using $PSF = 0.05°\sigma$, bottom: using $PSF = 0.07°\sigma$. The red line indicates the region where a possible signal is expected.

Image Cleaning Method	Reconst. Energy Range (GeV)	cut hadr.-ness	cut θ^2 (°)	Ex-cess Evts	Sign. Li Ma	U.L. Excess Evts (99% CL)	Mean E_γ MC (GeV)	Coll. Area at $< E_\gamma >$ (10^8 cm^2)	Mean Coll. Area (10^8 cm^2)
Abs. 7 4 (PSF= 0.05°σ)	100 - 200	0.60	0.09	-10	-1.2	21	179	1.2	1.0
	200 - 500	0.56	0.06	1	0.1	25	292.	6.0	5.0
Abs. 7 4 (PSF= 0.07°σ)	100 - 200	0.44	0.09	2	0.4	14	181	0.6	0.7
	200 - 500	0.38	0.06	-4	-0.6	18	299	5.5	4.9
Nepomuk (PSF= 0.05°σ)	100 - 200	0.56	0.09	1	0.0	31	155	2.4	1.9
	200 - 500	0.57	0.06	2	0.2	30	285	5.1	5.0
Nepomuk (PSF= 0.07°σ)	100 - 200	0.37	0.09	-7	-1.0	18	157	2.4	1.4
	200 - 500	0.40	0.06	-10	-1.3	18	290	5.6	4.2
Markus (PSF= 0.05°σ)	100 - 200	0.63	0.07	- 4	-0.4	23	166	1.5	1.3
	200 - 500	0.52	0.05	1	0.2	21	292	5.0	4.6
Markus (PSF= 0.07°σ)	100 - 200	0.40	0.09	-11	-2.0	13	173	1.5	1.2
	200 - 500	0.30	0.06	7	1.3	21	292	4.8	4.2

Table 18: Results of the *DISP*-analysis for the GRB050713a prompt emission data, using the later runs as OFF-data.

Image Cleaning Method	Differential Flux Upper Limits - PROMPT EMISSION						
	Mean Energy E_0 (GeV)	$\alpha = 1$	$\alpha = 2$	$\alpha = 2.25$	$\alpha = 2.5$	$\alpha = 3$	$E_b = 200$
		$d\Phi/dE$ 10^{-18} $\mathrm{cm^{-2}keV^{-1}s^{-1}}$	$d\Phi/dE$ 10^{-18} $\mathrm{cm^{-2}keV^{-1}s^{-1}}$	$d\Phi/dE$ 10^{-18} $\mathrm{cm^{-2}keV^{-1}s^{-1}}$	$d\Phi/dE$ 10^{-18} $\mathrm{cm^{-2}keV^{-1}s^{-1}}$	$d\Phi/dE$ 10^{-18} $\mathrm{cm^{-2}keV^{-1}s^{-1}}$	$d\Phi/dE$ 10^{-18} $\mathrm{cm^{-2}keV^{-1}s^{-1}}$
Abs. 7 4 (PSF= 0.05°σ)	179	8.6	10.	11.	11.	11.	10.
	292	1.1	1.4	1.4	1.4	1.4	1.5
Abs. 7 4 (PSF= 0.07°σ)	181	14.	16.	16.	16.	16.	15.
	299	1.0	1.2	1.2	1.2	1.2	1.2
Nepomuk (PSF= 0.05°σ)	155	6.7	8.0	8.2	8.3	8.2	7.0
	285	1.5	1.8	1.9	1.9	1.9	1.9
Nepomuk (PSF= 0.07°σ)	157	5.2	5.6	5.6	5.5	5.3	5.4
	290	1.1	1.3	1.3	1.3	1.2	1.3
Markus (PSF= 0.05°σ)	166	7.7	9.1	9.2	9.3	9.3	8.2
	292	1.2	1.5	1.5	1.5	1.5	1.6
Markus (PSF= 0.07°σ)	173	5.4	6.1	6.1	6.1	6.0	5.7
	292	1.4	1.6	1.7	1.7	1.6	1.7

Table 19: Differential upper limits obtained with the *DISP*-analysis for the GRB050713a prompt emission data, using the later runs as OFF-data. The variable α denotes the (unknown) incident gammas spectral index and E_b the break energy for the exponential cut-off spectrum.

10.3 Search in time slices of 100 seconds

As in the case of the *ALPHA*-analysis, a dedicated search for peak emission in steps of 101 seconds (22 time slices) was performed. Table 20 lists the used parameters for the peak emission search. Only Nepomuk's image cleaning was used, every of the 22 time slices was taken as ON data while the remaining data set was used as OFF data. A second search was performed shifting the phase of the time slice by 50 seconds.

Figures 87 to 88 show the distribution of obtained significances, with and without phase shift. Moreover, the number of excess events from below the corresponding cut in θ^2 are distributed in general randomly over time, as can be seen in figures 89 and 90.

Additionally to what could already be done in the *ALPHA*-analysis, the number of excess events anywhere in the camera was plotted to search for a possible gamma ray emission peak OFF-axis. The corresponding distribution of excess events can be seen in figures 91 and 92.

Image Cleaning Method	Reconst. Energy Range (GeV)	cut hadr.-ness	cut θ^2 (°)	Mean E_γ MC (GeV)
Nepomuk (PSF= 0.05°σ)	100 - 200	0.56	0.09	155
	200 - 500	0.58	0.06	285
Nepomuk (PSF= 0.07°σ)	100 - 200	0.34	0.09	157
	200 - 500	0.41	0.06	290

Table 20: Results of the *DISP*-analysis for the GRB050713a 100 seconds time slices search, using all ON data except that slice as OFF-data.

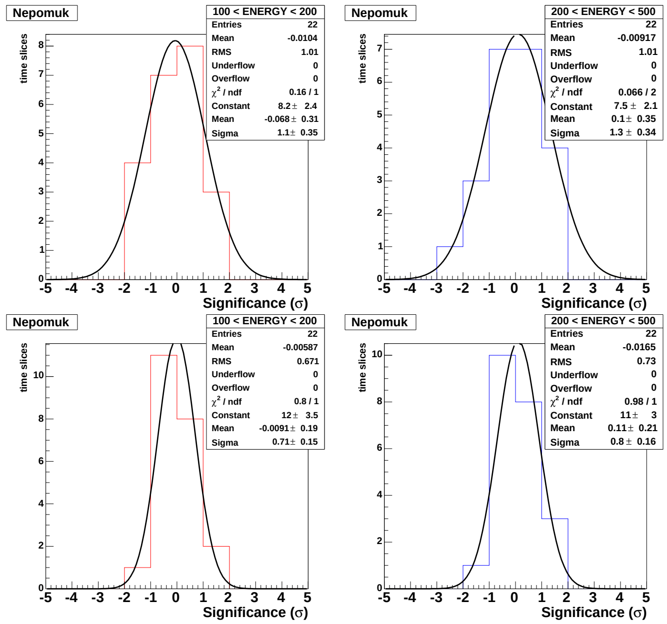

Figure 87: Distributions of the obtained significances during the peak search, obtained with the Nepomuk's time image cleaning. The four plots correspond to two slices of the $ENERGY$ parameters: Left: 100 to 200 GeV and right: 200 to 500 GeV reconstructed energy. Top: with cuts optimized using $PSF = 0.05°\sigma$, bottom: using $PSF = 0.07°\sigma$.

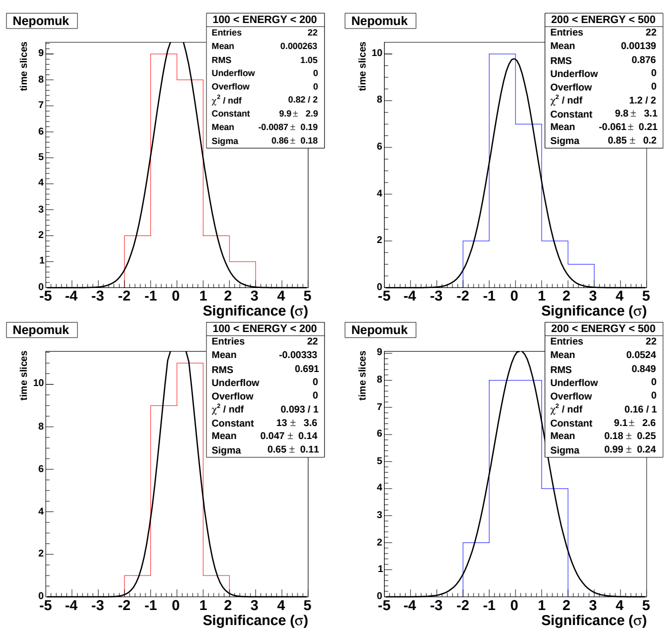

Figure 88: Distributions of the obtained significances during the peak search, times shifted by half a period. The data was cleaned with Nepomuk's time image cleaning. The four plots correspond to two slices of the $ENERGY$ parameters: Left: 100 to 200 GeV and right: 200 to 500 GeV reconstructed energy. Top: with cuts optimized using $PSF = 0.05°\sigma$, bottom: using $PSF = 0.07°\sigma$.

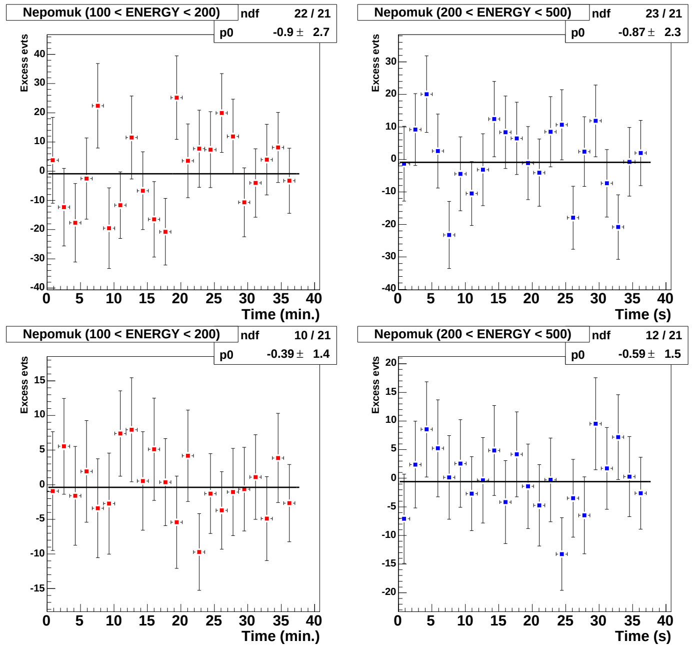

Figure 89: Number of excess events vs. time for the peak search, obtained with the Nepomuk's time image cleaning. The four plots correspond to two slices of the $ENERGY$ parameters: Left: 100 to 200 GeV and right: 200 to 500 GeV reconstructed energy. Top: with cuts optimized using $PSF = 0.05°\sigma$, bottom: using $PSF = 0.07°\sigma$..

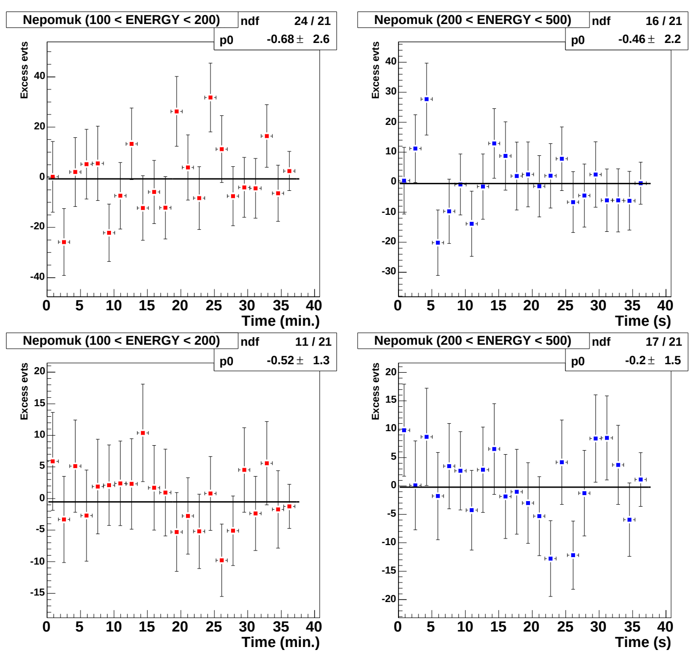

Figure 90: Number of excess events vs. time for the peak search, times shifted by half a period. The data was cleaned with Nepomuk's image cleaning. The four plots correspond to two slices of the $ENERGY$ parameters: Left: 100 to 200 GeV and right: 200 to 500 GeV reconstructed energy. Top: with cuts optimized using $PSF = 0.05°\sigma$, bottom: using $PSF = 0.07°\sigma$.

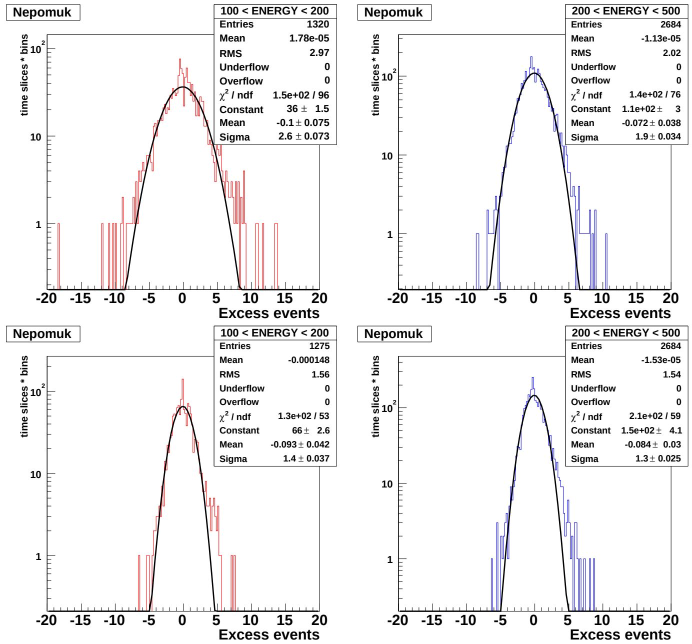

Figure 91: Number of excess events anywhere in the camera vs. time for the peak search, obtained with the Nepomuk's time image cleaning. The four plots correspond to two slices of the $ENERGY$ parameters: Left: 100 to 200 GeV and right: 200 to 500 GeV reconstructed energy. Top: with cuts optimized using $PSF = 0.05°\sigma$, bottom: using $PSF = 0.07°\sigma$..

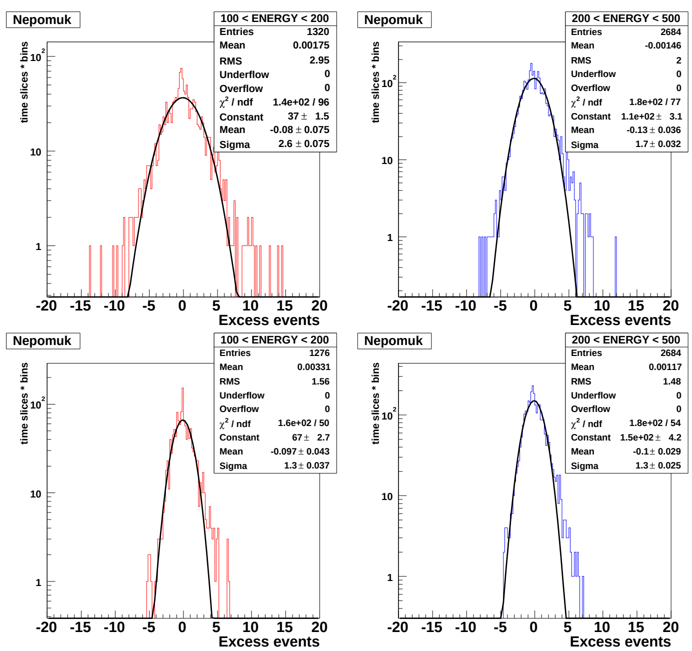

Figure 92: Number of excess events anywhere in the camera vs. time for the peak search, times shifted by half a period. The data was cleaned with Nepomuk's image cleaning. The four plots correspond to two slices of the $ENERGY$ parameters: Left: 100 to 200 GeV and right: 200 to 500 GeV reconstructed energy. Top: with cuts optimized using $PSF = 0.05°\sigma$, bottom: using $PSF = 0.07°\sigma$.

11 Conclusions

We have developed a complete analysis chain dedicated to low-energy events to be used for the analysis of Gamma-ray burst data.

We developed code to calibrate the GRB data using the interleaved calibration events from the previous source in order to calibrate the GRB with light pulses as close as possible to the start of the observation of the prompt emission.

Four image cleaning algorithms were tested against each other: The standard absolute image cleaning using thresholds of 10 and 5 photo-electrons, respectively, an absolute cleaning with lower thresholds (7 and 4 photo-electrons) and two algorithms exploiting the arrival time information extracted from the FADC data: A code written by Nepomuk Otte and another written by Markus Gaug. While testing the new code, a couple of bugs was found in already existing Mars versions which led to the new release Mars_V0-10-8.

All four image cleaning algorithm's were applied to the Mrk501 data, taken at the beginning of July, 2005 using standard cuts, except for a cut on $SIZE$ which takes our high-energy events. A new, unbiased way to optimize the cut on $HADRONNESS$ was developed and applied to the Mrk501 flare data leading to a $4\,\sigma$ detection of signals between 45 and 70 GeV for only one hour of ON data cleaned with one or the other algorithms based on arrival times. Nepomuk's cleaning algorithm yielded the lowest treshold in incident gamma energies: 65 GeV average energy in the lowest bin.

We applied the new analysis to the GRB050713a data using MC simulated gamma showers with two different point spread functions: $0.05°\sigma$ and $0.07°\sigma$. The data was analysed in four different ways: A dedicated search during the prompt emission phase, an analysis dedicated to the first 1000 s of GRB050713a data, one search of the whole 2220 seconds sample and a peak emission search scanning the 2220 seconds in steps of 100 seconds for significant excesses at low values of $ALPHA$. None of these searches yielded a significant signal and the following differential upper limits could be derived:

$$< \frac{d\Phi}{dE} > |_{150\,\mathrm{GeV}} \quad < \quad 1.3\cdot 10^{-17}\ \mathrm{ph/cm^2/keV/s} \ \equiv\ 3.6\,\mathrm{C.U.} \qquad \text{first } 90\,\mathrm{s} \tag{46}$$

$$< \frac{d\Phi}{dE} > |_{150\,\mathrm{GeV}} \quad < \quad 4.1\cdot 10^{-18}\ \mathrm{ph/cm^2/keV/s} \ \equiv\ 1.1\,\mathrm{C.U.} \qquad \text{first } 1000\,\mathrm{s} \tag{47}$$

$$< \frac{d\Phi}{dE} > |_{150\,\mathrm{GeV}} \quad < \quad 3.0\cdot 10^{-18}\ \mathrm{ph/cm^2/keV/s} \ \equiv\ 0.7\,\mathrm{C.U.} \qquad \text{entire } 2223\,\mathrm{s} \tag{48}$$

$$< \frac{d\Phi}{dE} > |_{150\,\mathrm{GeV}} \quad < \quad 1.8\cdot 10^{-17}\ \mathrm{ph/cm^2/keV/s} \ \equiv\ 4.9\,\mathrm{C.U.} \qquad \text{any } 100\,\mathrm{s} \text{ interval} \tag{49}$$

$$< \frac{d\Phi}{dE} > |_{280\,\mathrm{GeV}} \quad < \quad 2.3\cdot 10^{-18}\ \mathrm{ph/cm^2/keV/s} \ \equiv\ 3.2\,\mathrm{C.U.} \qquad \text{first } 90\,\mathrm{s} \tag{50}$$

$$< \frac{d\Phi}{dE} > |_{280\,\mathrm{GeV}} \quad < \quad 7.7\cdot 10^{-19}\ \mathrm{ph/cm^2/keV/s} \ \equiv\ 1.1\,\mathrm{C.U.} \qquad \text{first } 1000\,\mathrm{s} \tag{51}$$

$$< \frac{d\Phi}{dE} > |_{280\,\mathrm{GeV}} \quad < \quad 6.4\cdot 10^{-19}\ \mathrm{ph/cm^2/keV/s} \ \equiv\ 0.7\,\mathrm{C.U.} \qquad \text{entire } 2223\,\mathrm{s} \tag{52}$$

$$< \frac{d\Phi}{dE} > |_{280\,\mathrm{GeV}} \quad < \quad 4.8\cdot 10^{-18}\ \mathrm{ph/cm^2/keV/s} \ \equiv\ 6.6\,\mathrm{C.U.} \qquad \text{any } 100\,\mathrm{s} \text{ inverval} \tag{53}$$

The crab unit (C.U.) was thereby assumed to be: $1\,\mathrm{C.U.} := 1.5\cdot 10^{-3}\left(\frac{E}{\mathrm{GeV}}\right)^{-2.58}\mathrm{ph/cm^2/TeV/s}$, measured by MAGIC and fitted from 300 GeV to 5 TeV[2]. These limits include the following systematic

[2] Taking interpolated values from the direct measurements at these energies, the Crab unit diminishes by

uncertainties:

1. Possible degradations of the point spread function
2. Trigger inefficiencies in parts of the camera
3. Changes in the limits due to different possible spectral indices of the incident gamma ray spectrum
4. A global 10% uncertainty on the absolute calibration

Even including these systematic, the limit in the upper energy bin results to be slightly better than the one presented by N. Galante and A. Stamerra in [1]. The limit in the lower energy bin cannot be compared directly with their results since their analysis does not reach down so far in energy.

Also, integral limits were calculated to be compared with the ones presented in [1]. As the integral limits depend on the integration ranges, however, a close comparison cannot be made. We chose rather wide integration ranges and obtain compatibility with the sum of upper limits in the corresponding finer energy bins presented in [1].

A second, semi-independent $DISP$-analysis was performed using the similar, but not the same, parameters to calculate the $HADRONNESS$. Slightly different cuts were used there and a final cut on the parameter θ^2. Comparing these two analysis yield generally higher energy thresholds for the $DISP$-analysis, but comparable sensitivity and upper limits at higher energies. We noted that the so-called "ghost-busting" efficiency goes down to 0.5 at very low energies and may be responsible for the higher threshold in energy.

about 10% at 150 GeV and by less than 5% at 280 GeV

References

[1] N. Galante and A. Stamerra, Observation of GRB050713a with MAGIC, MAGIC internal note, 25$^{\text{th}}$ July, 2005 (see also: Draft for a publication in ApJ).

[2] A. Falcone, GRB050713a: Swift detection of Bright Burst, GCN circular 3581, July 13, 2005.

[3] A. De Luca, GRB050713a: analysis of the XMM-Newton observation, GCN circular 3695, July 28, 2005.

[4] A. Falcone, D. Morris for the SWIFT collaboration, private e-mail exchange (SWIFT digital data allocation) with M. Teshima, July 14, 2005.

[5] P. Liebing, MAGIC internal report TDAS-0508, `http://wwwmagic.mppmu.mpg.de/documents/TDAS_notes/tdas0508/tdas0508.html`

[6] E. De Oña Wilhelmi, private communication

[7] Th. Schweizer, PhD Thesis, Universitat Autònoma de Barcelona, 2002, available on `http://wwwmagic.mppmu.mpg.de/publications/theses/ThomasS_thesis.ps.gz`

[8] Th. Schweizer, email to `magic_soft@mppmu.mpg.de` from March 2, 2005.

[9] P. Majumdar, private communication

[10] O. Helene, Upper LImit of Peak Area, Nuclear Instruments and Methods 212, 1983.

[11] Bock, R. K., Chilingarian, A., Gaug, M., Hakl, F. Hengstebeck, T., Jirina, M., Klaschka, J., Kotrc, E., Savicky, P., Towers, S., Vaciulis, A., Wittek W., “Methods for multidimensional event classification: a case study using images from a Cherenkov gamma-ray telescope”, NIM A516, pp. 511-528, 2004